

DISSERTATION

MOBILITY AND FLUORESCENCE OF BARIUM IONS IN XENON GAS FOR THE  
EXO EXPERIMENT

Submitted by  
Julio Cesar Benitez Medina  
Department of Physics

In partial fulfillment of the requirements  
For the Degree of Doctor of Philosophy  
Colorado State University  
Fort Collins, Colorado  
Spring 2014

Doctoral Committee

Advisor: William Fairbank

Bruce Berger  
Stephen Lundeen  
Carmen Menoni

Copyright by Julio Cesar Benitez Medina 2014

All Rights Reserved

## ABSTRACT

### MOBILITY AND FLUORESCENCE OF BARIUM IONS IN XENON GAS FOR THE EXO EXPERIMENT

The Enriched Xenon Observatory (EXO) is an experiment which aims to observe the neutrinoless double beta decay of  $^{136}\text{Xe}$ . The measurement of this decay would give information about the absolute neutrino mass and whether or not the neutrino is its own antiparticle. Since this is a very rare decay, the ability to reject background events by detecting the barium ion daughter from the double beta decay would be a major advantage. EXO is currently operating a detector with 200 kg of enriched liquid xenon, and there are plans to build a ton scale xenon detector.

Measurements of the purity of liquid xenon in our liquid xenon test cell are reported. These results are relevant to the research on detection of single barium ions by our research group at Colorado State University. Details of the operation of the purity monitor are described. The effects of using a purifier, recirculation and laser ablation on the purity of liquid xenon are discussed.

Mobility measurements of barium in xenon gas are reported for the first time. The variation of mobility with xenon gas pressure suggests that a significant fraction of molecular ions are formed when barium ions interact with xenon gas at high pressures. The measured mobility of  $\text{Ba}^+$  in Xe gas at different pressures is compared with the predicted theoretical value, and deviations are explained by a model that describes the fraction of molecular ions in Xe gas as a function of pressure. The results are useful for the analysis of experiments of fluorescence of  $\text{Ba}^+$  in xenon gas. It is also important to know the mobility of the ions in order to calculate the time they interact with an excitation laser in fluorescence experiments and in proposed  $^{136}\text{Ba}^+$  daughter detection schemes.

This thesis presents results of detection of laser induced fluorescence of  $\text{Ba}^+$  ions in Xe gas. Measurements of the pressure broadening of the excitation spectra of  $\text{Ba}^+$  in xenon gas are presented. Nonradiative decays due to gas collisions and optical pumping affect the number of fluorescence counts detected. A model that treats the barium ion as a three level system is used to predict the total number of fluorescence counts and correct for optical pumping. A pressure broadening coefficient for  $\text{Ba}^+$  in xenon gas is extracted and limits for p-d and d-s nonradiative decay rates are extracted. Although fluorescence is reduced significantly at 5-10 atm xenon pressure, the measurements in this thesis indicate that it is still feasible to detect  $^{136}\text{Ba}^+$  ions directly in high pressure xenon gas, e.g. in a double beta decay detector.

## ACKNOWLEDGMENTS

I would like to thank my family for always believing in me, and for their unconditional support. I could have not made it here without them. Special thanks to Ms. Nada Sekeljic for her helping me staying optimistic while I was writing my thesis.

I want to thank my advisor, William Fairbank, for giving me to opportunity to work under his guidance. He taught me the importance of being curious and learn something new from every experiment. I also want to thank all the members of the EXO collaborators with whom I spent a fair amount of time working in the EXO-200 experiment in Carlsbad NM. It was one of the best experiences of my career working with so many talented scientists and learning from them.

I would like to thank my thesis committee members, Bruce Berger, Stephen Lundeen, and Carmen Menoni, for taking the time to review my thesis and for their feedback. I also wish to thank Dr. Siu Au Lee for her advice and loaning of equipment essential for my experiments. Bob Adame deserves special thanks for his invaluable help in the machine shop.

In addition I wish to thank my labmates, Brian Mong, Shon Cook, Tim Walton, Chris Chambers, and Adam Craycraft for providing me help with my experiments. I would particularly like to thank Kendy Hall, with whom I worked together for several years, for teaching me everything he knew about the lab.

The work presented in this thesis was supported by the Department of Energy, grant number DE-FG02-03ER41255.

# TABLE OF CONTENTS

Abstract . . . . .	ii
Acknowledgments . . . . .	iv
1 Introduction . . . . .	1
1.1 Neutrino Physics . . . . .	1
1.2 Neutrino Oscillations . . . . .	2
1.3 Neutrinoless Double Beta Decay . . . . .	5
1.4 EXO Experiment . . . . .	9
1.4.1 EXO 200 . . . . .	9
1.4.2 Barium Tagging in EXO . . . . .	11
2 Theory . . . . .	15
2.1 Energy Levels of $Ba^+$ in Vacuum . . . . .	15
2.2 Atomic Radiation . . . . .	16
2.3 Three Level Model . . . . .	18
2.4 Broadening of Spectral Lines . . . . .	20
2.4.1 Natural Line Broadening . . . . .	20
2.4.2 Pressure Broadening . . . . .	21
2.4.3 Doppler Broadening . . . . .	22
2.5 Theory of Liquid Xenon Purity Monitor . . . . .	23
2.5.1 ICARUS Purity Monitor . . . . .	24
2.6 Ion Mobility . . . . .	25
2.7 Molecular Ion Formation . . . . .	27
2.7.1 Termolecular Association . . . . .	27
2.7.2 Collisional Dissociation . . . . .	28
2.7.3 Fraction of Atomic Ions . . . . .	29

3	Apparatus . . . . .	31
3.1	Xenon System . . . . .	31
3.1.1	Xenon Cell . . . . .	33
3.1.2	Cryogenic System . . . . .	34
3.1.3	Gas Handling and Recirculation System . . . . .	37
3.2	CSU Purity Monitor . . . . .	41
3.2.1	Electron charge detection . . . . .	44
3.2.2	Detection of Ba <sup>+</sup> ion current . . . . .	46
3.2.3	Determination of electron lifetime . . . . .	49
3.2.4	Electron transmission . . . . .	52
3.2.5	Transparency of grids . . . . .	63
3.3	Ba <sup>+</sup> Ion Creation by Laser Ablation . . . . .	64
3.4	Mobility of Ions in Gas . . . . .	68
3.4.1	Calculation of $d_{eff}^2$ . . . . .	70
3.4.2	Gas handling for mobility experiments . . . . .	74
3.5	Fluorescence Detection . . . . .	75
3.5.1	Light Collection Setup . . . . .	76
3.5.2	Single mode operation of excitation laser . . . . .	78
3.5.3	Light Detection Efficiency . . . . .	79
4	Results . . . . .	86
4.1	Purity Measurements . . . . .	86
4.1.1	Electron Lifetime Measurements . . . . .	86
4.1.2	Effects of Recirculation on the Electron Lifetime . . . . .	88
4.1.3	Effects of Ablation on the Electron Lifetime . . . . .	91
4.2	Mobility Experiments . . . . .	94
4.2.1	Charge Dependence of Ionic Mobility . . . . .	95
4.2.2	Mobility Results . . . . .	102

4.2.3	Molecular Ion Formation . . . . .	104
4.3	Fluorescence Experiments . . . . .	109
4.3.1	Fluorescence Spectra . . . . .	110
4.3.2	Pressure Broadening . . . . .	113
4.3.3	Predicted Fluorescence Counts and Nonradiative Decays . . . . .	127
4.3.4	Single Ion Detection at High Pressure Xenon Gas . . . . .	138
5	Conclusion . . . . .	143
	References . . . . .	146

# 1 Introduction

## 1.1 Neutrino Physics

The existence of neutrinos was initially proposed by Pauli in 1930, and he originally called them neutrons. He introduced the new particle to explain the apparent non conservation of energy and angular momentum in a  $\beta$  decay. At that time it was thought that the  $\beta$  decay emitted an electron only from a nucleus  $(A, Z)$  in a nuclear transition of the form  $(A, Z) \rightarrow (A, Z + 1) + e^-$ . From the conservation of energy, this type of decay would require that the emitted electron in the  $\beta$  decay had a fixed energy approximately equal to the released energy  $Q$ . Experimental results, however, showed that the energy spectrum of the  $\beta$  decay was continuous with an end point at an energy equal to  $Q$ . Pauli suggested the  $\beta$  decay was a three body process given by

$$(A, Z) \rightarrow (A, Z + 1) + e^- + \bar{\nu}_e \quad (1.1)$$

where the released energy is shared by the electron and the neutrino  $\bar{\nu}_e$ . This explains the continuous energy spectra of the  $\beta$  decay. Pauli also proposed that the neutrino is a neutral particle with a spin of  $\frac{1}{2}$  to preserve the conservation of charge and angular momentum [1]. From the energy distribution of the emitted electron from the  $\beta$  decay it was deduced that the mass of the neutrino was much smaller than the electron mass. The Standard Model of particle physics assumes that neutrinos are massless.

Neutrinos were not directly observed experimentally until 1956 when Reines and Cowen detected the process

$$\bar{\nu} + p \rightarrow e^+ + n \quad (1.2)$$

in which a neutron and a positron are produced by the interaction of an antineutrino and a proton. This is called inverse  $\beta$  decay. Frederick Reines was awarded the Nobel Prize in 1995 for the detection of the neutrino.

## 1.2 Neutrino Oscillations

The idea that neutrinos are massive and oscillate was suggested by Pontecorvo in 1958 [2]. It is now known that there are three different flavor neutrinos: electron neutrinos  $\nu_e$ , muon neutrinos  $\nu_\mu$ , and tau neutrinos  $\nu_\tau$ . Each flavor has its corresponding antiparticle, an antineutrino. Neutrinos can oscillate between the three different flavors. The first evidences of neutrino oscillation was in the measurements of solar neutrinos by R. Davis [3]. Solar neutrinos were detected by observing the reaction



It was observed that the flux of solar neutrinos  $\nu_e$  was 2 to 3 times smaller than the predicted flux.

In the current model of neutrino oscillations, neutrino flavor eigenstates and mass eigenstates are not the same. The flavor eigenstates are related to the mass eigenstates by a linear superposition

$$|\nu_\alpha\rangle = \sum_i U_{\alpha i} |\nu_i\rangle \quad (1.4)$$

where  $|\nu_\alpha\rangle$  are the flavor eigenstates and  $|\nu_i\rangle$  the mass eigenstates.  $U$  is the unitary PMNS mixing matrix named for Pontecorvo, Maki, Nakagawa and Sakata [4]. It has the form

$$U = \begin{pmatrix} 1 & 0 & 0 \\ 0 & c_{23} & s_{23} \\ 0 & -s_{23} & c_{23} \end{pmatrix} \begin{pmatrix} c_{13} & 0 & s_{13}e^{-i\delta} \\ 0 & 1 & 0 \\ -s_{13}e^{i\delta} & 0 & c_{13} \end{pmatrix} \begin{pmatrix} c_{12} & s_{12} & 0 \\ -s_{12} & c_{12} & 0 \\ 0 & 0 & 1 \end{pmatrix} \quad (1.5)$$

where  $c_{ij} = \cos \theta_{ij}$  and  $s_{ij} = \sin \theta_{ij}$ , and  $\theta_{ij}$  is the mixing angle between the mass states  $i$  and  $j$ . The phase  $\delta$  is related to the violation of Charge-Parity (CP) symmetry.

The time dependence of a neutrino state, created by weak interactions in a flavor eigenstate, is obtained by applying the space-time translation operator  $e^{-i(Ht - \vec{P} \cdot \vec{r})}$ , and it is given by [5]:

$$|\nu_\alpha(x, t)\rangle = \sum_i U_{\alpha i} e^{-i(E_i t - p_i x)} |\nu_i\rangle \quad (1.6)$$

The time dependent probability for a neutrino to convert from flavor  $\alpha$  to flavor  $\beta$  is then given by

$$P(\alpha \rightarrow \beta)(t) = |\langle \nu_\beta | \nu_\alpha(x, t) \rangle|^2 = \left| \sum_i U_{\beta i}^* U_{\alpha i} e^{-i(E_i t - p_i x)} \right|^2 \quad (1.7)$$

For relativistic neutrinos that have a momentum  $p$  when they are emitted at the source,  $E \approx p$ , and  $p \gg m_i$  in a unit system where  $c = 1$ . The energy  $E_i$  is approximately equal to

$$E_i = \sqrt{m_i^2 + p_i^2} \simeq p_i + \frac{m_i^2}{2p_i} \simeq E + \frac{m_i^2}{2E} \quad (1.8)$$

The time it takes the neutrino to travel a distance  $L$  from the source to the detector is approximately equal to  $L$ , using  $c = 1$ . The probability of detecting a flavor neutrino  $\beta$  is then given by

$$P(\alpha \rightarrow \beta)(t) = \left| \sum_i U_{\beta i}^* U_{\alpha i} e^{-i \frac{m_i^2}{2} \frac{L}{E}} \right|^2 \quad (1.9)$$

A simple case to analyze is the oscillation primarily between two neutrino flavors. In this case only one mixing angle  $\theta$  is needed to describe the relation between two neutrino states. The unitary mixing matrix is given by

$$U = \begin{pmatrix} \cos \theta & \sin \theta \\ -\sin \theta & \cos \theta \end{pmatrix} \quad (1.10)$$

The probability of converting a flavor neutrino  $\nu_\alpha$  to a  $\nu_\beta$  flavor is then [4]:

$$P(\nu_{\alpha} \rightarrow \nu_{\beta}) = \sin^2(2\theta) \sin^2\left(\frac{\Delta m^2 L}{4E}\right) \quad (1.11)$$

The implications of this equation are that if neutrino oscillations are observed, the mixing angle  $\theta$  and the mass squared difference  $\Delta m^2$  must be different from zero.

Several experiments have measured the mixing angles and the mass squared differences  $\Delta m_{ij}^2$  by detecting neutrino oscillations. The Super Kamiokande collaboration gave the first clear evidence of neutrino oscillation by observing atmospheric neutrinos. The results of the Super Kamiokande experiments have been fully confirmed by accelerator neutrino experiments K2K, MINOS, and T2K. Studies of atmospheric neutrinos give information about  $\Delta m_{32}^2$  and  $\theta_{23}$ . Results from oscillation in solar neutrinos have been reported by the SNO and KamLAND experiments. Oscillations in solar neutrinos give information about  $\Delta m_{21}^2$  and  $\theta_{12}$ . The mixing angle  $\theta_{13}$  was measured recently by the Double Chooz, T2K, and the Daya Bay experiments.

A summary of the best fit mass squared differences and mixing angles from multiple experiments are listed in Table 1.1 [6]. The result for the mixing angle  $\theta_{13}$  is from the recent measurement of the Daya Bay experiment, reported on October 2013, and is the best measurement of  $\theta_{13}$  to date [7].

Since the sign of  $\Delta m_{32}^2$  is not known, there are two possibilities of mass hierarchies. This is depicted in Figure 1.1. One possibility is called normal hierarchy, where the smallest mass is  $m_1$ , and the other is called inverted hierarchy where the smallest mass is  $m_3$ .

Neutrino oscillation experiments provide mass square differences, but they do not provide information about the absolute mass of neutrinos. These experiments show clear evidence of neutrino oscillation, thus proving that neutrinos have mass, contradicting the assumption of the Standard Model that neutrinos are massless.

**Table 1.1:** Summary of neutrino mass squared differences and mixing angles.

Measurement	Value
$\Delta m_{21}^2$	$7.59 \pm_{0.18}^{0.20} \times 10^{-5} \text{ eV}^2$
$ \Delta m_{32}^2 $	$2.43 \pm 13 \times 10^{-3} \text{ eV}^2$
$\sin^2 \theta_{12}$	$0.312 \pm_{0.015}^{0.017}$
$\sin^2 \theta_{23}$	$0.51 \pm 0.06$
$\sin^2 \theta_{13}$	$0.090 \pm_{0.009}^{0.008}$

### 1.3 Neutrinoless Double Beta Decay

Several fundamental questions about neutrinos could be answered by the detection of neutrinoless double beta decay ( $0\nu\beta\beta$ ), such as whether neutrino is its own antiparticle, and the absolute neutrino mass. These are discussed briefly in this section.

In one type of double beta decay, two neutrino double beta decay ( $2\nu\beta\beta$ ), two neutrons in a nucleus decay into two protons, and two electrons and two electron antineutrinos are emitted in the process:

$$(A, Z) \rightarrow (A, Z + 2) + 2e^- + 2\bar{\nu}_e \quad (1.12)$$

The Feynman diagram for this decay is given in Figure 1.2 on the left. This process conserves lepton number and is allowed by the Standard Model. In a second type of double beta decay, neutrinoless double beta decay ( $0\nu\beta\beta$ ), no antineutrinos are emitted:

$$(A, Z) \rightarrow (A, Z + 2) + 2e^- \quad (1.13)$$

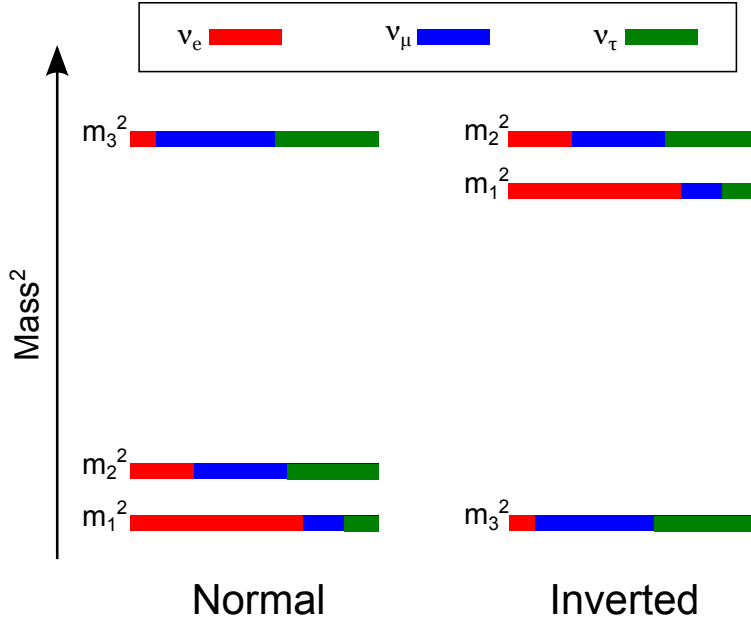


**Figure 1.1:** Diagram of normal and inverted mass hierarchy.

The  $(0\nu\beta\beta)$  process shown in Figure 1.2 on the right only occurs if the neutrino is a Majorana particle, meaning that the neutrino is its own antiparticle. In a  $(0\nu\beta\beta)$  decay, an antineutrino from a beta decay changes helicity and is absorbed at the other beta decay vertex. This a second order process in the weak interaction, and it is very rare [1]. This process is forbidden in the Standard Model because the lepton number is not conserved if only two electrons and no antineutrinos are emitted in the decay [8].

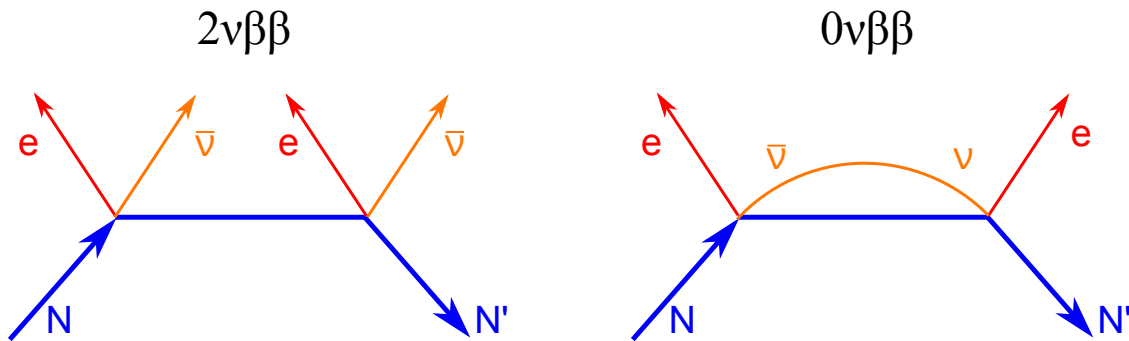


**Figure 1.2:** Feynman diagrams for two neutrino double beta decay  $2\nu\beta\beta$  and for neutrinoless double beta decay  $0\nu\beta\beta$ . N is the initial nucleus and N' is the daughter nucleus of the decay

The energy spectra of the two decays is shown in Figure 1.3. In  $2\nu\beta\beta$  decay the two electrons and the two antineutrinos share the energy  $Q$  of the decay, and the result is a continuous energy spectrum with values of energy less than  $Q$ . In the case of  $0\nu\beta\beta$  decay, essentially all of the kinetic energy is carried by the two electrons, and its energy spectrum is a sharp peak at energy  $Q$  with very little spread.

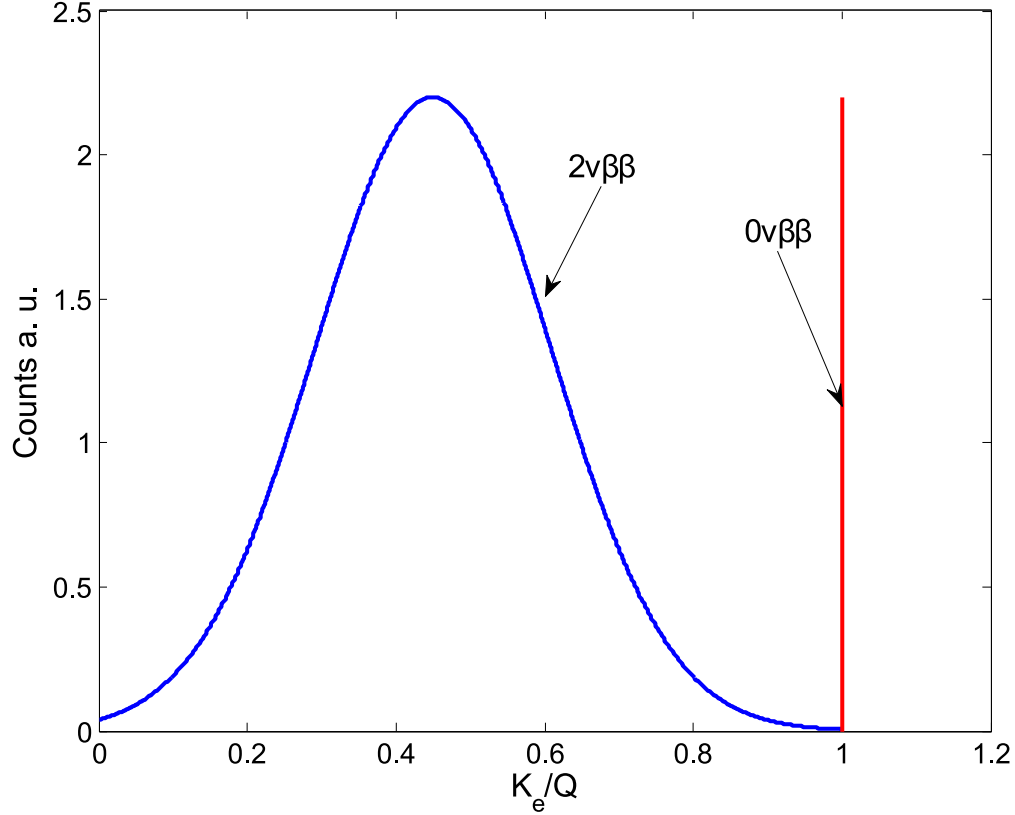


**Figure 1.3:** An illustration of the energy spectrum of  $2\nu\beta\beta$  and  $0\nu\beta\beta$  decays. The total energy of the electrons is normalized to the endpoint energy  $Q$ .

The half life  $T_{1/2}^{0\nu}$  for  $0\nu\beta\beta$  decay is related to the effective Majorana neutrino mass as [9]

$$T_{1/2}^{0\nu} = \left[ G^{0\nu}(E_0, Z) |M_{GT}^{0\nu} - \frac{g_V^2}{g_A^2} M_F^{0\nu}|^2 \langle m_\nu \rangle^2 \right]^{-1} \quad (1.14)$$

In this equation  $G^{0\nu}$  is a phase-space factor that depends on the end point energy of the decay  $Q$  and the nuclear charge  $Z$ ,  $M_{GT}^{0\nu}$  and  $M_F^{0\nu}$  are Gamow-Teller and Fermi nuclear matrix elements, which can be calculated from theoretical nuclear models, and  $g_V$  and  $g_A$

are the vector and axial-vector coupling constants. The effective neutrino mass  $\langle m_\nu \rangle$  is given by

$$\langle m_\nu \rangle = \left| \sum_j U_{ej}^2 m_j \right| \quad (1.15)$$

where  $U_{ej}$  is the PMNS mixing matrix defined earlier.

A list of several isotopes that are used in different double beta decay experiments, with their corresponding Q values and natural abundance, are listed in Table 1.2.

**Table 1.2:** Double beta decay source isotopes. Table adapted from [6]

$\beta\beta$ -decay	Q (KeV)	nat. abund. (%)	experiments
$^{48}\text{Ca} \rightarrow ^{48}\text{Ti}$	4273.7	0.187	CANDLES
$^{76}\text{Ge} \rightarrow ^{76}\text{Se}$	2039.1	7.8	GERDA, Majorana
$^{82}\text{Se} \rightarrow ^{82}\text{Kr}$	2995.5	9.2	SuperNEMO, Lucifer
$^{100}\text{Mo} \rightarrow ^{100}\text{Ru}$	3035.0	9.6	MOON, AMore
$^{116}\text{Cd} \rightarrow ^{116}\text{Sn}$	2809	7.6	Cobra
$^{130}\text{Te} \rightarrow ^{130}\text{Xe}$	2530.3	34.5	CUORE
$^{136}\text{Xe} \rightarrow ^{136}\text{Ba}$	2461.9	8.9	EXO, KamLAND-Zen, NEXT XMASS
$^{150}\text{Nd} \rightarrow ^{150}\text{Sm}$	3367.3	5.6	SNO+, DCBA/MTD

The current best experimental limits of the half life of neutrinoless double beta decay have been measured by the Heidelberg-Moscow experiment, GERDA, KamLAND-Zen, and EXO-200. The Heidelberg-Moscow experiment and the GERDA experiment search for  $0\nu\beta\beta$  decay of the isotope  $^{76}\text{Ge}$ ; they reported a lower limit for the  $0\nu\beta\beta$  half life of  $T_{12}^{0\nu}(^{76}\text{Ge}) > 1.9 \times 10^{25}$  years [10] and  $T_{12}^{0\nu}(^{76}\text{Ge}) > 2.1 \times 10^{25}$  years [11] respectively. The KamLAND-Zen and EXO-200 experiments look for the  $0\nu\beta\beta$  decay of the isotope  $^{136}\text{Xe}$ . The reported lower limits of the  $0\nu\beta\beta$  half life are:  $T_{12}^{0\nu}(^{136}\text{Xe}) > 1.9 \times 10^{25}$  years for the KamLAND-Zen experiment, which corresponds to a Majorana neutrino mass limit of  $\langle m_{nu} \rangle < (120-250)$

meV [12]; and  $T_{12}^{0\nu}(^{136}\text{Xe}) > 1.6 \times 10^{25}$  years for the EXO-200 experiment, which corresponds to masses less than 140-380 meV, depending on the matrix element calculation [13].

## 1.4 EXO Experiment

Our group is part of the Enriched Xenon Observatory (EXO) collaboration that is aiming to detect a  $0\nu\beta\beta$  and  $2\nu\beta\beta$  decay from the isotope  $^{136}\text{Xe}$ . The  $0\nu\beta\beta$  process that EXO hopes to observe is



Since Xe gas and liquid Xe are transparent, the daughter of the decay may be tagged using laser induced fluorescence [14]. The detection of the barium daughter ion would eliminate background events from natural radioactivity, since relevant background events are not expected to produce a barium ion. One of the research topics presented in this thesis is the detection of barium ions in xenon gas, which is a subject of interest for gas xenon double beta decay detectors.

### 1.4.1 EXO 200

The first generation EXO experiment is the EXO 200 experiment, so named because it contains on the order of 200 kg of enriched  $^{136}\text{Xe}$ . The experiment is located in Carlsbad, New Mexico at the Waste Isolation Pilot Plant (WIPP) in a salt mine 655 meters underground.

The EXO 200 experiment utilizes a time projection chamber (TPC) detector, with enriched liquid xenon as both the source and the detection medium. The detector is filled with 175 kg of enriched xenon, of which 80.6% is the isotope  $^{136}\text{Xe}$  and 19.4% is  $^{134}\text{Xe}$  [15]. The liquid xenon is at a temperature of 167 K and at a pressure of 1110 Torr. A picture of half the TPC is shown in figure 1.4. The TPC has a cylindrical shape and has a cathode grid at center plane of the cylinder.



**Figure 1.4:** Picture of half of the EXO 200 TPC before installation. The top part is the cathode grid, and the anode wires are in the bottom part. The APD's, which are installed in the holes at the bottom, are not shown in this picture.

Each end of the TPC has avalanche photodiodes (APD) that collect scintillation light produced when fast electrons ionize xenon atoms. There are two wire grids crossed at  $60^\circ$  at each end of the TPC that collect the charge signal from the electrons of the ionization process. The location of the event can be reconstructed by combining the charge signal with the scintillation signal. The charge signal detected by the wire grids gives the 2D location, and the 3D position is obtained by taking the difference in time between the ionization and the scintillation signal, which is the electron drift time. The charge and scintillation signals are also used to calculate the event energy.

A schematic diagram of the EXO-200 detector is shown in Figure 1.5. The TPC is contained in a copper vessel that, is filled with liquid xenon. In order to reduce the natural radiation from copper, the walls of the vessel are only 1.37 mm thick. The vessel is mounted

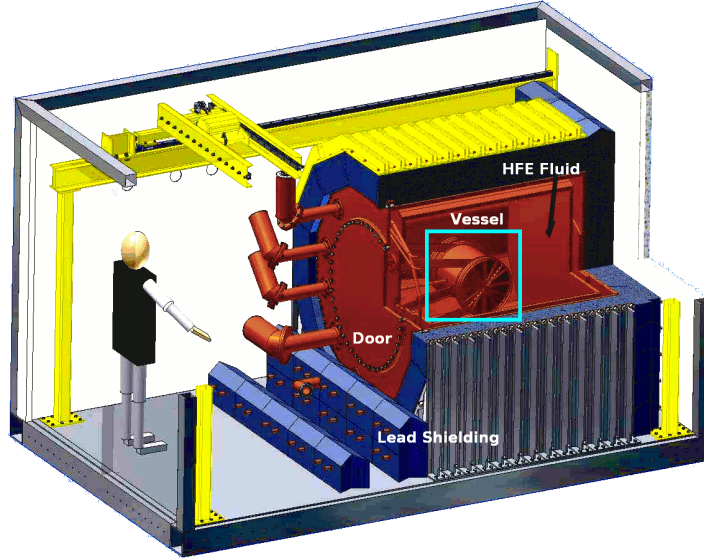


**Figure 1.5:** Schematic diagram of the EXO-200 detector.

inside a double walled cryostat filled with HFE-7000 ( $\text{CF}_3\text{CF}_2\text{CF}_2\text{OCH}_3$ ) cryogenic fluid that serves as a heat transfer medium.

It is important to reduce the backgrounds near the  $Q$  energy since the  $0\nu\beta\beta$  decay rate is very small. Low background levels in the EXO 200 detection were achieved by selecting only ultra-low radioactivity materials for the construction of the TPC, copper vessel, cryostat, and plumbing. The cryostat is shielded from external radiation with a 25 cm thick layer of lead [16].

EXO-200 has been taking data since May 2011; it reported the first observation of  $2\nu\beta\beta$  decay in  $^{136}\text{Xe}$ , and measured a half life of  $T_{1/2}^{2\nu\beta\beta} = 2.11 \pm 0.04(\text{stat}) \pm 0.21(\text{syst}) \times 10^{21}$  years [15]. The systematic uncertainty comes from energy calibration, fiducial volume and background models. The KamLAND-Zen collaboration subsequently reported a value of  $T_{1/2}^{2\nu\beta\beta} = 2.38 \pm 0.02(\text{stat}) \pm 0.14(\text{syst}) \times 10^{21}$  years [17] that agrees with the EXO-200 result.

### 1.4.2 Barium Tagging in EXO

The EXO collaboration is currently working on the design a the new generation  $0\nu\beta\beta$  experiment. The successor of EXO-200 is, for the time being called nEXO (next EXO). This new experiment will be a ton scale detector of liquid xenon that builds on many of the

things learned in EXO 200. It may also incorporate detection of the barium daughter ion of the  $0\nu\beta\beta$  decay as an additional means of "tagging" real  $^{136}\text{Xe}$  decay events to eliminate all other backgrounds.

The neutrino mass sensitivity depends on the  $0\nu\beta\beta$  half life time according to equation (1.14) as  $\langle m_\nu \rangle \propto 1/\sqrt{T_{1/2}^{0\nu\beta\beta}}$ . In a background free experiment, the mass sensitivity scales as  $1/\sqrt{Nt}$ , where  $N$  is the number of nuclei and  $t$  is the time that the experiment is run. For an experiment with non zero background proportional to  $N$ , fluctuations in the background rate limit the mass sensitivity scaling to  $\langle m_\nu \rangle \propto 1/(Nt)^{1/4}$  [18]. The neutrino mass sensitivity can be improved in both cases by increasing  $N$ , but eliminating background events leads to a much larger gain with  $N$ . The detection of the barium daughter ion in the decay will lead to essentially background free detection of the  $0\nu\beta\beta$  decay, since all other background events, other than the  $2\nu\beta\beta$  decay, can be rejected if the barium ion is not detected. The expected mass sensitivity of EXO-200 after two years of running is 109 meV [16]. The nEXO experiment is expected to have a mass sensitivity below 10 meV [16]. Experiments with barium ion tagging would explore neutrino mass in the range from 4 to 10 meV.

If nEXO has the projected sensitivity, it may be able to determine if the mass hierarchy of neutrinos is normal or inverted. Figure 1.6 shows values of the effective neutrino mass  $m_\nu$  as a function of the lightest neutrino mass in the normal and inverted hierarchy. If the effective Majorana mass is shown to be less than  $10^{-2}$  eV, then it could be concluded that the neutrino mass hierarchy is normal. This is one of the reasons why nEXO is aiming to have mass sensitivity in this range. With barium tagging even higher sensitivities may be achieved. Exploration of part of normal hierarchy regime may be possible.

The EXO collaboration is currently working on the development of different barium ion detection techniques. The direct daughter of the  $0\nu\beta\beta$  decay is  $\text{Ba}^{++}$ . It is expected that  $\text{Ba}^{++}$  will neutralize to  $\text{Ba}^+$ , or possible even  $\text{Ba}$ , when the ion is in liquid xenon [14]. Our research group at Colorado State University is exploring the detection of a single  $\text{Ba}^+$  or a single neutral  $\text{Ba}$  atom in solid xenon. The idea is to freeze the ion at the end of a cold probe

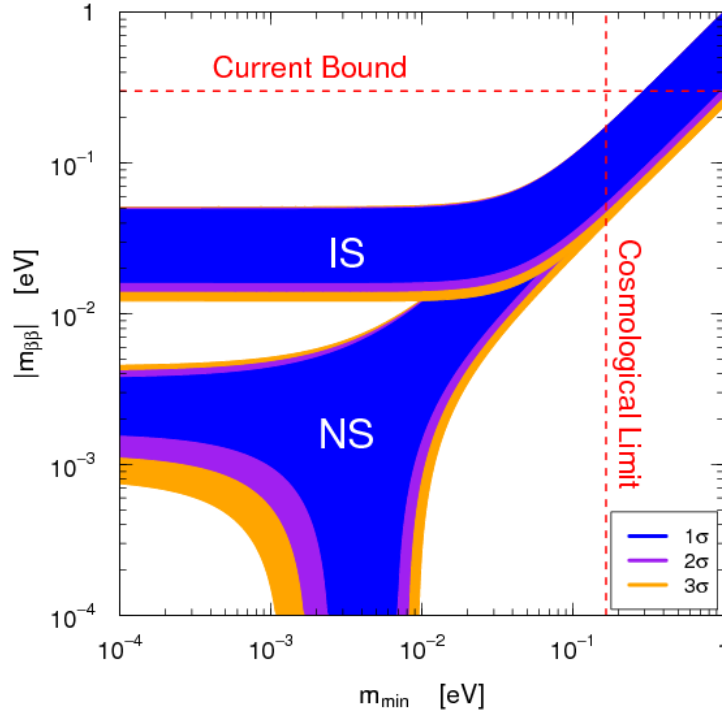


**Figure 1.6:** Effective neutrino mass as a function of the minimum neutrino mass. Figure reprinted from [6]

and then use laser induced fluorescence to detect the  $\text{Ba}^+$  ion or Ba atom. Previous efforts have been reported in the theses of Brian Mong, Kendy Hall and Shon Cook [19, 20, 21]. Another detection method pursued by one EXO collaborator at Stanford is to grab the  $\text{Ba}^+$  ion from liquid xenon on a metal or semiconductor surface without freezing. The barium ion is likely to neutralize on the probe, but it can be desorbed from the probe after removal from the probe to vacuum and then resonantly ionized for detection.

The EXO collaboration is also considering the operation of a gas phase TPC in parallel to the liquid phase TPC. The Carleton group in Canada has built a gas TPC prototype that operates between 1 and 10 bar with volume of  $1 \text{ m}^3$  [22]. The final design of a gas phase TPC is expected to run at pressures between 5 and 10 atm in a chamber with a volume of  $40 \text{ m}^3$  that would contain 1 to 2 tons of xenon [18].  $\text{Ba}^+$  might be detected directly by using laser induced fluorescence in gas phase. In gas, the optical transition of  $\text{Ba}^+$  broadens. In order to assess the possibility of  $\text{Ba}^+$  detection in Xe gas, the pressure broadening must be measured.

Detecting the barium ions in gas would bypass the problem of loading and unloading it from a probe.

The research presented in this thesis discusses the formation of  $\text{BaXe}^+$  molecules in high pressure xenon gas and measurements of fluorescence of  $\text{Ba}^+$  ions in xenon gas. Knowing what happens to barium ions in high pressure xenon is important in order to have a better understanding of  $\text{Ba}^+$  detection in a high pressure xenon gas detector.

One of the proposed methods by the EXO collaboration for tagging barium ions in high pressure gas detector is to extract the barium ion from inside the TPC to a low pressure chamber using a nozzle and an RF carpet ion guide. The ion is guided inside the high pressure xenon to the nozzle with electric fields. Once the ion is in the low pressure chamber the xenon can be pumped out and the barium ion can be identified in vacuum. Since  $\text{Ba}^+$  in high pressure xenon gas can form  $\text{BaXe}^+$ , one question is whether the ion coming from the nozzle will be an atomic ion or a molecular ion. The probability that  $\text{Ba}^+$  converts to  $\text{BaXe}^+$  is dependent on the xenon pressure. As  $\text{Ba}^+$  travels from high to low pressure xenon gas, the probability that the ion converts to  $\text{BaXe}^+$  could be calculated along its trajectory using the measurements reported in this thesis.

## 2 Theory

The physics background and the theory relevant to the experimental work of this thesis are reviewed in this chapter. First, the energy levels of Barium ions in vacuum are introduced in section 2.1. The concepts of broadening and quenching of the fluorescence of barium ions in gas are explained in section 2.2 and then a three level system model for  $\text{Ba}^+$  is discussed in section 2.3. The widths of the spectral lines are affected by many factors; the processes relevant to this work are Doppler broadening and pressure broadening and are discussed in section 2.4. The theory relevant to understanding how a purity monitor for liquid xenon works is discussed in section 2.5. The theory of ion mobility and the formation of  $\text{BaXe}^+$  molecules and the effect on the mobility measurements are presented in sections 2.6 and 2.7.

### 2.1 Energy Levels of $\text{Ba}^+$ in Vacuum

The lowest energy levels of  $\text{Ba}^+$  and allowed transitions between them are shown in Figure 2.1. There are two strong transitions from the ground state,  $6s\ ^2S_{1/2}$ , to the excited states  $6p\ ^2P_{1/2}$  and  $6p\ ^2P_{3/2}$ , with transition wavelengths of 455.4 and 493.4 nm respectively. Ions excited from the ground state to the 6p states with laser light at these wavelengths can decay from the 6p state back to the ground state or to the 5d metastable states. The decays allowed by the electron dipole selection rules are shown in Figure 2.1 and listed in Table 2.1 with their respective decay rates. The decay rates of these transitions have comparable rates.

**Table 2.1:** Vacuum wavelengths and decay rates of  $\text{Ba}^+$  in vacuum [23].

Transition	Wavelength (nm)	A ( $\text{s}^{-1}$ )
$6p\ ^2P_{3/2} \longleftrightarrow 6s\ ^2S_{1/2}$	455.4	$1.11 \times 10^8$
$6p\ ^2P_{1/2} \longleftrightarrow 6s\ ^2S_{1/2}$	493.4	$9.53 \times 10^7$
$6p\ ^2P_{3/2} \longleftrightarrow 5d\ ^2D_{5/2}$	614.2	$4.12 \times 10^7$
$6p\ ^2P_{3/2} \longleftrightarrow 5d\ ^2D_{3/2}$	585.4	$6.00 \times 10^7$
$6p\ ^2P_{1/2} \longleftrightarrow 5d\ ^2D_{3/2}$	649.7	$3.10 \times 10^7$

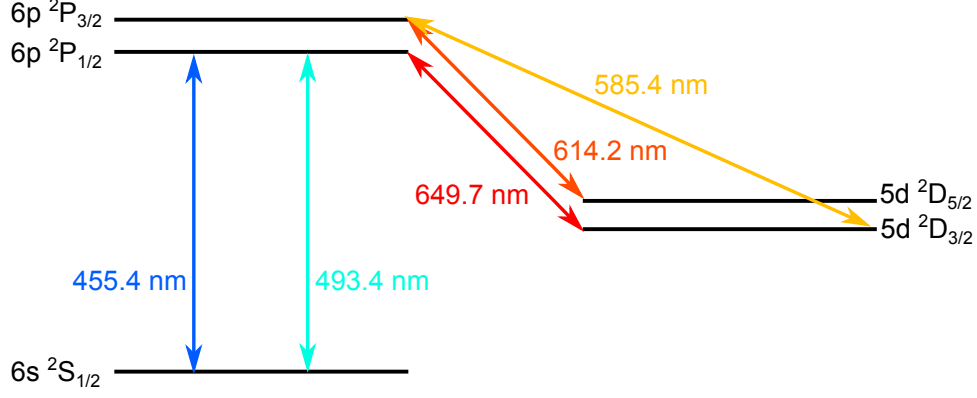


**Figure 2.1:** Energy levels of  $\text{Ba}^+$  in vacuum.

Barium ions spontaneously decay from the metastable states  $5d\ ^2D_{5/2}$  and  $5d\ ^2D_{3/2}$  to the ground state with lifetimes that are very long compared to the allowed transitions. The lifetimes of the metastable states are more than 30 s for the  $5d\ ^2D_{5/2}$  state [24], and 79.8 s for the  $5d\ ^2D_{3/2}$  state, [25] with transition wavelengths in the infrared. The sum of the decay rates is the inverse of the radiative lifetime of a state.

$$\frac{1}{\tau_{rad}} = \sum_{j < 2} A_{2j} \quad (2.1)$$

The branching ratio for a particular transition to state  $i$  is defined by

$$\phi_{21} = \frac{\text{rate of decay from states 2 to 1}}{\text{sum of all decay rates from state 2}} = \frac{A_{2i}}{\sum_j A_{2j}} \quad (2.2)$$

As an example, a branching ratio of 0.245 for  $\text{Ba}^+$  ions decaying from  $6p\ ^2P_{1/2}$  to  $5d\ ^2D_{3/2}$ , emitting 650 nm light, is calculated using the decay rates from Table 2.1.

## 2.2 Atomic Radiation

The excitation rate for an atom from state 1 to state 2 in a system is given by

$$W_{12} = \sigma_{12}(\nu) \frac{I_\nu}{h\nu} \quad (2.3)$$

where  $\sigma_{12}(\nu)$  is the absorption cross section,  $I_\nu$  is the intensity of the excitation laser and  $h\nu$  is the photon. The relative strength of absorption of radiation in the interval  $\nu$  to  $\nu + d\nu$  by atoms in state 1 is given by the line shape function with  $g(\nu)d\nu$ . Different factors contribute to the line shape and width and they will be discussed later in this chapter.

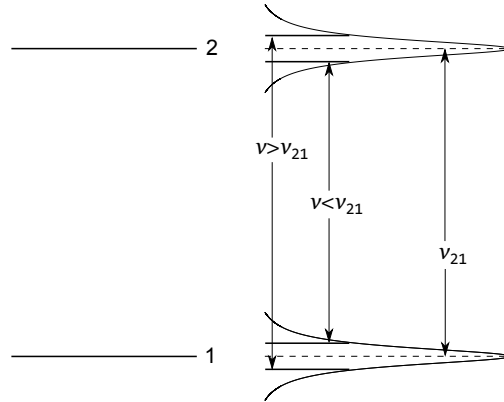


**Figure 2.2:** Transitions in broadened energy levels.

The absorption cross section depends on the line shape function according to

$$\sigma(\nu) = A_{21} \frac{\lambda^2}{8\pi n^2} g(\nu) \quad (2.4)$$

where  $A_{21}$  is the radiative decay rate for the transition,  $\lambda$  is the excitation wavelength and  $n$  is the index of refraction. The absorption cross section  $\sigma$  can be interpreted as the effective cross sectional area of the atom to the photon flux  $I_\nu/h\nu$ .

If  $\text{Ba}^+$  ion in vacuum is excited with 493.4 nm laser light ( $6s \rightarrow 6p$  transition), the ion will decay to the metastable state 5d after a few excitations. The ions will no longer be in resonance with the laser, and as a result, fluorescence will not be observed once the ion is in the metastable state. In this case the ion will need to be repumped from the 5d to the 6p state, using a 649.7 nm laser, to observe fluoresce again. If the ion is in a gaseous environment, the ion may decay from the metastable state back to the ground state due to collisional quenching. The rate constant for collisional de-excitation of the metastables  $D$  states of  $\text{Ba}^+$  in He background pressure was measured by A. Hermanni and G. Werth [26]. They reported a rate constant of  $9.7 \times 10^3 \text{ s}^{-1}/\text{Torr}$ .

In addition to decaying via radiative emission, an excited atom in a radiating state can also undergo nonradiative decay. The total decay rate  $A_{tot}$  on a transition is the sum of the radiative rate  $A_{rad}$  and nonradiative decay rate  $A_{nrad}$ :

$$A_{tot} = A_{rad} + A_{nrad} \quad (2.5)$$

The nonradiative decay rate might be expected to be proportional to gas pressure at constant temperature.

## 2.3 Three Level Model

A barium ion undergoing 493 nm excitation can be modeled as a three level system with states  $|1\rangle$ ,  $|2\rangle$ ,  $|3\rangle$  respectively  $6s\ ^2S_{1/2}$ ,  $6p\ ^2P_{1/2}$  and  $5d\ ^2D_{3/2}$ . A three level system is shown in Figure 2.3. The decay rates are  $A_{21}$ ,  $A_{23}$  and  $A_{31}$ , where  $A_{21}$  is the decay rate from state  $|2\rangle$  to state  $|1\rangle$  and so on. The ion is excited from state  $|1\rangle$  to state  $|2\rangle$  at a rate  $W_{12}$ . The rate equations for this system are

$$\frac{dN_1}{dt} = N_2A_{21} + N_3A_{31} - N_1W_{12} \quad (2.6)$$

$$\frac{dN_2}{dt} = N_1W_{12} - N_2A_{21} - N_2A_{23} \quad (2.7)$$

$$\frac{dN_3}{dt} = N_2A_{23} - N_3A_{31} \quad (2.8)$$

where  $N_1$ ,  $N_2$ , and  $N_3$  are the populations in states  $|1\rangle$ ,  $|2\rangle$ , and  $|3\rangle$  respectively. The conservation of total population of ions  $N$  implies

$$N = N_1 + N_2 + N_3 = \text{constant} \quad (2.9)$$

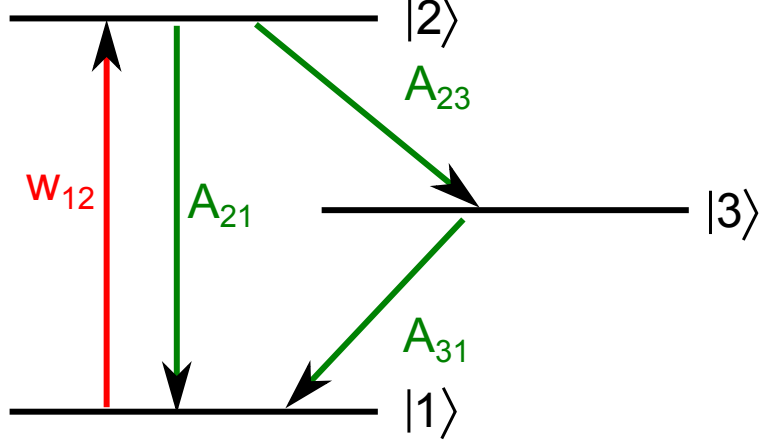


**Figure 2.3:** Three level model for a  $\text{Ba}^+$  ion.

The solution to the rate equations are of the form

$$N_2(t) = C_1 e^{-r_1 t} + C_2 e^{-r_2 t} + B_2 \quad (2.10)$$

$$N_3(t) = C_3 e^{-r_1 t} + C_4 e^{-r_2 t} + B_3 \quad (2.11)$$

The constants  $C_{1,2,3,4}$ ,  $r_{1,2}$  and  $B_{1,3}$  for  $N = 1$  are listed in table 2.2

**Table 2.2:** Constants for the solutions of the rate equations.

$$\begin{aligned}
 r_1 &= \frac{(A_{31}+R) - \sqrt{(A_{31}+R)^2 - 4(RA_{31} + A_{23}W_{12})}}{2} \\
 r_2 &= \frac{(A_{31}+R) + \sqrt{(A_{31}+R)^2 - 4(RA_{31} + A_{23}W_{12})}}{2} \\
 R &= W_{12} + A_{21} + A_{23} \\
 B_2 &= \frac{W_{12}A_{31}}{W_{12}A_{23} + A_{31}R} & B_3 &= \frac{W_{12}A_{23}}{W_{12}A_{23} + A_{31}R} \\
 C_1 &= \frac{r_2 B_2 - W_{12}}{r_1 - r_2} & C_2 &= \frac{-r_1 B_2 + W_{12}}{r_1 - r_2} \\
 C_3 &= \frac{r_2 B_3}{r_1 - r_2} & C_4 &= -\frac{r_1 B_3}{r_2 - r_1}
 \end{aligned}$$

The time dependence of  $N_2$  for different  $W_{12}$  and  $A_{31}$  values is shown in Figure 2.4. The value of the rate constant for collisional quenching of metastable  $\text{Ba}^+$  in He to the ground state, i.e.,  $A_{31} = 3.9 \times 10^5 \text{ s}^{-1}$  and  $A_{31} = 1.9 \times 10^6 \text{ s}^{-1}$  for pressures of 40 and 200 Torr, and the excitation rates  $W_{12} = 10^6 \text{ s}^{-1}$  and  $W_{12} = 10^7 \text{ s}^{-1}$ , respectively, are used in these plots. The

steady state is approached faster for higher  $W_{12}$  and  $A_{31}$ ; the population is lower at steady state for lower  $W_{12}$  and lower  $A_{31}$ , as given in the expression for  $B_2$ .

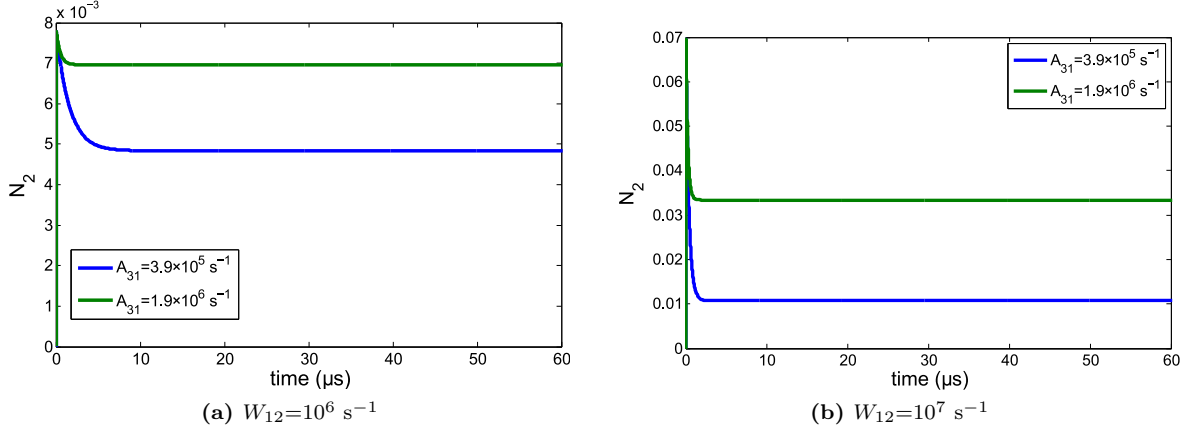


**Figure 2.4:** Population of state two as a function of time for two different  $W_{12}$  values, using the values  $A_{21} = 9.53 \times 10^7 \text{ s}^{-1}$   $A_{23} = 3.1 \times 10^7 \text{ s}^{-1}$ , which are the decay rates of  $\text{Ba}^+$  in vacuum.

## 2.4 Broadening of Spectral Lines

There are two classes of spectral line broadening, homogeneous and inhomogeneous line broadening. A line broadening mechanism is referred as *homogeneous* when it broadens the line of each atom in the same way. In this case, the lineshape of the single atom cross section and that of the overall absorption cross section are identical. On the other hand, a line broadening mechanism is said to be *inhomogeneous* when it distributes the atomic resonance frequencies over some spectral range. Such mechanism thus broadens the line of the overall system without necessarily broadening the lines of individual atoms [27]. Various broadening mechanisms relevant to this thesis are discussed in this section.

### 2.4.1 Natural Line Broadening

In the rest frame in vacuum, atomic transitions have a Lorentzian line shape function given by,

$$g(\nu) = \frac{\Delta\nu}{2\pi[(\nu_0 - \nu)^2 + (\Delta\nu/2)^2]} \quad (2.12)$$

and are homogeneously broadened. For a two level system in vacuum,  $\Delta\nu$  is given by,

$$\Delta\nu = \frac{A_{21}}{2\pi} \quad (2.13)$$

This is called natural line broadening. In this case, the normalized lineshape function on resonance is

$$g(\nu_0) = \frac{4}{A_{21}} \quad (2.14)$$

## 2.4.2 Pressure Broadening

When collisions occur between gas phase atoms or molecules there is an interaction energy that changes the transition frequency for a short period of time. The collisions therefore interrupt the phase of the wave function. The atoms no longer emit a monochromatic wave. This results in a broadening of the lineshape of the transition.

The time between collisions  $t$  it is not constant.  $P(t)dt$  represents the probability that an atom suffers a collision after a time interval  $t$  between  $t$  and  $t+dt$  after the previous collision. For random collisions the probability is

$$P(t)dt = \frac{1}{\tau_0} e^{-t/\tau_0} dt \quad (2.15)$$

where  $\tau_0$  represents the mean time between the collisions. The frequency  $\nu_0$  is interrupted by phase randomizing collisions, which causes a frequency spread. The line shape of the emitted light is calculated by multiplying distribution of frequency by  $P(t)dt$  and integrating from 0 to  $\infty$  [28]. The normalized spectral line shape is given by:

$$g(\nu) = \frac{\Delta\nu_p}{2\pi[(\nu_0 - \nu)^2 + (\Delta\nu_p/2)^2]} \quad (2.16)$$

where  $\Delta\nu_p$  is

$$\Delta\nu_p = \frac{1}{\pi\tau_0} \quad (2.17)$$

The line shape is a Lorentzian, like a natural line broadening, with linewidth  $\Delta\nu_p$ . As the number density of atoms in the gas increases, the time between collisions decreases and the linewidth increases. One would expect the linewidth to increase linearly with the pressure. Typical values for pressure broadening are around 10 to 20 MHz/torr [27]. When two broadening mechanisms contribute to line broadening, the overall lineshape is given by the convolution of the two lineshape functions. In the case of two homogeneous broadening mechanisms, e.g., natural broadening and pressure broadening, both with a Lorentzian lineshape and widths  $\Delta_N$  and  $\Delta_p$  respectively, the convolution of the two Lorentzians again gives a Lorentzian with a total width  $\Delta_T = \Delta_N + \Delta_p$ .

### 2.4.3 Doppler Broadening

Doppler broadening arises from the motion of atoms. If an atom that emits a frequency  $\nu_0$  in its rest frame is moving towards an observer in the laboratory with a velocity  $v_z$ , then the observer would measure the Doppler shifted frequency

$$\nu'_0 = \nu_0 \left(1 + \frac{v_z}{c}\right) \quad (2.18)$$

For a gas in thermal equilibrium there is a distribution of velocities both toward and away from the observer. The net effect is a broadened line shape function.

The homogeneous shape function for an atom moving at longitudinal velocity  $v_z$  is, from equations (2.12) and (2.18),

$$g(v_z, \nu) = \frac{\Delta\nu_h}{2\pi[(\nu - \nu_0 - \nu_0 v_z/c)^2 + (\Delta\nu_h/2)^2]} \quad (2.19)$$

The probability  $p_v dv_z$  that an atom of mass  $M$  in a gas at temperature  $T$  has a velocity component between  $v_z$  and  $v_z + dv_z$  is given by

$$p_v = \left(\frac{M}{2\pi kT}\right)^{1/2} \exp[-(Mv_z^2/2kT)] \quad (2.20)$$

where  $M$  is the mass of the atom,  $T$  is the gas temperature and  $v_z$  is the  $z$  component of the velocity. The line shape function for all atoms is obtained by multiplying (2.19) by  $p_v dv_z$  and then integrating over  $v_z$ .

$$g(\nu) = \left(\frac{M}{2\pi kT}\right)^{1/2} \int_{-\infty}^{+\infty} \left\{ \frac{\Delta\nu_h}{2\pi[(\nu - \nu_0 - \nu_0 v_z/c)^2 + (\Delta\nu_h/2)^2]} \right\} \times \exp[-(Mv_z^2/2kT)] dv_z \quad (2.21)$$

This function is called the Voigt function.

In the special case that  $\Delta\nu_h$  is much smaller than a typical Doppler shift, the Lorentzian can be approximated by a delta function. Thus integrating (2.21) gives

$$g(\nu) = \frac{1}{\nu_0} \left(\frac{Mc^2}{2\pi kT}\right)^{1/2} \exp\left[\left(-\frac{Mc^2}{2kT}\right) \left(\frac{\nu - \nu_0}{\nu_0}\right)^2\right] \quad (2.22)$$

The line shape is a Gaussian with a peak value at  $\nu_0$  and full width half maximum (FWHM) Doppler width of

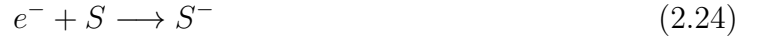
$$\Delta\nu_D = 2\nu_0 \left(\frac{2kT \ln 2}{Mc^2}\right)^{1/2} \quad (2.23)$$

If the the homogeneous width is much greater than the Doppler width, the function  $p_v$  can be replaced by a delta function centered at  $v_z=0$ . Thus the homogeneous line shape equation (2.16) is recovered. An atomic transition is dominated by Doppler broadening in a typical low pressure gas at room temperature. If, however, the pressure is high enough, pressure broadening will dominate [27].

## 2.5 Theory of Liquid Xenon Purity Monitor

It is important to have high purity liquid xenon to ensure the survival of  $\text{Ba}^+$  ions and electrons in the EXO detector and in our barium tagging test apparatus. Thus a way to quantitatively measure the purity level of the liquid xenon is needed.

Free electrons in liquid xenon can become attached to electronegative impurities. The negative ions move orders of magnitude more slowly and therefore have a much reduced current that can be neglected. The reaction describing the electron attachment to impurity atoms is given by



The rate of electrons lost is given by the equation

$$\frac{dN(t)}{dt} = -k_s[X]N(t) \quad (2.25)$$

where  $[X]$  is the the concentration of electronegative impurities,  $N(t)$  is the number of free electrons at time  $t$ , and  $k_s$  is the electron attachment rate [29]. After integrating equation (2.25)

$$N(t) = N_0 \exp(-t/\tau_e) \quad (2.26)$$

where  $N_0$  is the initial number of electrons. The electron lifetime  $\tau_e$  is inversely proportional to the concentration of electronegative impurities:

$$\tau_e = \frac{1}{k_s[X]} \quad (2.27)$$

The electron attachment rate constant  $k_s$  depends on the type of impurity and on the strength of the electric field. Studies of the attachment of electrons to  $O_2$ ,  $SF_6$  and  $N_2O$  in liquid xenon as a function of electric field were done by Bakale et al. [30].

### 2.5.1 ICARUS Purity Monitor

The liquid xenon purity monitor for the barium tagging apparatus at CSU is based on the design of the liquid argon (LAr) purity monitor for the ICARUS experiment, a very large TPC filled with ultra-pure liquid Ar aimed to study neutrino oscillations at Gran Sasso. The electron lifetime in LAr was determined in the ICARUS purity monitor by measurement of

the attenuation of an electron cloud moving in a small drift chamber filled with a sample of LAr [31].

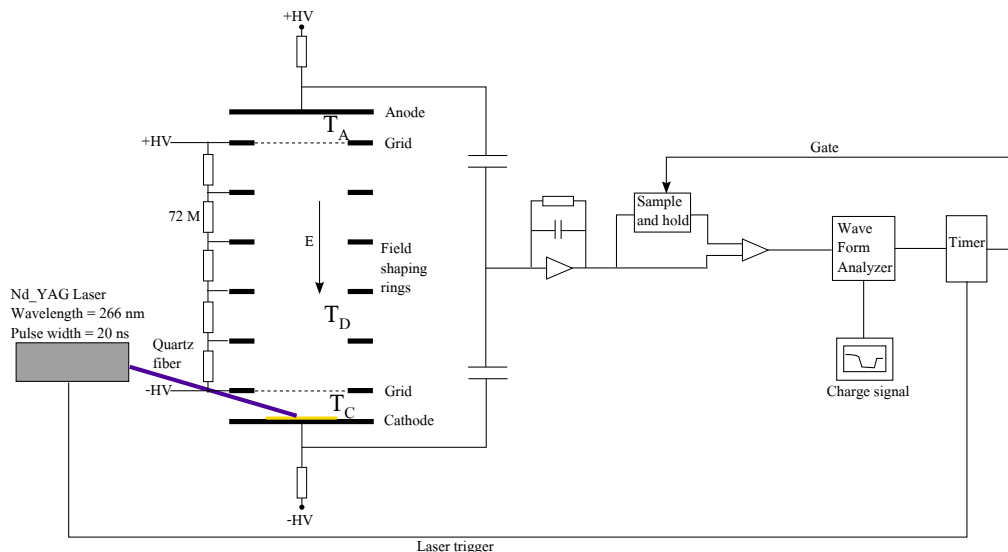


**Figure 2.5:** Schematic drawing of the ICARUS purity monitor. Redrawn from [31]

A diagram of ICARUS purity monitor is shown in Figure 2.5. It is a double gridded drift chamber with a drift length of 6.5 cm. An electron cloud is created via the photoelectric effect on the gold plated cathode by a pulsed Nd-YAG laser. The light is brought to the photocathode through a quartz optical fiber. In order to drift the electrons from the cathode to the anode, a high voltage is applied between the anode and the cathode with intermediate voltages on the two grids. As the electrons drift through the chamber, a percentage is lost by attaching to electronegative impurities. By measuring the ratio of the charge created at the cathode to the charge arriving to the anode, the electron lifetime in the liquid can be determined using equation (2.26). The concentration of electronegative impurities can be deduced from the electron lifetime using equation (2.27).

## 2.6 Ion Mobility

When a weak electric field is applied to group of ions in gas, they will travel with constant velocity parallel to the field lines, with the electric force balanced by a frictional force from

the medium. The average drift velocity of the ions  $v$ , is proportional to the electric field  $E$ :

$$v = \mu E \quad (2.28)$$

where the proportionality constant  $\mu$  is called the ion mobility. To compare data taken at different gas pressures and temperatures a "reduced" mobility extrapolated to zero field strength is calculated by

$$\mu_0 = \frac{p}{760} \frac{273.15}{T} \mu \quad (2.29)$$

where  $p$  is the gas pressure in Torr and  $T$  is the gas temperature in Kelvin [32].

At low electric field to gas number density,  $E/N$ , the ionic mobility is constant; however, at high electric fields the mobility is no longer constant. The ratio  $E/N$  determines whether the electric field is weak or strong. A unit of  $E/N$ , is the Townsend, or Td, such that 1 Td =  $10^{-17} \text{V}\cdot\text{cm}^2$ . The mobility of  $\text{Ba}^+$  in rare gases was calculated by M. F McGuirk et al. [33] using *ab initio* potential energy curves for  $\text{Ba}^+$  interacting with rare gas atoms. Their results predict that for values of  $E/N < 10$  Td the mobility of  $\text{Ba}^+$  in Xe gas is constant.

The friction force on the gas of an ion cloud with a large enough charge can cause a net fluid motion that will affect a mobility measurement. This effect is seen with charge as small as 10-20 pC. The ions then have an apparent mobility  $\mu_{app}$  that depends on the charge. For liquid xenon, the following empirical equation was found: [34]

$$\mu_{app} = \mu_{true} + cQ^{n(E)} \quad (2.30)$$

The power  $n$  of the  $Q$  dependence is on the order of 0.5-2.0 and depends somewhat on the electric field;  $c$  is a constant.

It is important to measure the mobility of  $\text{Ba}^+$  in Xe gas for potential applications of  $\text{Ba}^+$  tagging in a next generation EXO detector. For analyzing fluorescence experiments of  $\text{Ba}^+$  in Xe gas, the velocity of the ions through the excitation laser is needed. The results of

mobility are also used to determine the relative rate of association and dissociation reactions between ions and gas atoms, as discussed below.

## 2.7 Molecular Ion Formation

$\text{Ba}^+$  ions can be removed or recovered by the following reactions in Xe gas:

1) Three body association, or termolecular ion-neutral association, reaction



2) collisional dissociation



The reaction (2.32) is the same as (2.31) but in the opposite direction.

### 2.7.1 Termolecular Association

The association reaction rate  $R_{assoc}$  is proportional to the square of the gas number density  $[\text{X}]$ :

$$R_{assoc} = k_{assoc}[\text{X}]^2 \quad (2.33)$$

where  $k_{assoc}$  is the association rate constant [35]. Measured rate constants for some termolecular reactions are shown in Table 2.3.

These rates are on the order of  $10^{-31} \text{ cm}^6/\text{s}$ . Thus as an initial guess, we take the association rate for reaction (2.31) to be  $k_{assoc} \approx 10^{-31} \text{ cm}^6/\text{s}$ . At one atmosphere, or a gas density of  $[\text{X}] = 2.69 \times 10^{19} \text{ cm}^{-3}$ , the association rate is  $R_{assoc} = 7 \times 10^7 \text{ s}^{-1}$ . This means that the association reactions occur in a time on the order of 10 nanoseconds at atmospheric pressure.

**Table 2.3:** Measured association rates for some rare gas atomic ions in rare gas and metal ions in atmospheric gases at a temperature of 300 K [35, 36].

Termolecular reaction	$k_{assoc}$ (cm <sup>6</sup> /s)
$\text{Ar}^+ + \text{Ar} + \text{Ar} \longrightarrow \text{Ar}_2^+ + \text{Ar}$	$1.2 \pm 0.2 \times 10^{-31}$
$\text{Kr}^+ + \text{Kr} + \text{Kr} \longrightarrow \text{Kr}_2^+ + \text{Kr}$	$2.1 \pm 0.9 \times 10^{-31}$
$\text{Xe}^+ + \text{Xe} + \text{Xe} \longrightarrow \text{Xe}_2^+ + \text{Xe}$	$1.48 \pm 0.18 \times 10^{-31}$
$\text{Ca}^+ + \text{H}_2 + \text{H}_2 \longrightarrow \text{CaH}_2^+ + \text{H}_2$	$5.3 \times 10^{-31}$
$\text{Ca}^+ + \text{N}_2 + \text{N}_2 \longrightarrow \text{CaN}_2^+ + \text{N}_2$	$1.5 \times 10^{-31}$
$\text{Mg}^+ + \text{H}_2 + \text{H}_2 \longrightarrow \text{MgH}_2^+ + \text{H}_2$	$6.3 \times 10^{-31}$

## 2.7.2 Collisional Dissociation

In collisional dissociation, molecular ions are fragmented during collisions with gas atoms. The temperature dependence of the dissociation rate constant  $k_{dissoc}$  is given by Petrie et al. [36] as an Arrhenius type equation  $k = A \exp(-E_a/k_B T)$ , where  $A$  is the pre-exponential factor,  $E_a$  is the activation energy,  $k_B$  is the Boltzmann constant and  $T$  is the temperature. For collisional dissociation estimates, the pre-exponential factor used by Petrie et al. is  $1 \times 10^{-9} \text{ cm}^3 \text{ s}^{-1}$ . The collisional dissociation rate constant is then

$$k_{dissoc} = 1 \times 10^{-9} \text{ cm}^3 \text{ s}^{-1} e^{-(D_0/k_B T)} \quad (2.34)$$

where  $D_0$  is the dissociation energy of the molecular ion or binding energy. Values of  $D_0$  for different molecular species can be found in [35, 36]. The dissociation rate is proportional to the gas density  $[X]$

$$R_{dissoc} = k_{dissoc} [X] \quad (2.35)$$

For  $\text{BaXe}^+$ ,  $D_0 = 0.191 \text{ eV}$  [33]. Thus at atmospheric pressures and room temperature  $k_{dissoc} = 6.1 \times 10^{-13} \text{ cm}^3 \text{ s}^{-1}$  and  $R_{dissoc} = 1.5 \times 10^7 \text{ s}^{-1}$ . The dissociation reactions occur in a

time on the order of 60 nanoseconds at atmospheric pressure, approximately six times slower than the association reactions, with the estimated rates.

### 2.7.3 Fraction of Atomic Ions

The termolecular association and collisional dissociation reactions take place in the order of nanoseconds. The drift time of the ions during the mobility measurements is on the order of microseconds. Thus many association and dissociation reactions occur during the ion drift. After a number of reactions, the ratio of molecular ions to atomic ions reaches a steady state that depends on the ratio of  $R_{dissoc}$  to  $R_{assoc}$ , the temperature and the pressure of the gas:

$$\frac{[MX^+]}{[M^+]} = \frac{R_{assoc}}{R_{dissoc}} = \frac{k_{assoc}[X]^2}{k_{dissoc}[X]} = \frac{k_{assoc}}{k_{dissoc}}[X] \quad (2.36)$$

The gas number density is related to the pressure of the gas and the temperature by

$$[X] = (2.69 \times 10^{19} \text{ cm}^{-3}) \left( \frac{273.15 \text{ K}}{T} \right) \left( \frac{p}{760 \text{ Torr}} \right) \quad (2.37)$$

Thus

$$\frac{[MX^+]}{[M^+]} = \frac{k_{assoc}}{k_{dissoc}} (2.69 \times 10^{19} \text{ cm}^{-3}) \left( \frac{273.15 \text{ K}}{T} \right) \left( \frac{p}{760 \text{ Torr}} \right) \quad (2.38)$$

The fraction of atomic ions decreases as the pressure increases. The fraction of atomic ions  $f_{M^+} = [M^+]/([M^+] + [MX^+])$  can be written in terms of pressure (in Torr):

$$\frac{[M^+]}{[M^+] + [MX^+]} = \frac{1}{1 + bp} \quad (2.39)$$

where

$$b = \frac{k_{assoc}}{k_{dissoc}} \left( \frac{2.69 \times 10^{19} \text{ cm}^{-3}}{760 \text{ Torr}} \right) \left( \frac{273.15 \text{ K}}{T} \right) \quad (2.40)$$

As an example, the percentage of  $Ba^+$  ions in Xe gas and the percentage of  $Ba^+$  in Ar gas at 1 atm, and room temperature using the order of magnitude estimates of the reaction rates given above are compared in Table 2.4.

**Table 2.4:** Order of magnitude estimates of the percentage of  $\text{Ba}^+$  atomic ions in xenon gas at 1 atmosphere and room temperature.

Ion	Gas	$D_0$ (eV)	$k_{dissoc}$ ( $\text{cm}^3/\text{s}$ )	$k_{assoc}$ ( $\text{cm}^6/\text{s}$ )	$f_{M^+}$
$\text{Ba}^+$	Ar	0.0824	$4 \times 10^{-11}$	$10^{-31}$	0.94
$\text{Ba}^+$	Xe	0.191	$6 \times 10^{-13}$	$10^{-31}$	0.20

At atmospheric pressures, molecular ions dominate in Xe gas, while in Ar the atomic ions are the prevalent species assuming the estimated rate constants. This difference is a result of the smaller binding energy of  $\text{BaAr}^+$  than  $\text{BaXe}^+$ .

Molecular formation will have an effect on the mobility measurements. The ions traveling in gas will be a mixture of molecular and atomic ions, so the measured mobility will be a weighted average of the mobility of the molecular and atomic ions. At lower pressures the atomic ions will be the prevalent species and the measured mobility will be closer to the value of the atomic mobility. At high pressures the molecular ions will dominate and the overall effect will be a decrease in the mobility, since the larger molecular ions experience more friction and travel at a slower velocity. For  $\text{Ba}^+$  in Ar at 1 atm only a small decrease in the mobility from the ionic mobility value is expected because the percentage of atomic ions is still close to 100%. In Xe gas at 1 atm the predicted dominant species is  $\text{BaXe}^+$ , and it is expected that the measured mobility will be closer to that of  $\text{BaXe}^+$ .

## 3 Apparatus

In this chapter the apparatus used to perform the purity measurements in liquid xenon and the mobility and fluorescence experiments in gas is described, and basic procedures and experiments characterizing the apparatus are presented. The main part of the system consists of a Xe cell, a cryogenic system inside an ultra high vacuum chamber, and a gas handling system which is used supplies Xe gas to the cell and also serves as a recirculation and purification system. An electrode system, inside the Xe cell, is used for purity measurements. The same set of electrodes is used to drift the  $\text{Ba}^+$  ions in the mobility and fluorescence experiments. The detection of electron and  $\text{Ba}^+$  ion current signal is discussed in this chapter.

### 3.1 Xenon System

The Xe system has been used previously for mobility measurements of alkaline earth ions drifting in LXe [37, 34] and fluorescence experiments of  $\text{Ba}^+$  in LXe [20]. Several improvements and modifications have been made to the system through the years to accommodate the needs of the different experiments done with the system. A diagram of the Xe system is shown in Figure 3.1.

The Xe cell is inside an ultra-high vacuum chamber. The cell is connected to the gas handling part of the system which supplies purified Xe gas. The vacuum chamber, the Xe cell and the transfer lines of the gas handling system are all evacuated by a turbo pump. After the system is evacuated, the valve between the outer vacuum and the Xe cell is closed. Xe gas is then supplied to the cell from Xe bottles installed in the gas handling part of the system. The xenon gas goes through particle filters and a gas purifier before it is delivered to the Xe cell.

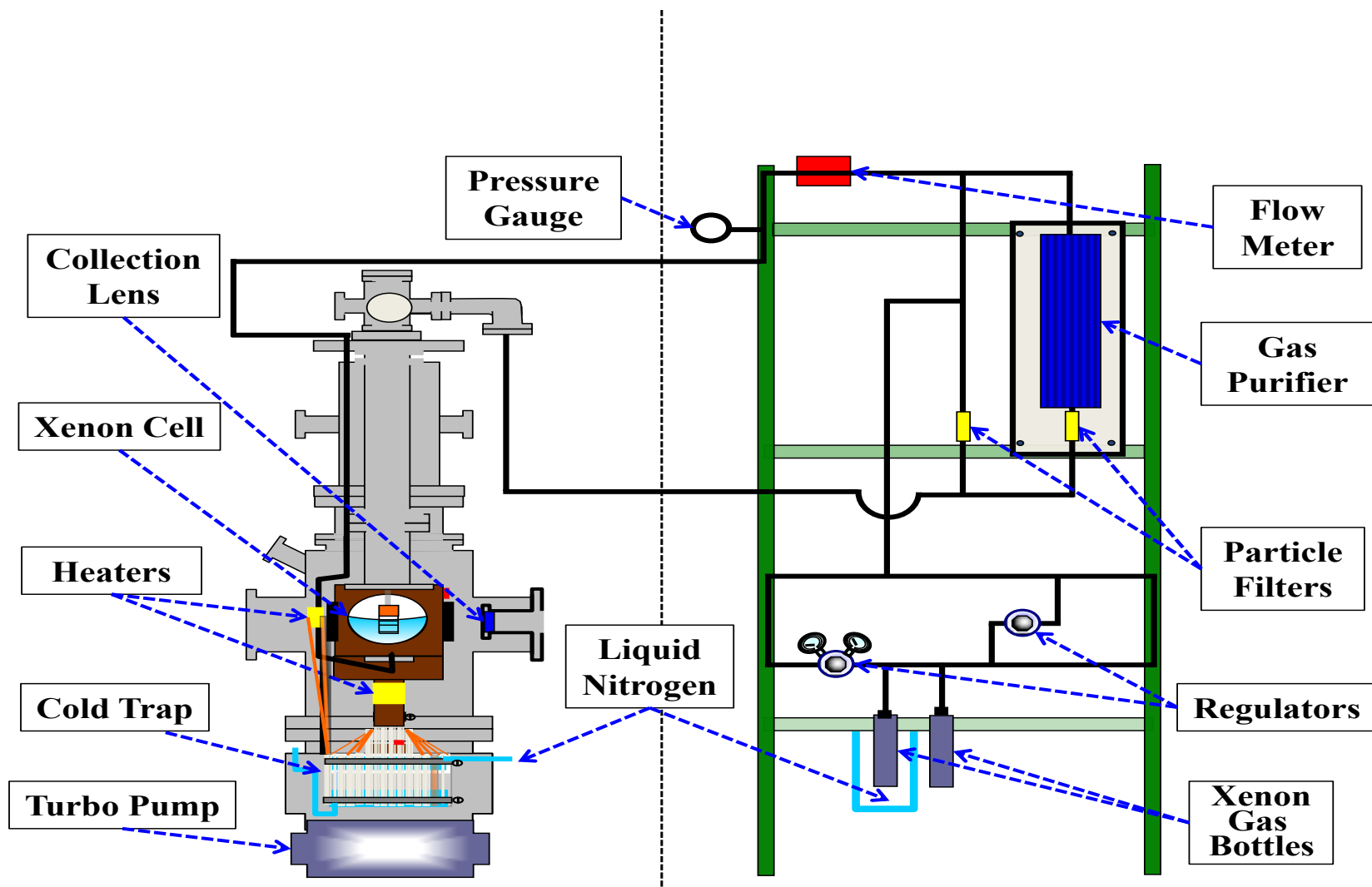


Figure 3.1: Xenon system.

A liquid nitrogen cold trap at the bottom of the outer vacuum chamber is used to cool down the Xe cell to around 170 K when experiments involving liquid xenon are performed. Power to the heaters on the Xe cell and the stainless steel pipe used for recirculation and recovery of xenon control their temperatures. A pressure gauge at the top of the systems reads the pressure inside the Xe cell. A flowmeter is used to measure the xenon gas flow when it is recirculated through the purifier. A lens mounted in a penetration nipple in the outer vacuum chamber collects light for fluorescence experiments.

### 3.1.1 Xenon Cell

The Xe cell is a made of copper block of size 3.82 in  $\times$  3.82 in  $\times$  5.11 in. The cell has four windows sealed with indium wires. The purpose of the windows is to have optical access to the inside of the cell. The top of the cell is connected to the Xe gas handling system by stainless steel tube. The bottom part is connected to a stainless steel flange that has a recirculation pipe welded to it. Both the bottom and the top part of the cell are sealed with indium wires. The seals are done based on the design of windows for low temperature and moderate pressures by Lim [38]. To seal the windows, the cell was heated to about 105°C in a home made oven to help the indium to flow between the window and the copper. The bolts of the windows were tightened with a torque of 7.5 ft-lb on each bolt with a criss-cross pattern while the copper cell was hot. The window seals are designed to withstand pressures up to 2 atmospheres. The seals of the windows were leak checked with a helium leak detector. Prior to a leak check, the cell was evacuated and then a leak test was done on each seal by spraying small amounts of helium from the outside. The total leak rate of the cell was estimated to be about  $4 \times 10^{-8}$  atm cm<sup>3</sup>/s. While doing experiments with liquid xenon, the pressure inside the cell can go up to 2 atm; this would result in a leak rate of  $7 \times 10^{-3}$  standard cm<sup>3</sup>/day assuming equal leak rates for inside pressurized versus outside pressurized. The amount of xenon lost per day is negligible compared with the 86 standard liters of xenon used during the experiment.

After the seals are leak checked, a high pressure test is done to verify that the cell can hold gas pressures of 1 to 2 atmospheres. In a high pressure test, the cell is filled with 1 to 2 atmospheres of argon or xenon gas while the vacuum chamber is kept under vacuum. The vacuum pressure of the chamber is measured with an ionization gauge, before and after the cell is filled with gas. The typical pressure of the outer vacuum chamber before gas is inserted in the copper cell is about  $10^{-8}$  Torr. With Xe gas deposited in the cell, the pressure of the outer vacuum chamber rises to about  $3 \times 10^{-7}$  Torr at 1 atm of xenon, and about  $7 \times 10^{-7}$  Torr when the pressure in the cell is 2 atm. If the pressure of the chamber rises to a pressure higher than  $10^{-6}$  Torr, that is an indication of the presence of a significant leak. With the pressure test we only can determine whether a leak exists or not, but its location cannot be identified. On the other hand, the leak test using the helium leak detector can localize a leak to a specific part of the cell. Prior to any experiment involving inserting gas in the cell, as a matter of precaution, a pressure test is performed. The major concerns of a leak are that it could cause the loss of xenon and damage to the turbo pump.

### 3.1.2 Cryogenic System

The triple point temperature of xenon is 161.4 K, and the boiling point at 1 atm is 165.1 K. In order to liquefy xenon at 1 atm pressure, the cell needs to be cooled down to 165 K. This is done using a liquid nitrogen cold trap. The cold trap is thermally connected to the xenon cell by more than 30 copper braided straps. The straps are clamped to the bottom and top of the cold trap. All but two of the braids are then clamped to a copper cylinder which is connected to the bottom of the xenon cell, and the other two copper straps are attached to the recirculation pipe. The cool-down process takes between 12 hours and 24 hours, depending on how tight the copper braided straps are attached to the cold trap. The clamping device becomes loose over time and the copper straps are usually retightened once the cell takes longer than 24 hours to cool down. The cold trap is filled with liquid nitrogen

(LN<sub>2</sub>) every 60 minutes to keep the temperature of the cold trap steady. A typical graph of a cool down process is shown in Figure 3.2

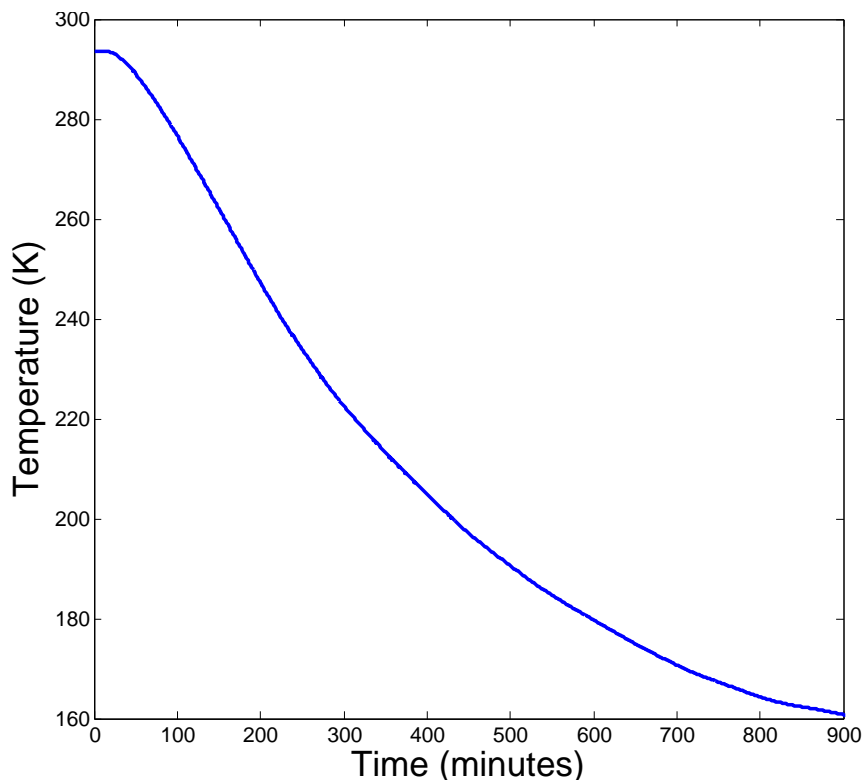


**Figure 3.2:** Typical plot of cooling down of Xe cell. It took 13 hours for the cell to cool down to 165 K for this run

Once the temperature of 165 K is reached, Xe gas is slowly added to the cell, and the pressure inside the cell goes from vacuum to 1 atm. After the pressure exceeds 1 atm, xenon starts to condense inside the cell. During the condensation process the temperature of the cell rises because the xenon gas transfers the latent heat of vaporization to the cell during its liquefaction. This limits the speed of the liquefaction process, because at 178 K the pressure inside the cell increases to 2 atm. If the temperature of the cell goes above 178 K, the flow of xenon gas from the xenon bottle to the cell is manually paused by closing the valve of the xenon bottle. This is done to prevent an increase in pressure and possible damage to the seals of the windows. The liquefaction is resumed once the temperature dips below 170 K.

When the desired liquid level is reached, the temperature of the cell is stabilized to 167 K with the use of a LakeShore 331 temperature controller via a proportional-integral-derivative (PID) loop. The temperature is controlled by sending current to a 25W heater band which is attached to the top part of the copper cylinder that connects the copper cell to the copper straps clamped to the cold trap. The current applied to the heater is regulated by a PID algorithm control that controls the output power based on the temperature of the copper cell relative to the selected setpoint. The sensor used to measure the temperature of the xenon cell is a Lakeshore silicon diode that is spring loaded onto one of the copper window flanges of the xenon cell. Figure 3.3 shows a plot of the temperature of the cell over a period of more than 20 hours. The variation of the temperature of the xenon cell is less than  $\pm 0.1$  K around the set point as long as the cold trap is filled with liquid nitrogen every hour.

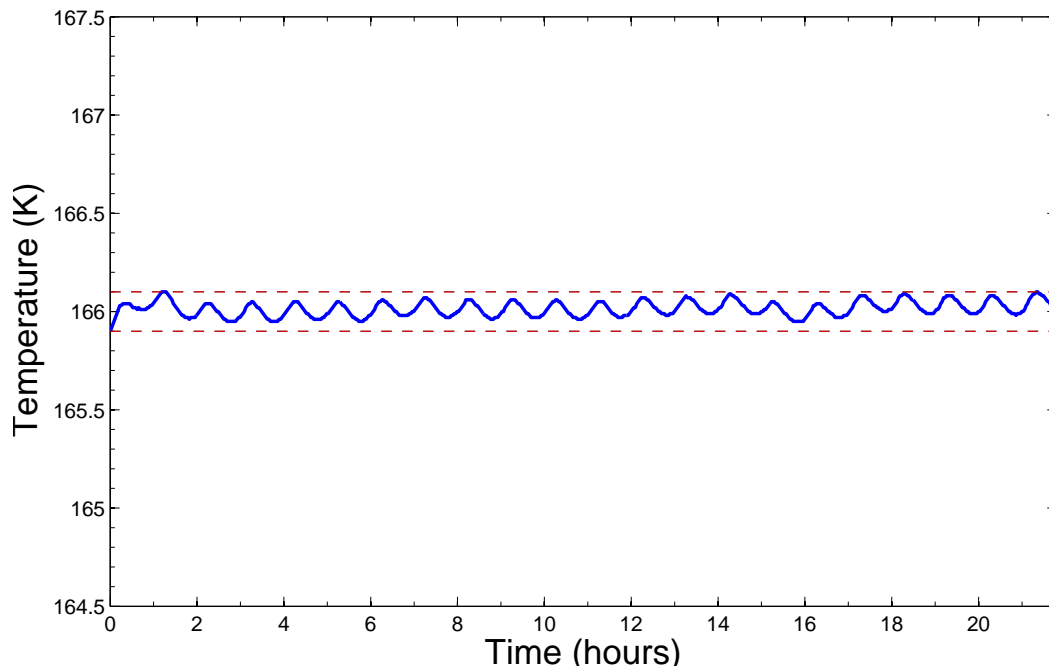


**Figure 3.3:** This plot shows the stability of the temperature of the cell with variations of less than  $\pm 0.1$  K around 166 K, over a period of more than 20 hours. The cold trap was refilled with liquid nitrogen every hour.

The cold trap is filled from a 180 liter LN<sub>2</sub> dewar. The filling of the cold trap is done automatically with the use of a solenoid valve connected to the dewar output. The valve is controlled by a timer programmed to open the solenoid valve for one minute every hour.

The temperature controller has an alarm system which is triggered when the temperature reading is higher than a specified high set point or when the temperature reads below a low set point. The alarm is normally set to trigger at 175 K and 165 K for the high and low set point respectively. If the alarm goes off, it sends a trigger signal to an automatic dialer that calls to the cell phone of the people in charge of the experiment. In the case that the temperature goes below 165 K, the heater is manually turned on to prevent xenon from freezing. If temperature goes above 175 K, liquid nitrogen is manually added to the cold trap to bring the temperature down.

### 3.1.3 Gas Handling and Recirculation System

The main parts of the gas handling system are the xenon bottles, the transfer lines, and the purifier. A schematic diagram of the path of xenon gas from the high pressure bottle to the cell is shown in Figure 3.4. There are two xenon bottles connected to the system; only one of them is used at a time and the other serves as a back up. Each bottle has 100 standard liters of xenon at a pressure of 700 psi. The xenon supplied from the gas bottle goes through a rare gas purifier before it goes into the cell. The purifier is a SAES MonoTorr purifier, model PS3-MT3-R-1, which is designed to remove O<sub>2</sub>, H<sub>2</sub>, CO, CO<sub>2</sub>, H<sub>2</sub>O, CH<sub>4</sub> and N<sub>2</sub> in rare gases to low parts per billion (ppb) levels or below. The purifier uses a patented getter technology that allows irreversible chemical absorption of impurities. The operating temperature of the purifier is between 350° C to 400° C. The inlet and outlet connections of the purifier are ¼" VCR female, which facilitates its installation. A particle filter is installed at the outlet of the purifier. After the xenon gas goes through the purifier and the particle filter, the xenon gas is condensed in the cell.

Once the xenon is condensed in the cell, it can be recirculated through the purifier in a closed loop. A diagram of the recirculation path is shown in Figure 3.5. A ¼" stainless steel pipe for recirculation is welded to the bottom flange of the xenon cell. A heater cartridge is attached to the recirculation pipe, at a position where the liquid level is expected to be.

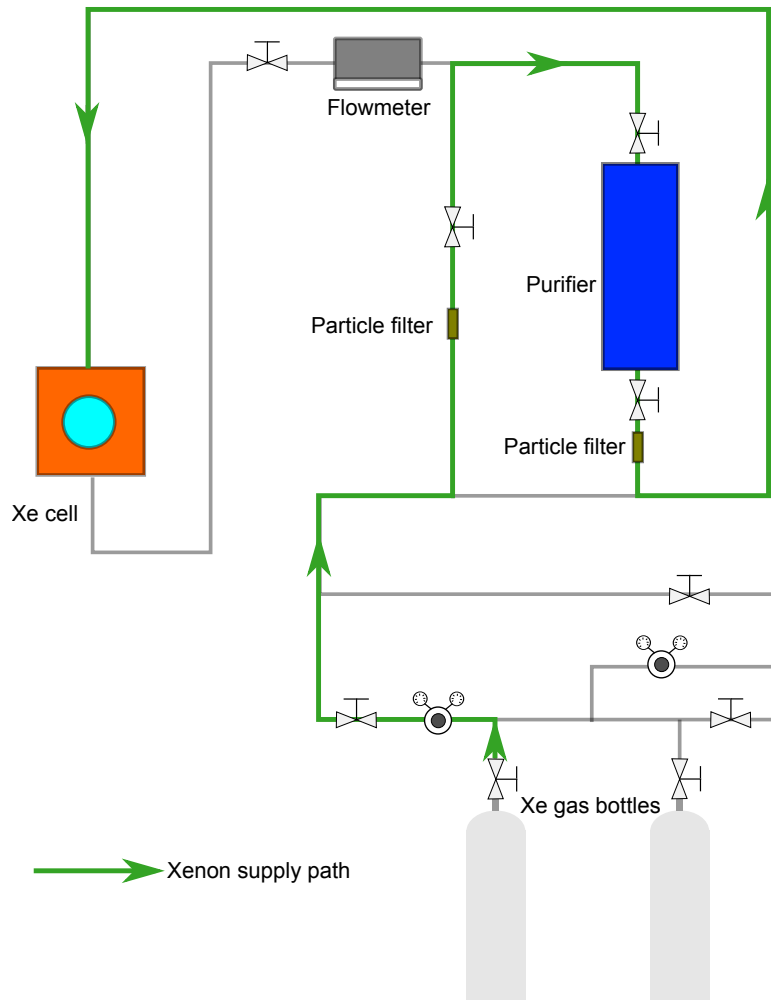


**Figure 3.4:** Simplified diagram of the xenon supply path.

The heater cartridge is thermally connected to the recirculation pipe by placing it between two pieces of copper that clamp both the heater cartridge and the pipe. The cartridge and the pipe are wrapped with indium foil to ensure good thermal contact with the copper. The heater cartridge attached to the recirculation pipe has maximum output power of 10 Watts and is controlled by an external Variac transformer. The output power is manually adjusted to control the temperature of the recirculation pipe; there is no feedback to control the temperature as in the case of the xenon cell temperature. The temperature of the recirculation pipe is kept at about 170 K and it is monitored using a spring loaded silicon detector mounted on the copper block that holds the cartridge.

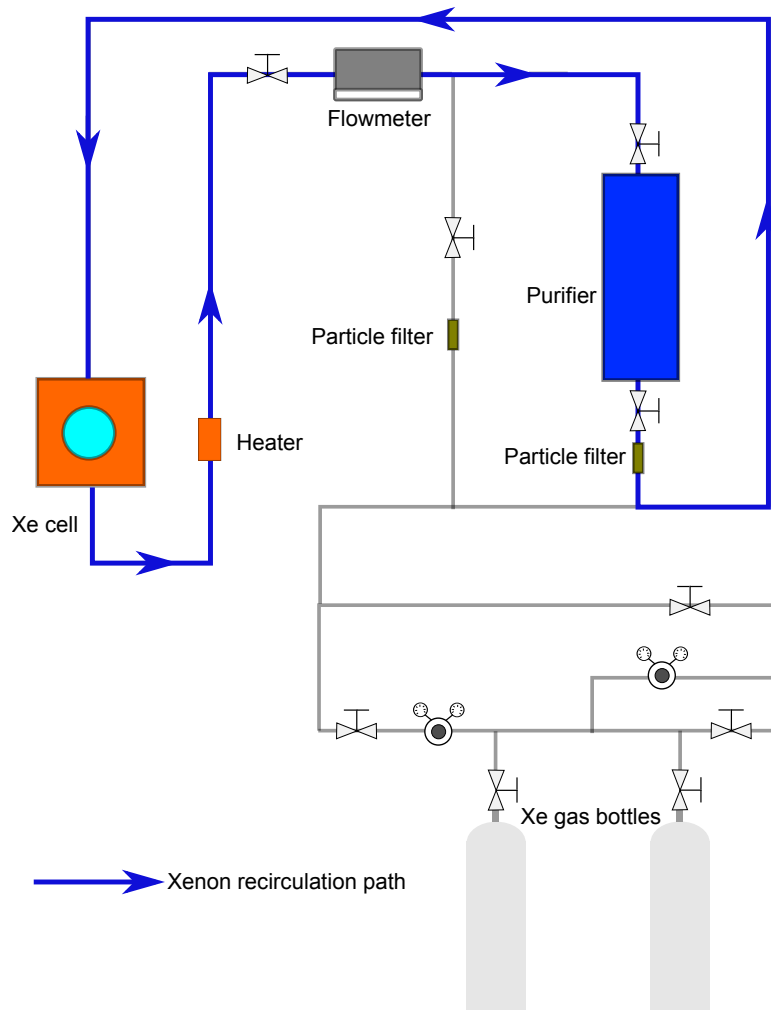


**Figure 3.5:** Simplified diagram of the xenon recirculation path.

The xenon is recirculated by applying heat to the recirculation heater. This is done by increasing the power applied to the heater cartridge attached to the pipe. This evaporates liquid in the recirculation pipe and increases the pressure in the upper recirculation pipe. This forces gas flow through the purifier and back to the xenon cell. The flow is measured with a MKS Type 179A Mass-Flo Meter installed in between the xenon cell and the purifier. The output signal, 0 - 5 V is recorded by a LabView program and converted to a flow rate reading, in standard cubic centimeters per minute (sccm). The recirculation cycle ends by condensing the xenon back into the cell.

The purpose of the recirculation is to remove impurities from the liquid without having to completely recover all the liquid xenon from the cell. The liquid remains calm while

the recirculation process occurs. This allows experiments to be performed during the recirculation process.

The liquid xenon is recovered from the cell after a set of experiments is completed. The liquid xenon can remain in the cell for several days by continuously filling the liquid nitrogen trap every hour and temperature regulation through the cell heater. In the case that the liquid nitrogen supply runs out, it takes about 3 hours for the temperature of the cell to go from 167 K to 178 K at which temperature, the pressure of the cell is 2 atmospheres. Before this happens, the liquid xenon is recovered as a preventive measure to avoid damage to the seals of the windows.

A diagram showing the path of xenon in the recovery process is shown in Figure 3.6. The liquid xenon recovery process is done by cryopumping the xenon from the copper cell into the xenon bottle. The process starts by raising the temperature of the cell to about 175 K. A liquid nitrogen bath is placed below the xenon recovery bottle, and the liquid nitrogen level is not above the mid-point of the xenon bottle. The top of the bottle is wrapped with heater tape, and heat is applied while the xenon is cryopumped to prevent freezing in the valve of the bottle. Once the xenon recovery bottle is cooled, its valve is opened and xenon gas is recovered from the bottom of the cell through the recirculation pipe.

As the xenon is evaporated from copper cell, the latent heat released by the liquid xenon causes the temperature of the copper cell and the recirculation pipe to decrease. If the temperature of the cell or the recirculation pipe gets down to 165 K, close to the freezing point of xenon at 1 atm, the recovery process is momentarily interrupted to prevent xenon ice formation. The power heater on both the pipe and copper cell is increased and the recovery process is resumed when the temperature of the cell goes up to at least 170 K. The recovery continues until the pressure inside the cell goes below 50 Torr. The residual xenon gas is released to the outer vacuum chamber by slowly opening a valve that isolates the inside of the copper cell from the outer vacuum chamber, and then it flows out of the chamber through the turbo pump.

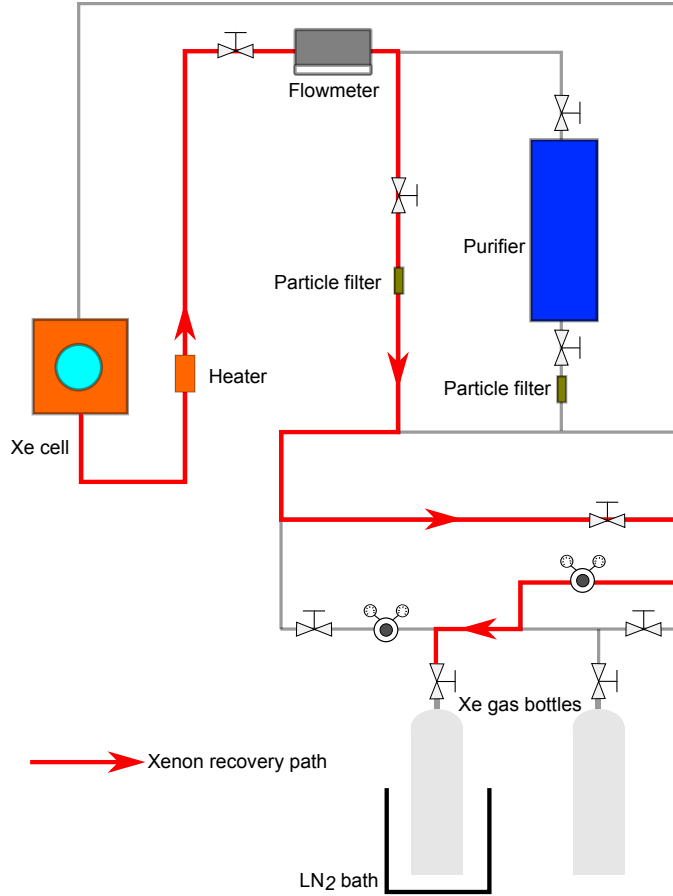


**Figure 3.6:** Simplified diagram of the path for xenon recovery.

## 3.2 CSU Purity Monitor

The electrode setup of the purity monitor is the same one used for the fluorescence experiments. A diagram of the electrode setup is shown in Figure 3.7.

The electrodes are labeled from top to bottom as follows: Target (T), Accelerator (A), Grid 2 (G2), Grid 1 (G1), Collector (C). The Target plate holds a barium metal tip used to create  $\text{Ba}^+$ ; this plate is not used for the purity measurements. The Accelerator, Grid 1, and Grid 2 are stainless steel plates with a diameter of 28.8 mm and thickness of 0.635 mm, these plates have an 11 mm diameter hole at the center. Mesh wires are soldered onto the plates and cover each hole. The purpose of the mesh wires is to ensure uniform electric field between the plates and at the same time allow electrons and ions to go through the plates. The

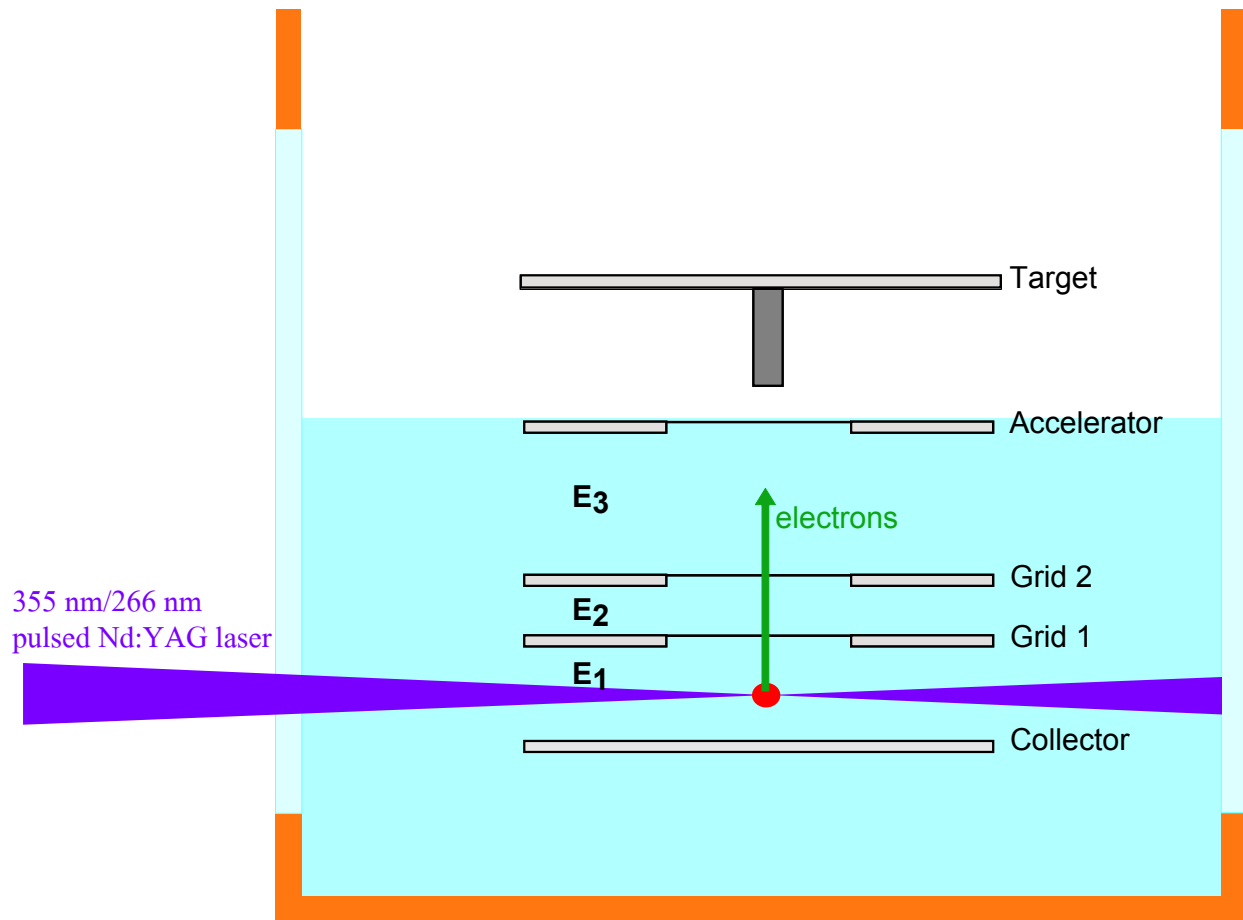


**Figure 3.7:** Diagram of the purity monitor. Electric fields  $E_1$ ,  $E_2$ , and  $E_3$  are applied in between the plates.

Collector plate at the bottom is the same as the other electrodes, except that it has no hole and wire mesh. The electrode plates are electrically isolated from each other with quartz tubes. The plate assembly is held in place inside the cell by an aluminum rod attached to a conflat flange blank. High voltage bias can be applied to each of the electrode plates through the preamplifier boxes. The quartz tubes are cut to the desired length with a diamond saw. Inside the cell, high vacuum coaxial cables are soldered onto each of the plates, and the cables are connected to vacuum feedthroughs. Each of the electrodes is connected to a preamplifier box model eV-550 by Endicott Interconnect Technologies, Inc. Each box has a low noise, charge sensitive preamplifier board model eV-5092, with a sensitivity of 0.2 mV/fC.

As in the ICARUS purity monitor discussed in section 2.5, the electron transmission in liquid xenon is measured to determine the concentration of impurities. There are three

main differences in the CSU purity monitor. First, electrons are created via multiphoton ionization of the liquid xenon instead of via photoelectric effect. Second, the CSU purity monitor is optically accessible for the fluorescence experiments. This has the advantage that the UV light for photoionization can be brought into the purity monitor without the use of an optical fiber. Third, the drift region is shorter, because the liquid xenon volume is smaller.

The ionization rate  $W$  of the  $n$ -photon process is proportional to the  $n$ th power of the laser intensity  $I$ , where  $n$  is the minimum number of photons needed to ionize the ion.

$$W \propto I^n \tag{3.1}$$

Our research group measured the  $n$  value of the multiphoton ionization process for different wavelengths. We found that for 221 nm and 266 nm wavelengths,  $n=2$ ; thus, two photons are needed to ionize the liquid xenon, for 280 nm and 355 nm a value of  $n=3$  was measured [20]. The UV light was focused with a 20 cm UV lens. The wavelengths used to create electrons in the purity monitor were 266 nm and 355 nm.

The electrons created by multiphoton ionization between the Collector and the Grid 1 plates drift to the Accelerator plate. As they pass through the liquid xenon, some of them become attached to electronegative impurities in the liquid. The current pulse coming out of each plate is measured with the preamplifiers. Typical preamplifier signals are shown in Figure 3.8. Initially, when the electrons are in the region between Collector and Grid 1, the Collector plate has a positive induced output current due to charge going away from the Collector and Grid 1 has a negative induced current due to charge going toward Grid 1. The preamplifiers connected to the other plates do not have induced current during this period, because they are shielded by Grid 1; then, the electrons drift through the region between Grid 1 and Grid 2 inducing signals on both plates, and then through the region between Grid 2 and Accelerator, until they finally arrive to the Accelerator plate. The integrated currents from each plate deduced from the preamplifier signals are used to calculate the percentage

of electrons that survive in the liquid xenon as they travel through the drift region. The liquid xenon purity is calculated from the transmission using the drift time.

### 3.2.1 Electron charge detection

The equivalent circuit of the preamplifier is shown in Figure 3.9. The preamplifier does not measure current directly, but rather puts a voltage proportional to the integrated current that decays with a time constant  $R_1C$ . The  $R_1C$  time constant for each amplifier is calibrated by fitting the decay part of a signal produced by a square wave current input. Measurements for each preamplifier while connected to the plate of interest are shown in Figure 3.10.

In order to understand better the drift of the electrons, the output voltage of the preamplifiers,  $V_{out}$ , is converted to a current signal. The following equations are obtained by applying Kirchhoff's rule to the circuit diagram of Figure 3.9.

$$I(t) = I_1(t) + I_2(t) \quad (3.2)$$

$$V_{out}(t) = MV_1(t) \quad (3.3)$$

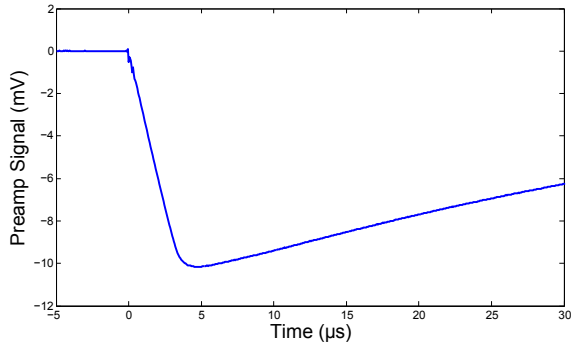
$$V_1(t) = -\frac{q_2}{C} = -I_1(t)R_1 \quad (3.4)$$

After solving these equations, the current  $I(t)$  in terms of the output voltage  $V_{out}(t)$  is given as

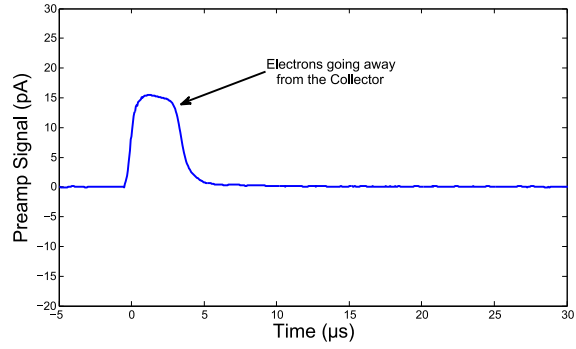
$$I(t) = -\frac{1}{R_1M} \left( V_{out} + R_1C \frac{dV_{out}}{dt} \right) \quad (3.5)$$

The gain factor  $R_1M$  for each preamplifier is determined by calibrating the preamplifier with a square wave signal through a 1 pF capacitor. A square input signal and its reconstructed signal is shown in Figure 3.11. A circuit diagram in calibration mode is shown in Figure 3.12. The multiplication factor that gives the best fit is  $R_1M=9.0 \times 10^6 \Omega$ .

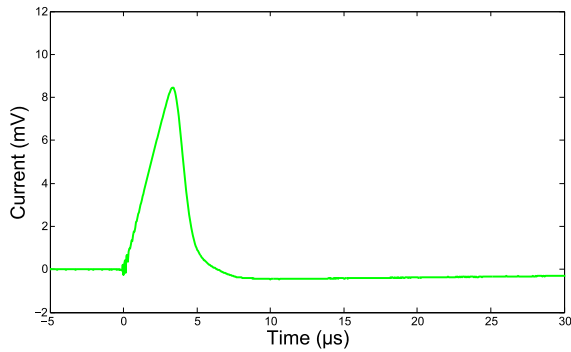
The preamp signals are recorded and averaged in a digital oscilloscope triggered by a photodiode that responds to scattered light from the pulsed laser. A LabView program stops the oscilloscope and transfers the data to a PC.



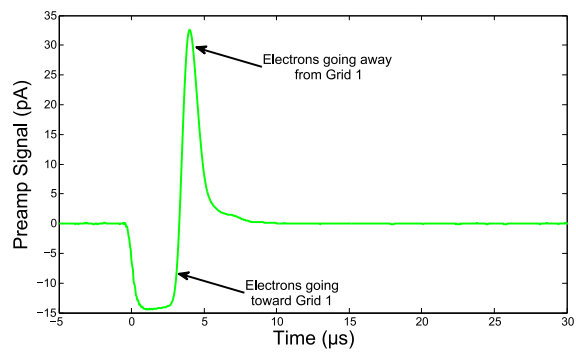
(a) Voltage signal from preamp attached to C



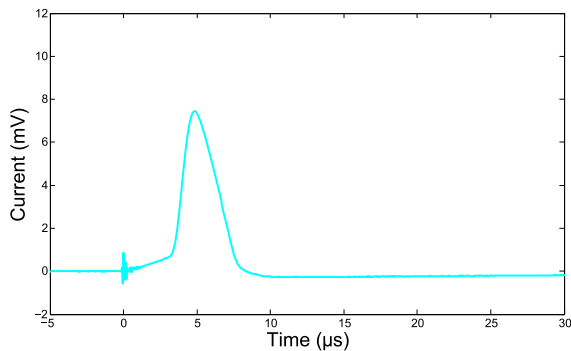
(b) Induced current signal on Collector plate



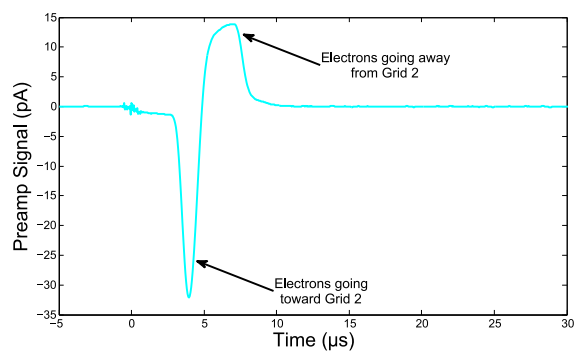
(c) Voltage signal from preamp attached to Grid 1



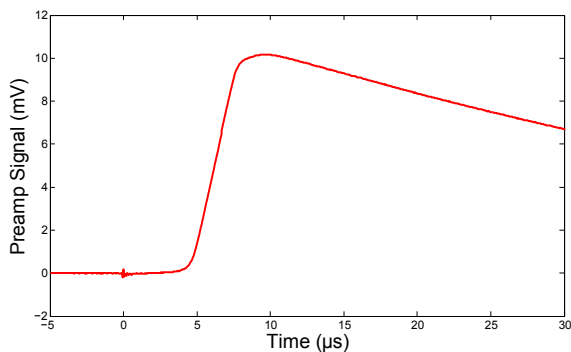
(d) Induced current signal on Grid 1 plate



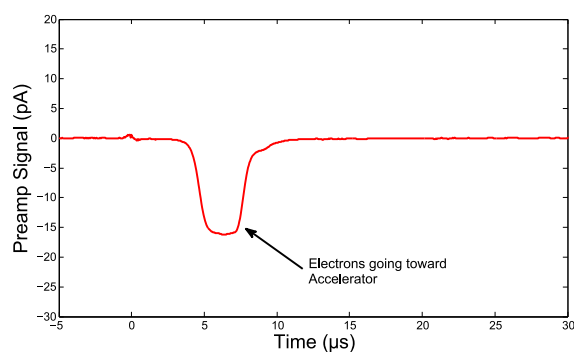
(e) Voltage signal from preamp attached to Grid 2



(f) Induced current signal on Grid 2 plate



(g) Voltage signal from preamp attached to A



(h) Induced current signal on Accelerator plate

**Figure 3.8:** Typical preamplifier and current signals of purity measurements

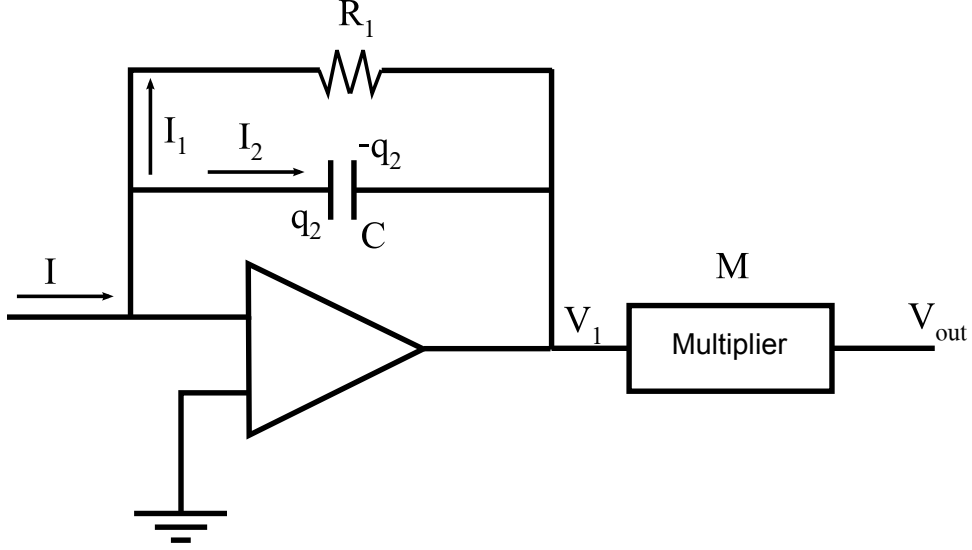


Figure 3.9: Equivalent circuit diagram of the preamplifier.

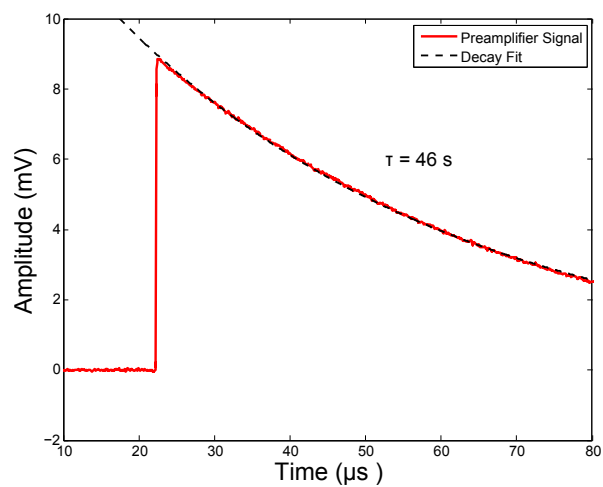
### 3.2.2 Detection of $\text{Ba}^+$ ion current

The same electrode system used for the purity monitor is also used to draw the barium ions, created in the ablation process, from the metal tip to the Grid 1 plate. A Keithley 610C electrometer connected to G1 is used to measure the ion current. Since the electrometer has a long time constant of hundreds of milliseconds, the current must be determined by a correction procedure using the output voltage signal of the electrometer and its derivative. The equivalent circuit of the electrometer is similar to that for the preamplifier shown in Figure 3.9, except that the time constant is much longer.

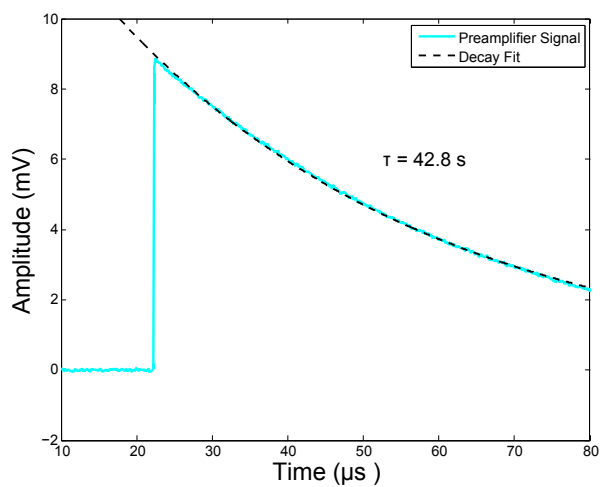
A circuit diagram in calibration mode is shown in Figure 3.13. The value of the resistance  $R_1$  in equation (3.5) depends on the settings of the electrometer. For the mobility experiments and fluorescence experiments of  $\text{Ba}^+$  in xenon gas the electrometer was operated at a scale of  $0.1 \times 10^{-9}$  A; for this setting,  $R_1 = 1 \times 10^9 \Omega$ . The multiplication factor  $M$  and the effective capacitance  $C$  are calculated by calibrating the electrometer with a square wave signal through a large resistor  $R = 2.2 \times 10^6 \Omega$ .

The following equation is obtained with the use of Kirchhoff's rule

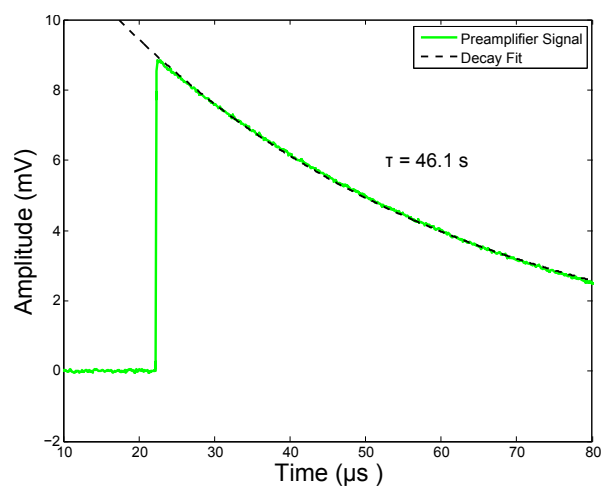
$$V_{test}(t) - I(t)R - I_1(t)R_1 = 0 \quad (3.6)$$



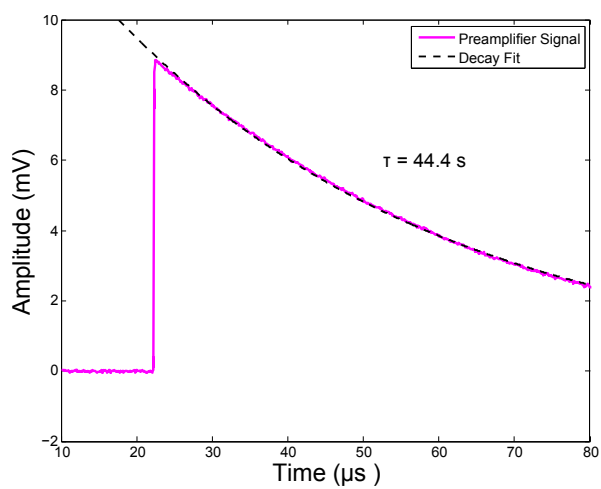
(a) Preamplifier connected to Collector plate



(b) Preamplifier connected to Grid 1 plate



(c) Preamplifier connected to Grid 2 plate



(d) Preamplifier connected to Accelerator plate

**Figure 3.10:** Fits of decay times from preamplifier signals

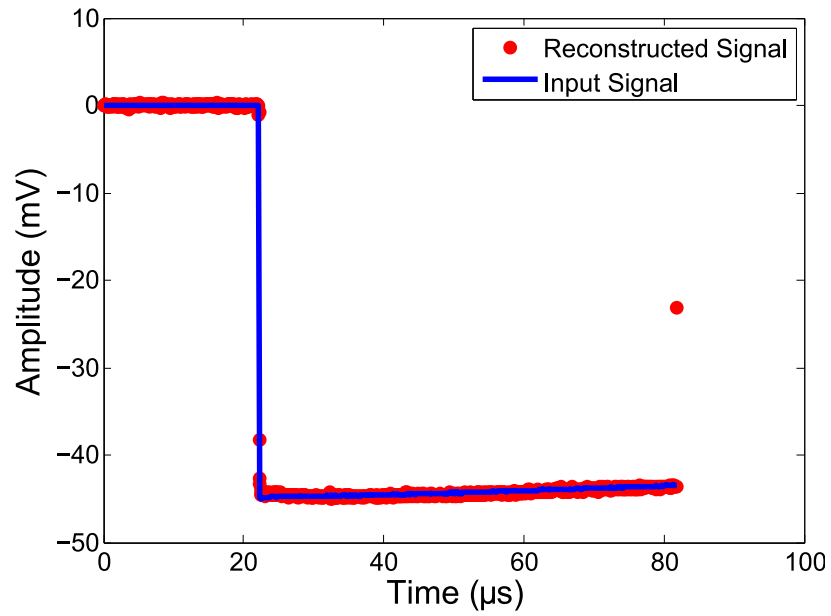


**Figure 3.11:** Reconstructed electrometer input signal and square wave input signal.

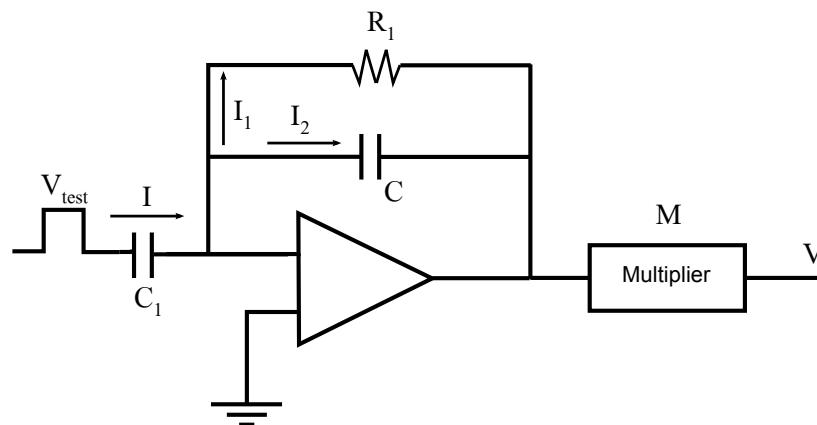


**Figure 3.12:** Circuit diagram of preamplifier in calibration mode.

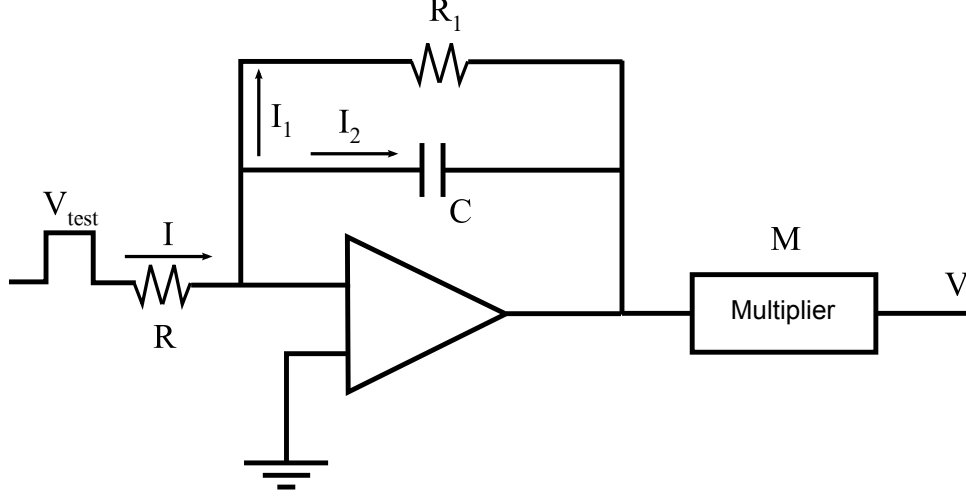


**Figure 3.13:** Equivalent circuit diagram of the electrometer.

Substituting Equations 3.5 and 3.4 in Equation 3.6,  $V_{test}$  becomes

$$V_{test}(t) = -\frac{R + R_1}{R_1 M} \left( V_{out}(t) + \tau_{eff} \frac{dV_{out}(t)}{dt} \right) \quad (3.7)$$

where  $\tau_{eff} = (RR_1)C/(R + R_1)$  is the effective time constant. The output signal  $V_{out}$  is recorded from an oscilloscope as well as the input test pulse  $V_{test}$ . The output voltage is used to reconstruct the initial input square wave pulse using Equation 3.7. Figure 3.14 shows a square wave input signal and a reconstructed signal. The parameters that best fit the input pulse are.  $M=-30$  and  $\tau_{eff}=0.92$  ms. The effective capacitance is then 420 pC. This gives a time constant  $R_1C=0.42$  s for the electrometer.

The voltage signal of the electrometer and the corrected current signal for a typical pulse of barium ions in xenon gas are shown in Figure 3.15. The asymmetry in the current signal indicates that there is some asymmetric spread of the ion cloud.

### 3.2.3 Determination of electron lifetime

A simplified formula the electron transmission is the ratio of the final charge detected at the Accelerator plate  $Q_A$  to the initial charge created between plates as measured at Collector,  $Q_C$ . A model of the induced current on the Collector and the Accelerator appropriate

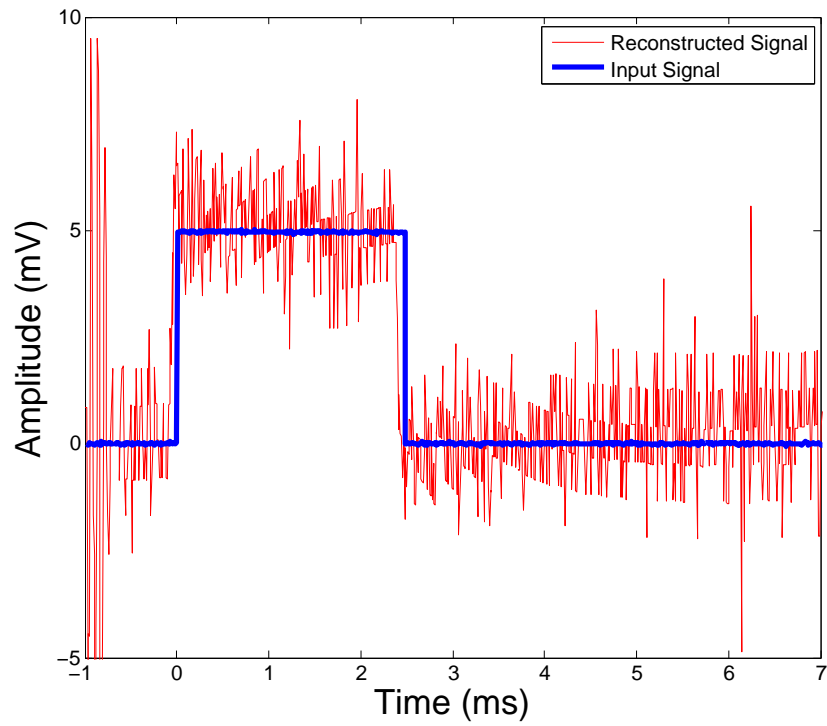


**Figure 3.14:** Reconstructed input signal compared to an actual signal.

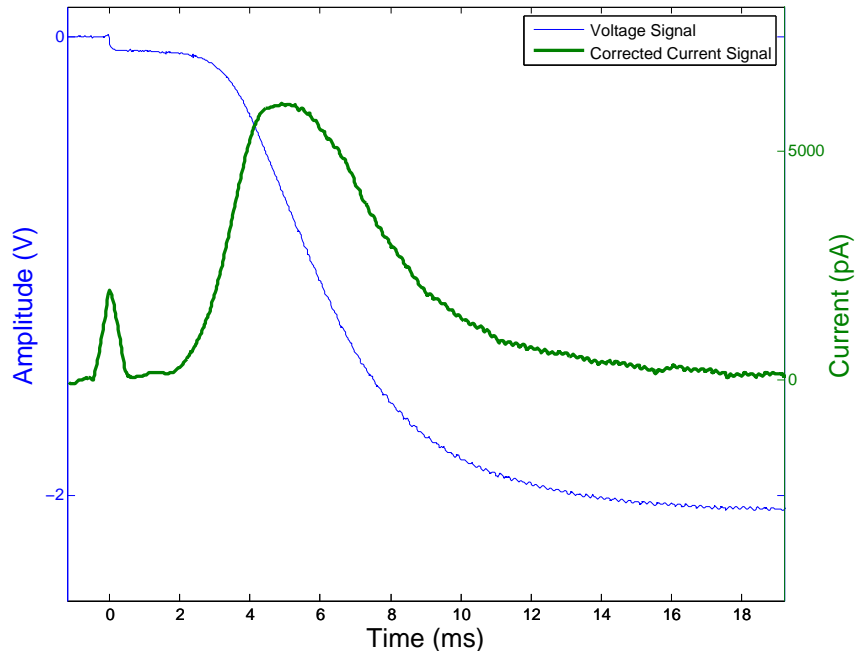


**Figure 3.15:** Plot of voltage signal from the electrometer and reconstructed current signal on Grid 1 from a typical pulse of  $\text{Ba}^+$  ions in xenon gas.

for a charge cloud with negligible physical size is illustrated in Figure 3.16. The drift time  $T_1$  is the time required by the electrons to drift from the location where they are created to Grid 1,  $T_2$  is the drift time between Grid 1 and Grid 2, and  $T_3$  is the time to drift from the Grid 2 to the Accelerator. The firing of the laser pulse is designated as  $t = 0$ . The purpose of Grid 1 is to shield the Collector from drifting electrons so that no current signal is induced after the electrons are drifting through Grid 1. The purpose of Grid 2 is to shield the Accelerator from the drifting electrons so that a current signal is induced only after the electrons have crossed Grid 2. The current as a function of time  $i(t)$  measured at

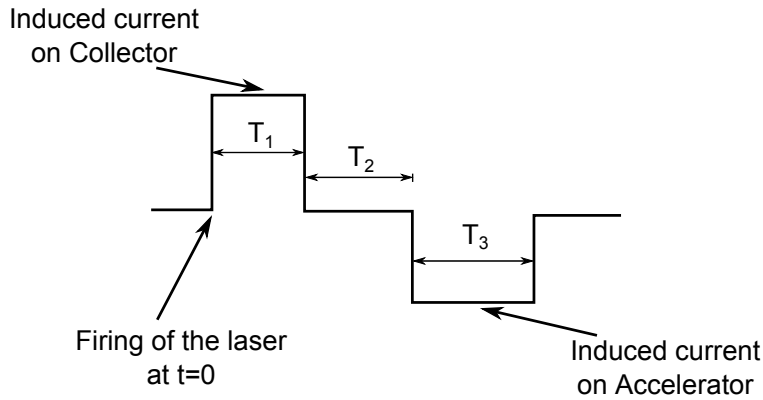


**Figure 3.16:** Simplified diagram of the induced current on Collector and Accelerator indicating the drift times.

the Collector and the Accelerator is determined by the speed of the electrons  $v_d$  and the geometry according to Ramo's Theorem [39]. Including electron loss due to attachment to electronegative impurities the induced current at time  $t$  in a given region  $i$  is

$$I_i(t) = \frac{Q_0}{T_i} e^{-t/\tau_e} \quad (3.8)$$

where  $Q_0$  is the initial charge,  $T_i$  is the drift time in region  $i$ , and  $\tau_e$  is the electron lifetime. Following a similar procedure for the determination of the electron transmission in liquid argon for the ICARUS experiment by Bettini et. al. [31], the total charge at the Collector,  $Q_C$ , is found by integrating the Collector current  $I_C(t)$  during the time that the electrons

travel from the location where they are initially created to Grid 1:

$$Q_C = \int_0^{T_1} \frac{Q_0}{T_1} e^{-t/\tau_e} dt = \frac{Q_0 \tau_e}{T_1} (1 - e^{-T_1/\tau_e}) \quad (3.9)$$

The total charge at the Accelerator is

$$Q_A = \int_{T_1+T_2}^{T_1+T_2+T_3} \frac{Q_0}{T_3} e^{-t/\tau_e} dt = \frac{Q_0 \tau_e}{T_3} (e^{-\frac{T_1+T_2}{\tau_e}} - e^{-\frac{T_1+T_2+T_3}{\tau_e}}) \quad (3.10)$$

The ratio  $R$  of  $Q_A$  to  $Q_C$ , after some algebraic manipulation, becomes

$$R = \frac{Q_A}{Q_C} = \left[ \frac{T_1 \sinh(T_3/2\tau_e)}{T_3 \sinh(T_1/2\tau_e)} \right] \exp \left\{ -\frac{T_2 + \frac{T_1+T_3}{2}}{\tau_e} \right\} \quad (3.11)$$

If  $T_1 \ll \tau_e$  and  $T_3 \ll \tau_e$ , then the term in square brackets of equation (3.11) is approximately 1, and the charge ratio is simply

$$R = e^{-T_d/\tau_e} \quad (3.12)$$

where  $T_d = T_2 + \frac{1}{2}(T_1 + T_3)$ . Thus, the electron lifetime can be found by measuring the ratio of the charge collected at the Accelerator to the charge at the Collector, and the drift times  $T_C$ ,  $T_D$  and  $T_A$ . The concentration of impurities is related to the electron lifetime by equation (2.27).

### 3.2.4 Electron transmission

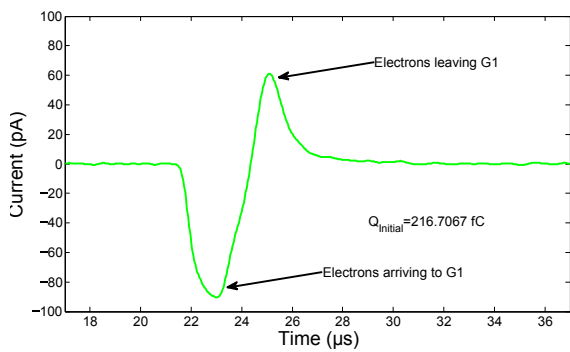
Using the ratio  $\frac{Q_A}{Q_C}$  to measure the electron transmission through liquid xenon, as discussed above, is valid if all electrons created in the region between Collector and Grid 1, except for the electrons lost to impurities, arrive at the Accelerator plate. Another requirement is that electrons are only created between Collector and Grid 1.

When the electron cloud created is wider than the hole in the Grid 1 plate, some of the electrons initially created would be collected by Grid 1 rather than passing through the hole. In this case, the amount of charge leaving Grid 1 would be less than the amount of charge

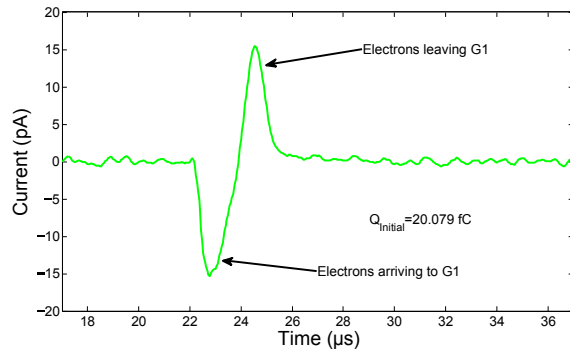
arriving to it. The current induced on Grid 1 when a relatively large number of electrons are created is shown in Figure 3.17a. Due to Coulomb repulsion there is a growth in size of the electron cloud until it is wider than the Grid 1 hole. One can see that the integral of the negative induced current signal due to electrons going towards Grid 1 is greater in magnitude than the integral of the positive current due to electrons leaving Grid 1. The difference should be the charge collected by Grid 1. When the electron charge is small (Figure 3.17b), the cloud of electrons is smaller and most of the electrons go through Grid 1. Therefore, the negative and positive current pulses are almost equal. The induced current signal on Grid 1 when the laser is focused 5.5 mm away from the center is shown in Figure 3.17c. The integral of the negative current signal due to electrons arriving to Grid 1 is greater in magnitude than the positive integral from electrons leaving the Grid 1, because some electrons are collected by Grid 1.

When the current from Collector and Grid 1 are added, the current from electrons leaving Collector approximately cancels the current from the electrons arriving during period  $T_1$  to Grid 1, since the charge will induce the same current on each plate but with opposite sign according to the Shockley-Ramo theorem [40]. Thus the sum of Collector plus Grid 1 current signals is just the induced current produced by electrons leaving Grid 1. In order to take into account the electrons lost to Grid 1, the transmission can be more accurately described by the ratio of  $Q_A$  to the charge leaving Grid 1,  $Q_{C+G1}$ . An example of the sum of Collector and Grid 1 current is shown in Figure 3.18. The charge  $Q_{C+G1}$  is calculated by integrating the red curve, the sum of Collector and Grid 1 currents. It can be seen that the signal of Collector plus Grid 1 is approximately zero while electrons go between the Collector and Grid 1 plate.

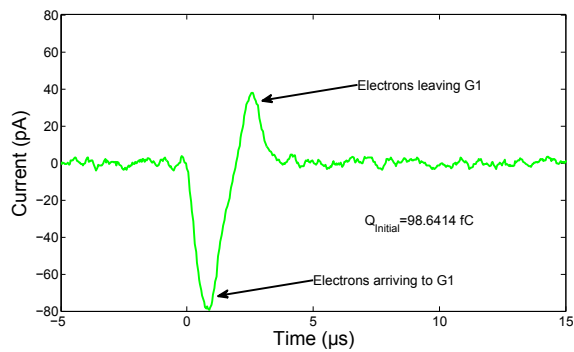
In order to obtain accurate purity measurements, all or most of the electrons must be created inside the volume of the purity monitor electrodes. If electrons are created outside the purity monitor volume, there may be additional charge arriving to the Accelerator plate without passing through Grid 1. This affects the purity measurements because the measured



(a) Induced current signal on Grid 1 due to a relatively large electron charge



(b) Induced current signal on Grid 1 due to a relatively small electron charge



(c) Induced current signal on Grid 1 when the ionization laser is focused approximately 5.5 mm away from the center of the purity monitor

**Figure 3.17:** Typical preamplifier and current signals of purity measurements

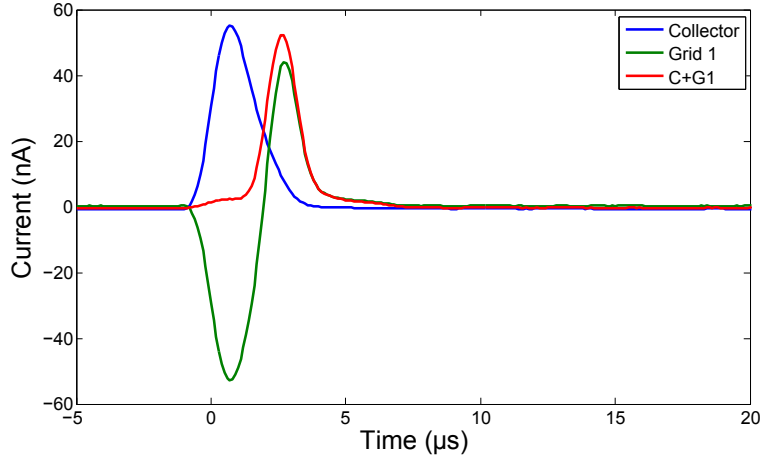


**Figure 3.18:** Example of sum of Collector plus Grid 1 current

electron transmission would be higher than the true transmission. The electrons moving outside the plates may also induce a current signal on the copper cell or the shielding of the coaxial cables that connect the plates to the preamplifiers. But, since neither the copper cell nor the shielding of the coaxial cables are connected to any preamplifier, that will not be detected.

In the parallel plate approximation, charge moving between plates will induce a current signal of the same magnitude, and opposite direction on each plate. If the charge is completely confined within the plates and the other conducting surfaces are far enough away, then the sum of the current signals of all four plates is expected to be zero. A non zero sum of the current signals can be interpreted as electrons arriving or leaving the system, composed of four plates, depending on the sign of the sum signal. An example of a negative sum is shown in Figure 3.19, indicating a net flux of electrons arriving to the system. An example of a sum signal approximately equal to zero is shown in Figure 3.20. In this case the sum is zero because most of the electrons are created inside the purity monitor.

There are two possible ways that electrons can be outside the plates. One way is that electrons are created along the path of the ionization laser outside the plate region. Due to the nonlinear ionization process most of the electrons are created in the focus, which is located in the center of the purity monitor. But there is still a small percentage of electrons

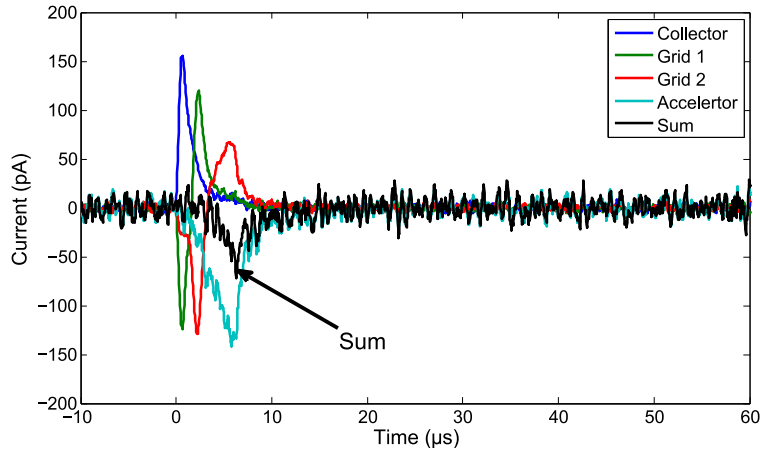


**Figure 3.19:** Example of current signal plates producing a negative sum.

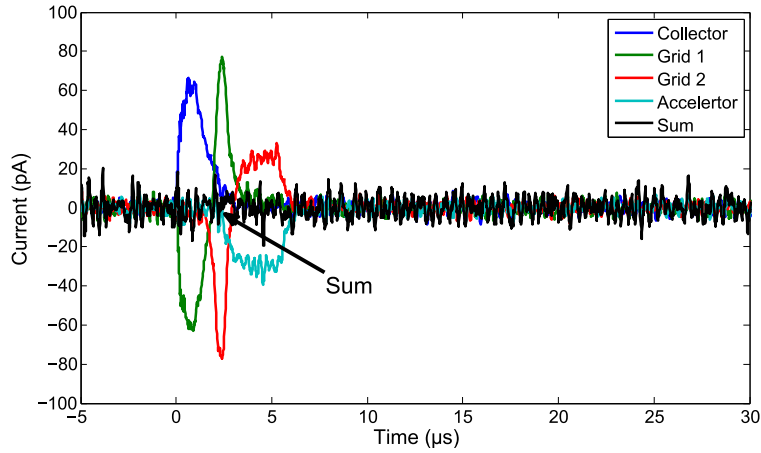


**Figure 3.20:** Example of current signal plates producing a sum approximately equal to zero.

created outside the plates. Another way is when electrons are initially created in the focus region, but they are repelled due to Coulomb repulsion and sent outside the plate region. This becomes significant as the laser energy increases, thus increasing the initial created electron charge.

To test the effect of electrons created outside the plates, measurements were taken when the laser beam used for ionization of liquid xenon was focused outside or close to the edge of the purity monitor. It can be seen in Figure 3.21 that having some charge created outside the purity monitor produces more negative signal in the Accelerator than positive signal in

the Collector plate. The net negative Sum signal indicates a net flux of electrons is entering the system from the outside.

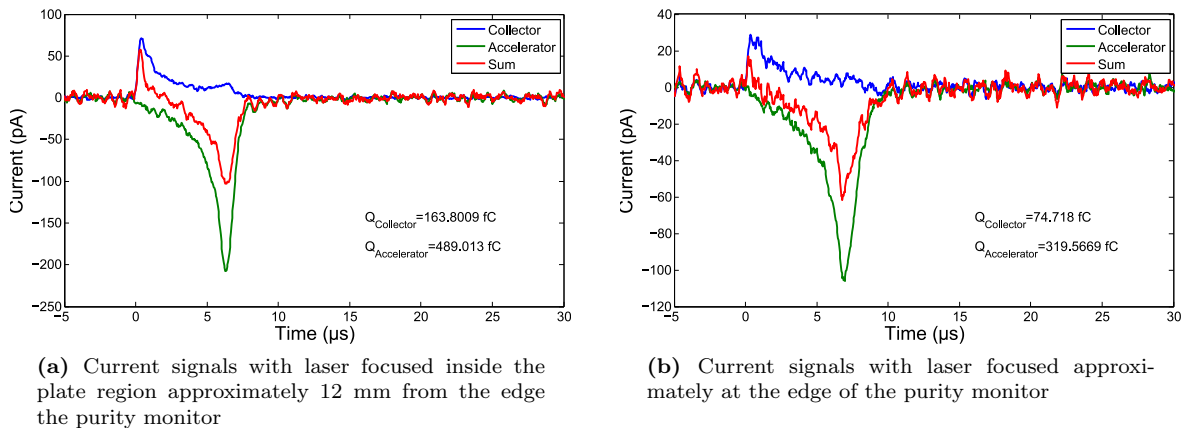


**Figure 3.21:** Signals with the UV ionization beam focused near the edge of the plate region.

In order to correct for electrons created outside the plate region, the extra signal may be subtracted from the Accelerator signal. This assumes that most of the outside electrons are collected by the accelerator, which has the most positive potential, and that they have similar attenuation along this path. By taking into account the corrections mentioned above, the electron transmission can be calculated by the ratio  $\frac{Q_{A-SUM}}{Q_{C+G1}}$ , where  $Q_{A-SUM}$  is the charge calculated by integrating the (Accelerator - Sum) signal.

By moving the focus of the laser beam horizontally, the position where most of the electrons are created can be changed. The different ratios proposed to measure the transmission will be affected as the focus is moved horizontally. The optimum correction implemented should make the transmission measurements independent of the position where the electron charge is created.

The electron transmission was measured as a function of the position of the focus by moving the focusing lens horizontally. Results of four separate measurement runs are shown in Figure 3.22. The ratio  $\frac{Q_A}{Q_C}$  has a maximum near the center of the purity monitor. Then the ratio decreases as the focus moves away from the center, because only the portion of the electron cloud that is below the hole of Grid 1 is transmitted. The spacing between the two

minima of transmission is approximately 1 cm, which is about the size of the hole of Grid 1, so this explanation makes sense. As the laser focus moves further out than the edge of the grid hole, the ratio  $\frac{Q_A}{Q_C}$  increases again because more electrons start to be created outside the purity monitor which causes additional signal on the Accelerator.

The ratio  $\frac{Q_A}{Q_{C+G1}}$  corrects for electrons lost to Grid 1. It can be seen that this ratio does not have dips as the focus moves away from the center of the purity monitor. But the ratio increases to values greater than 1 as the focus gets closer to the edge of the purity monitor, since it does not take into account the electrons created outside of it.

The ratio  $\frac{Q_{A-SUM}}{Q_{C+G1}}$  also takes into account the electrons outside the purity monitor by including the Sum signal. More detailed plots with error bars are shown in Figure 3.23. The ratio is relatively flat throughout the whole range, but still increases to values higher than 1 when the focus is close to the edge of the purity monitor. The ratio increases near the edge of the purity monitor suggest that the correction using the formulas is not complete when the focus is far from the center. The corrections are not as accurate when the sum signal is large, so it is best to keep the sum signal as small as possible by creating only a small amount of charge in the center of the purity monitor.

The total distance from the lens to the center of purity monitor is estimated by external measurements to be 23.5 cm. Figure 3.24 is a schematic representation of the lens, window on vacuum chamber and window of the copper cell relative to the center of the purity monitor. From the plots in Figure 3.22, the point symmetry of the electron transmission  $\frac{Q_A}{Q_C}$ , where the focus should be in the center of the purity monitor, is located between 23.0 cm and 23.5 cm in the different experiments in agreement with the external focus measurements. The laser beam focus could change from time to time as the divergence of the laser can vary somewhat with flashlamp energy.

From Figures 3.22 and 3.23, the electron transmission in the center of the purity monitor is  $\sim 100\%$  in all four runs. The number of electrons created via nonresonant multiphoton ionization at a position  $z$  of the beam, is proportional to function  $S_n(z)$ , which is a measure

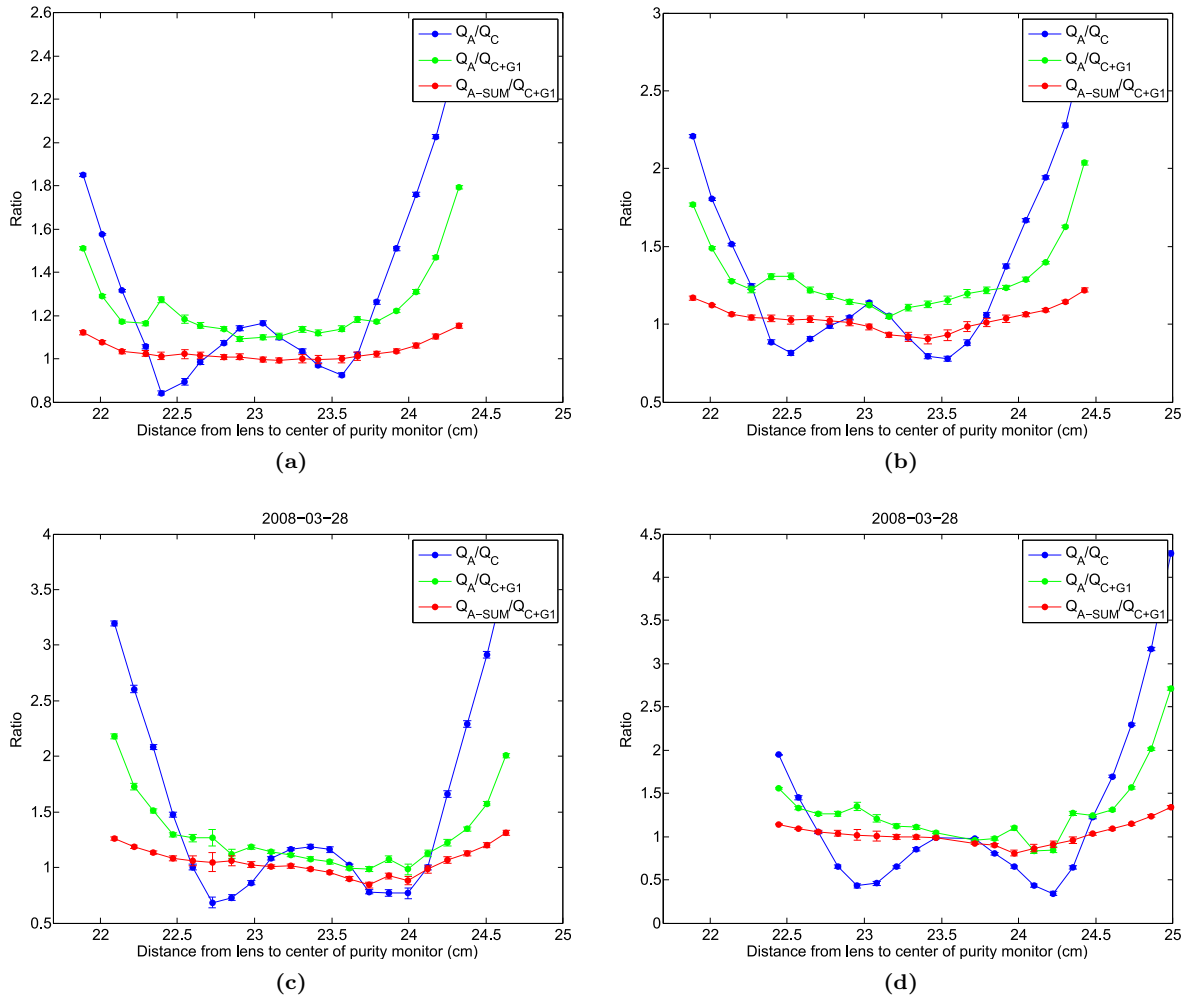
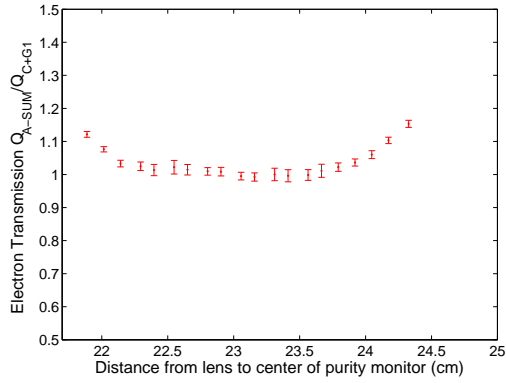
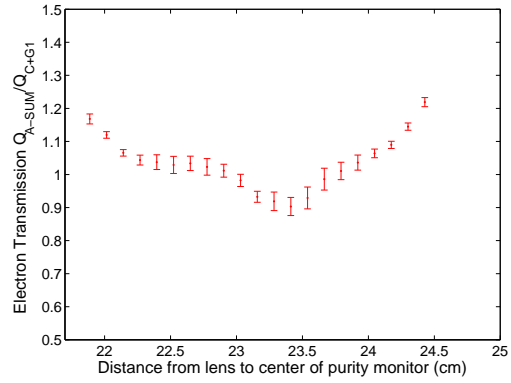


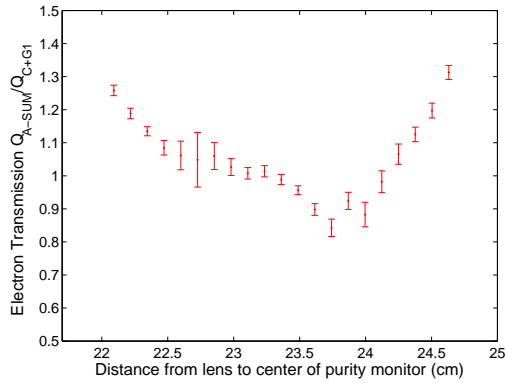
**Figure 3.22:** Plots of ratios of charge as a function of the focus position from four separate runs. The ionization beam was focused with a nominal 22 cm lens using a wavelength of 355 nm



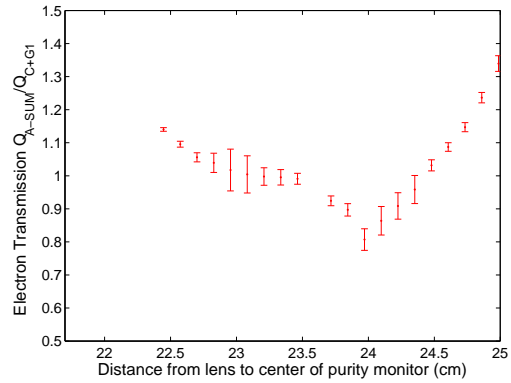
(a)



(b)



(c)



(d)

**Figure 3.23:** Plots of ratio of charge  $\frac{Q_{A-SUM}}{Q_{C+G}}$  vs focus position. This is the same data as in Figure 3.22 with the scale in the  $y$  axis expanded.

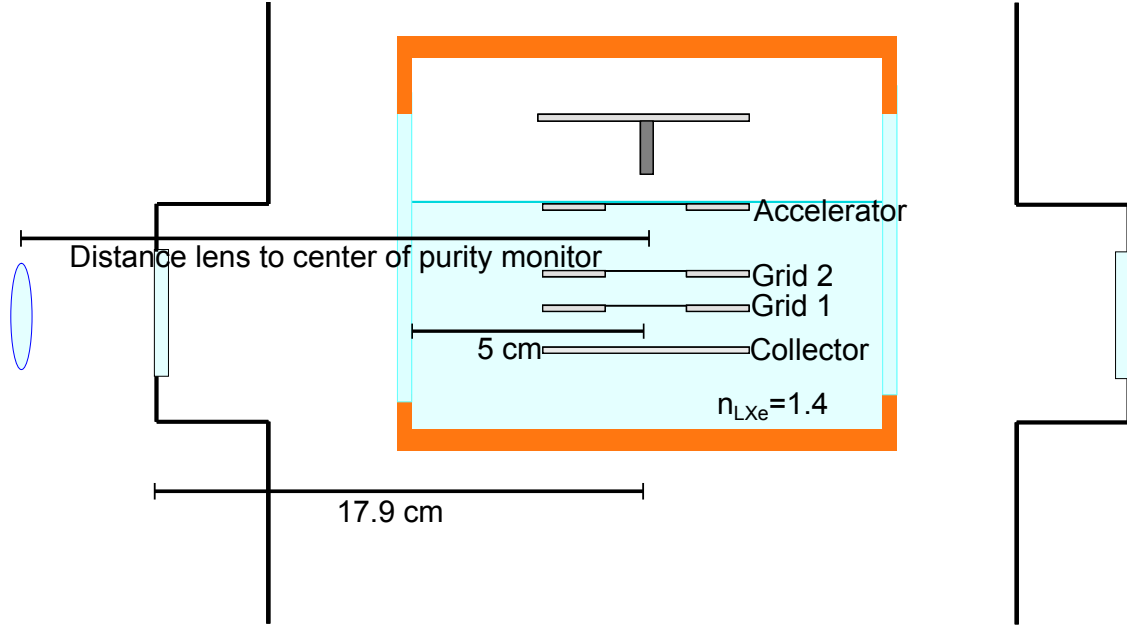


**Figure 3.24:** Position of lens relative to the center of the purity monitor.

of the relative number of electrons created per unit length in  $z$  and depends on the beam waist  $w(z)$  as follows:

$$S_n(z) = [\pi w^2(z)]^{1-n} \quad (3.13)$$

where  $n$  is the number of photons needed to ionize the liquid xenon,  $n=3$  for a wavelength of 355 nm. This was discussed in detail in Kendy Hall's thesis [20]. For  $n>1$ , most of the electrons will be created at positions where  $w(z)$  is small, i.e., near the focus. At positions farther away from the focus the beam waist will grow and therefore smaller number of electrons per length will be created outside the focus. Even though the number of electrons created away from the focus is small, they must be taken into account when measuring the transmission, since to measure small impurity concentrations, transmissions close to 100% need to be determined. As seen in Figure 3.23, the ratio  $\frac{Q_A - SUM}{Q_C + G1}$  does a reasonable job of this.

By increasing the laser energy, due to Coulomb repulsion of the initial charge, the number of electrons outside the purity monitor increases. This results in an apparent electron transmission  $\frac{Q_A}{Q_C}$  that depends on the initial charge created. At greater initial charge, the electron

cloud radius is larger, and the fraction of charge transmitted through Grid 1 should decrease. In Figure 3.25a this ratio is plotted against the Collector charge, which is the initial electron charge created. For large charge, the ratio  $\frac{Q_A}{Q_C}$  decreases dramatically, in agreement with expectations. The ratio  $\frac{Q_A}{Q_{C+G1}}$  takes into account charge lost to Grid 1 but does not correct for charge outside the plates. Figure 3.25b shows that the ratio  $\frac{Q_A}{Q_{C+G1}}$  is close to constant with initial charge, but goes up to values higher than 1 for large initial charge. The ratio  $\frac{Q_{A-SUM}}{Q_{C+G1}}$  includes corrections for electrons outside the purity monitor. In Figure 3.25c this ratio is plotted against the Collector charge. It is observed that the transmission is slightly overcorrected at large Collector charge.

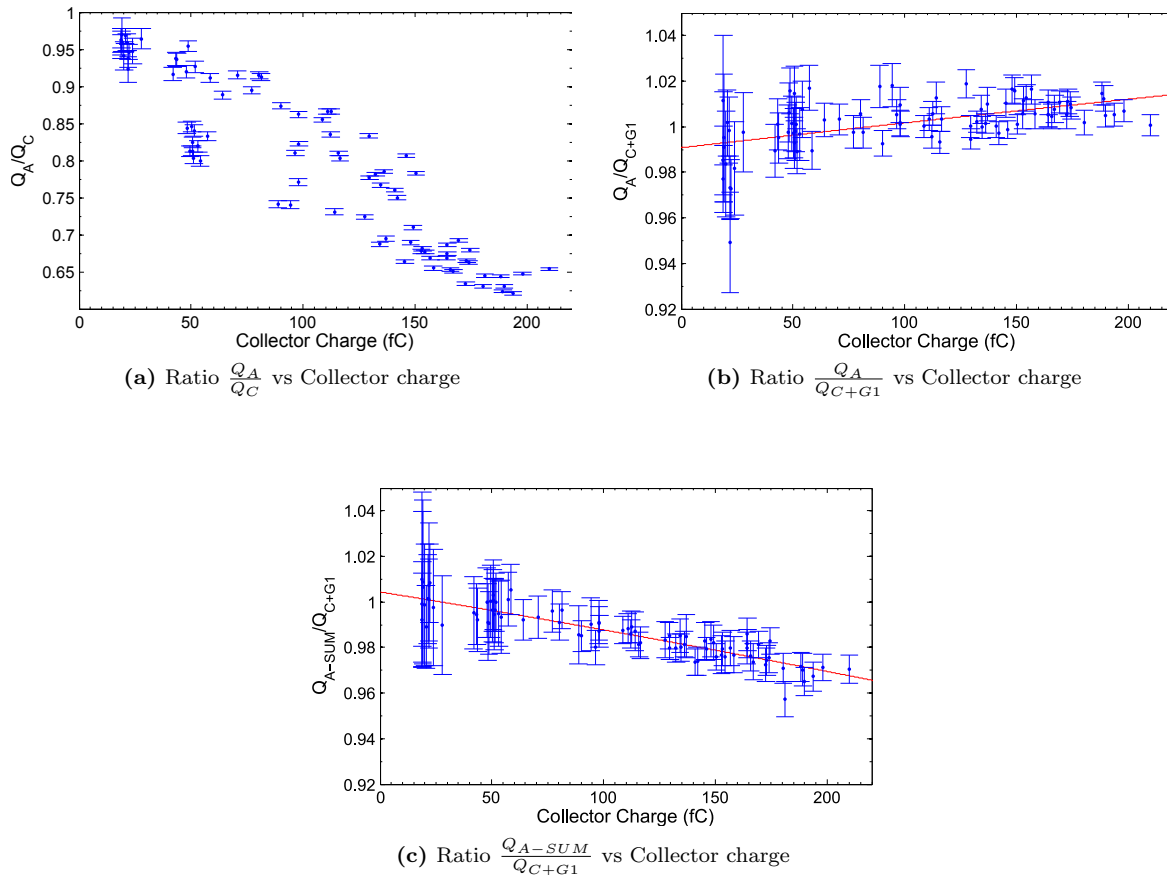


**Figure 3.25:** Plots of electron transmission ratios as a function of initial charge.

The plot of  $\frac{Q_{A-SUM}}{Q_{C+G1}}$  vs Collector charge in Figure 3.25c was fitted to a quadratic function of the form  $R = a + bx + cx^2$  using a weighted regression fit. The values of the parameters for

the fit of the transmission  $\frac{Q_{A-SUM}}{Q_{C+G1}}$  are  $a=1.004\pm 0.006$ ,  $b=(-1.58\pm 1.02)\times 10^{-4}$ , and  $c=(-7.98\pm 41)\times 10^{-8}$ . The intercept  $a$  gives the transmission at zero charge is  $1.004\pm 0.006$ , which is consistent with 100% transmission. Such a fit can be used to correct for systematic error due to large charge size. If the initial charge is less than 50 fC, the systematic error due to the charge is less than 1%.

In summary, the best way to minimize the systematic error in the electron transmission is to use the smallest possible amount of charge, to confine the electron creation to the center of the purity monitor using a tight focus and a nonlinear ionization process. The quantity used to measure the electron transmission in the purity studies in Chapter 4 is  $\frac{Q_{A-SUM}}{Q_{C+G1}}$  except where otherwise mentioned.

### 3.2.5 Transparency of grids

To prevent extra electron loss, the grids, especially Grid 2, must have essentially 100% charge transparency, i.e.,  $\sim 100\%$  of the electrons must be transmitted through the grids. High transparency to the electrons can be achieved by choosing an appropriate ratio of electric fields before and after the grid; the critical ratio of the electric fields depends on the geometry of the grid such as the diameter of the wires, and the distances between the wires but should be on the order of 3 [39]. The ratio of the electric fields needed to have close to 100 % transparency of the grids was experimentally determined by varying the ratio of the electric fields between the plates, and measuring the transmitted charge through the grid.

To measure the transparency of the Grid 2, the electron transmission was measured while the ratio  $E_3/E_2$  was varied while keeping  $E_1$  and  $E_2$  fixed, where  $E_3$  is the electric field between Grid 2 and Accelerator,  $E_2$  is the electric field between Grid 1 and Grid 2, and  $E_1$  is the field between Grid 1 and Collector as depicted in Figure 3.7. In these measurements, the focus of the UV beam was positioned between the Collector and Grid 1, at approximately the center of the purity monitor. The initial electron charge was nearly constant for each run, the variation in the initial charge was due to fluctuation in the laser power.

The different transmission ratios for four different charge values are plotted versus the ratio of electric field  $E_3/E_2$  in Figure 3.26 and 3.27. The transmission has a rapid rise and then is constant at about 1 for values  $E_3/E_2 > 2-3$ . Results of a fit of the form  $T(1 - \exp(-\frac{E_3/E_2}{b}))$  are given in the figures. The spacings between the plates for these experiments are listed in the Configuration A of Table 3.1

**Table 3.1:** Configuration of distances for purity monitor

Distance between plates	Configuration A	Configuration B
Grid 2 to Accelerator	8 mm	8 mm
Grid 1 to Grid 2	1 mm	1 mm
Collector to Grid 1	2 mm	4 mm

The voltages applied to the plates of the purity monitor were,  $V_C = 0V$ ,  $V_{G1} = 20V$ ,  $V_{G2} = 50V$ , and  $V_A$  was varied in Figure 3.26 and  $V_C = 0V$ ,  $V_{G1} = 10V$ ,  $V_{G2} = 22.5V$ , and  $V_A$  varied in Figure 3.27.

The measured transmission at high  $E_3/E_2$ , according to the ratio  $\frac{Q_{A-SUM}}{Q_{C+G1}}$  was  $T = 100\%$  to within  $2\sigma$  for the lower charges. This again confirms that measurements with high transmission can be made. The ratio of electric field  $\frac{E_3}{E_2}$  that gives a grid transmission greater than 99% must satisfy  $\frac{E_3}{E_2} > 4.6b$  where  $b$  is the fit parameter. For the lowest value of  $b$  in this data, the electron transmission through Grid 2 is greater than 99% if  $\frac{E_3}{E_2} > 2.26$  and for the highest value of  $b$   $\frac{E_3}{E_2} > 3.18$ . In the measurements of the electron lifetime the ratios of electric field used were  $\frac{E_3}{E_2} \geq 3$  and  $\frac{E_2}{E_1} \geq 3$ .

### 3.3 Ba<sup>+</sup> Ion Creation by Laser Ablation

For the mobility and spectroscopy experiments, Ba<sup>+</sup> ions are created by pulsed laser ablation of a barium metal tip. Absorption of intense laser light results in rapid heating of the material surface down to thickness on the order of 1  $\mu\text{m}$ , with the subsequent vaporization of surface atoms and molecules. If electrons released are hot and dense enough a plasma

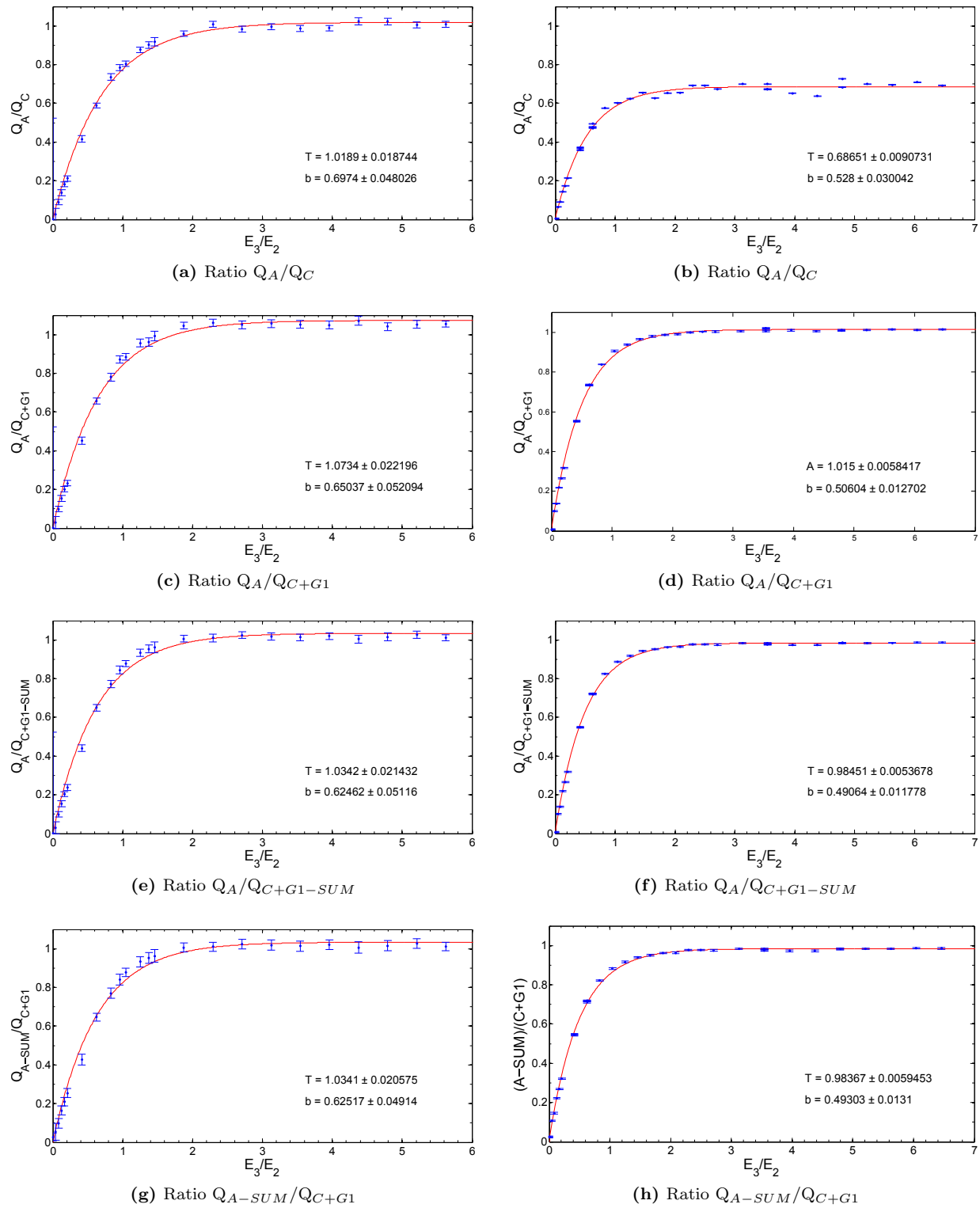


**Figure 3.26:** Transmission plots as a function of the ratio of electric fields  $E_3/E_2$ . The plots on the left have an average charge 18 fC, and the plots on the right have an average charge of 232 fC

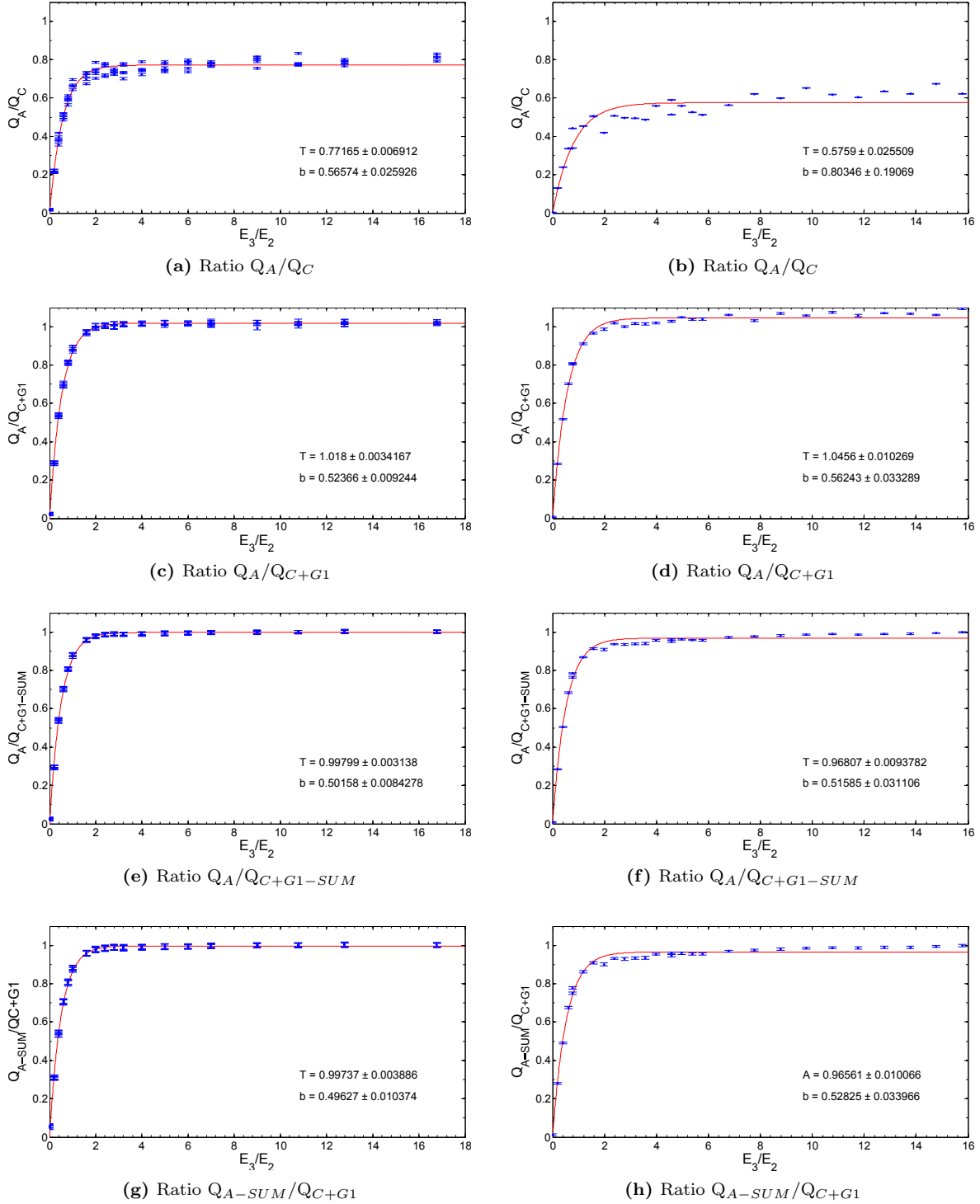


**Figure 3.27:** Transmission plots as a function of the ratio of electric fields  $E_3/E_2$ . The plots on the left have an average charge 50 fC, and the plots on the right have an average charge of 212 fC

forms resulting in enhanced creation of ionized surface species. The ablated material forms an expanding cloud of neutral atoms and molecules, electrons and ions.

The barium metal tip used as a target material for laser ablation is mounted in a slot made in the Target plate. Figure 3.28 is a picture of the electrode plates setup with the metal tip. The barium tip is cut from a pure barium rod using a stainless steel saw blade. Then the piece is molded by hammering it and given a rectangular shape using diagonal cutter pliers. The top of the barium tip is slightly thicker than the rest of the tip so that it can be mounted snugly in the slot of the Target plate. Once the barium tip is made to the desired shape, the oxide layer that forms quickly on the barium is removed with a file as much as possible. Then the tip is mounted on the Target plate. After this process is completed, the electrode plate system with the barium metal tip is loaded into the copper cell by inserting it from the top of the chamber. The copper cell is evacuated right after the electrodes and the barium are inside the cell, to prevent further oxidation of the barium metal.

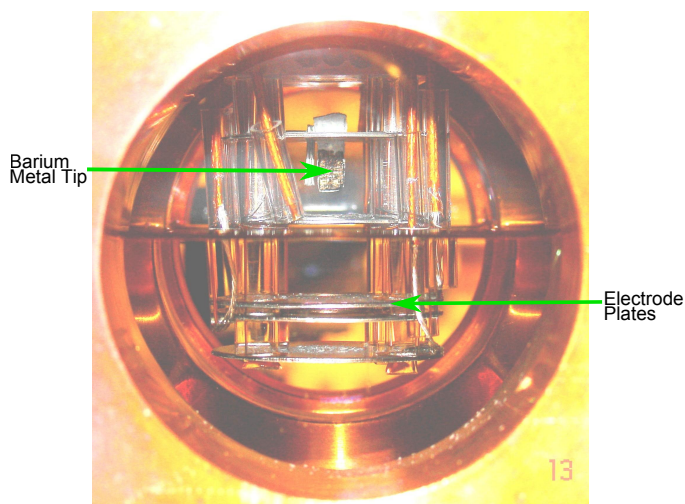


**Figure 3.28:** Picture of barium metal tip and electrode plates.

The laser used to ablate the barium metal is a Quanta-Ray Nd:YAG pulsed laser with a wavelength of 1064 nm and a pulse width of 10 ns. The ablation laser beam is focused with a 48 cm lens. When the laser is focused exactly at the barium metal tip, the intensity of the beam is high enough that it makes a hole through the barium metal after a few laser shots. To avoid this situation, the lens is positioned such that the focus is 5 cm beyond the

barium metal tip. This way the beam size at the barium metal is larger, thus reducing its intensity. Depending on the amount of ion charge produced, the typical pulse laser energy varies between 5 mJ and 15 mJ, and with  $w=0.05$  cm, the peak intensity is on the order of  $10^8$  W/cm<sup>2</sup>. The ablation produces a controlled Ba<sup>+</sup> charge pulse that depends on the laser pulse energy, as shown in Figure 3.29. The energy of the laser is varied by using a variable neutral density (ND) filter. The energy of the laser pulse is measured with a Coherent FieldMaxII-TOP laser power/energy meter with a Coherent J-25MB-LE energy sensor. It is seen that the ion charge can be continuously controlled in the range of 3 pC to 50 pC. Above a threshold of about 6 mJ, the charge increases almost linearly with ablation energy.

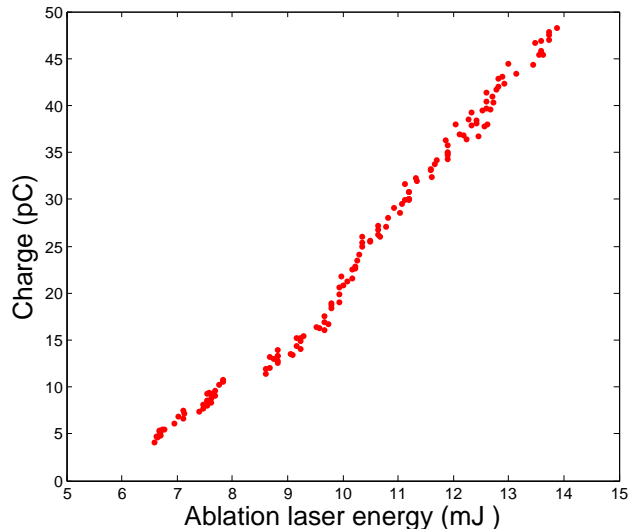


**Figure 3.29:** Barium ion charge vs ablation energy from the 1064 nm pulsed Nd:YAG laser.

### 3.4 Mobility of Ions in Gas

The mobility of Ba<sup>+</sup> ions in Xe and in Ar gas was determined at varying gas pressures by measuring the drift time of the Ba<sup>+</sup> ions from the barium metal tip, where the ions were created by laser ablation, to the Grid 1 plate. The ion mobility  $\mu$  given in Chapter 2 is

$$\mu = \frac{v}{E} \tag{3.14}$$

where  $E$  is the electric field and  $v$  the drift velocity.

In the experimental setup for the mobility experiments, the electric field is not constant along the drift path, so the transit time results from the ions passing through regions of different  $E$  values. The equipotential lines and the trajectory of the ions calculated by SIMION software package are shown in Figure 3.30. The green line is the drift path of the

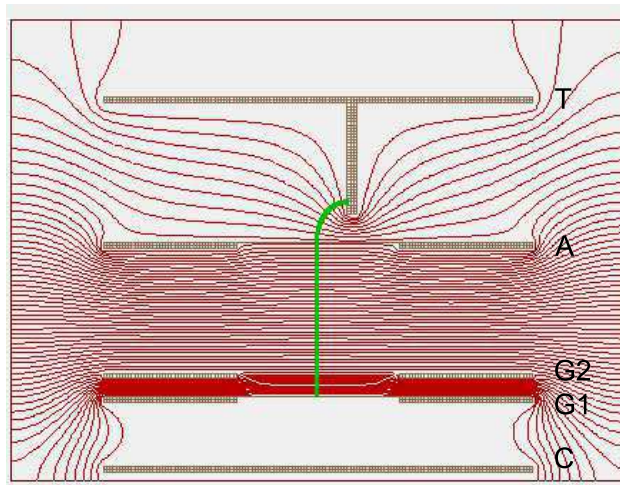


**Figure 3.30:** Cross section of the equipotential lines of the electrode configuration with a straight barium metal tip simulated by SIMION 8.0

ions, and the red lines are equipotential contours. It can be seen that the electric field is not uniform near the metal tip, which causes the trajectory of the ions to curve while they travel between the ablation target and the Accelerator plate. To take the nonuniformity of the electric field into account, the  $E$  field is calculated along the trajectory path of the ions. The mobility depends on the integral of  $1/E$  along the drift path of the ions according to [37]:

$$\mu = \frac{V \int \frac{ds}{E}}{V t_d} = \frac{d_{eff}^2}{V t_d} \quad (3.15)$$

where  $V$  is the applied voltage between the Target and Grid 1 plates and  $t_d$  is the drift time of the ions. The parameter  $d_{eff}^2$  is calculated by numerically integrating  $V/E$  along the drift path. It depends only on the geometry of the electrode system and the ratio of the voltages of the electrodes. The coordinates of the drift path and the electric field at each point along

the trajectory of the ions are obtained from the SIMION simulation. The drift path starts at the spot where the ablation laser hits the barium tip, and it ends at the G1 plate where the ion current is detected by the electrometer. The drift time,  $t_d$ , is defined as the time at which the peak of the current signal occurs on G1. The LabView program used to save the electrometer output signal automatically reconstructs the current  $I(t)$  and finds the peak time after smoothing the current signal. The charge is the integral of the current. The signal at  $t=0$ , possibly due to the photoelectric effect, is neglected. Some examples of current signals at different applied voltages on the target are shown in Figure 3.31. Applying a lower voltage causes the ions to travel slower and the total time of flight of the ions increases.

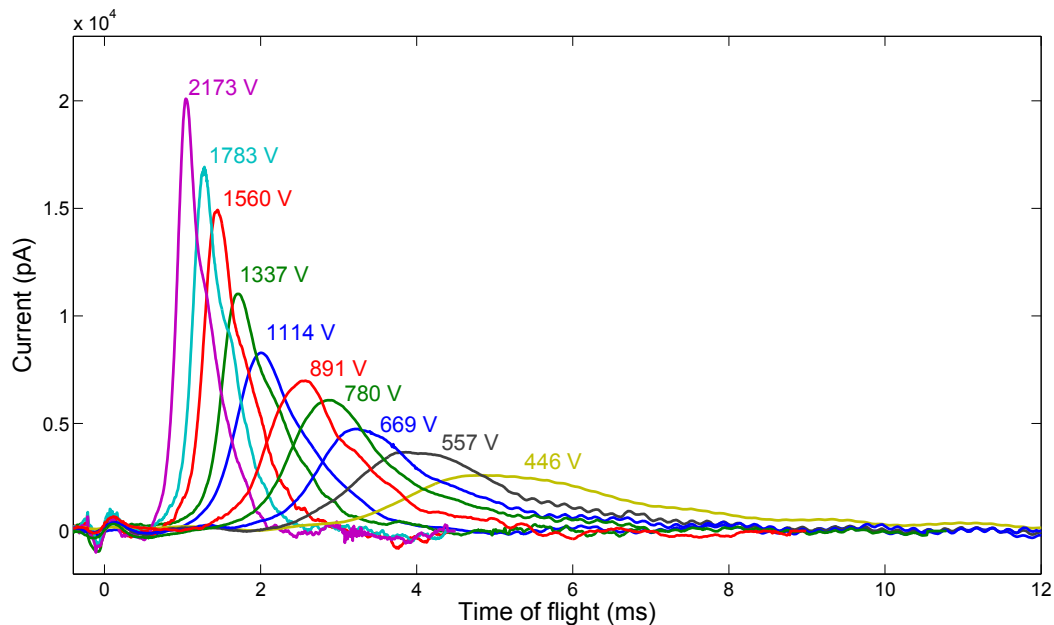
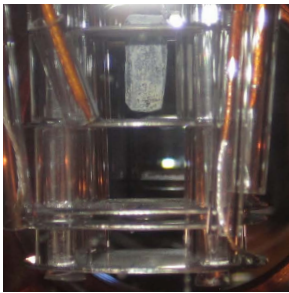


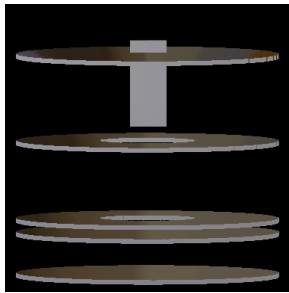
**Figure 3.31:** Current signals of barium ions in xenon gas at a pressure of 640 Torr and a temperature of 296 K. The applied voltage on the Target plate is denoted for each signal.

### 3.4.1 Calculation of $d_{eff}^2$

Pictures of the three different target configurations and their corresponding 3D models, which were done using SIMION 8.0, are shown in Figure 3.32. In one of the configurations, the metal tip was mounted vertically (3.32a-3.32d), in another configuration the metal tip



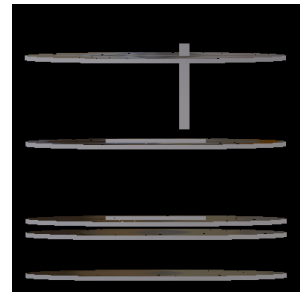
(a) Front view of straight metal tip configuration



(b) Front view of 3D model of straight metal tip configuration in SIMION



(c) Side view of straight metal tip configuration



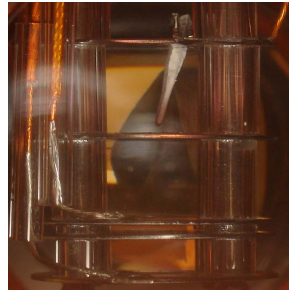
(d) Side view of 3D model of straight metal tip configuration in SIMION



(e) Front view of tilted metal tip configuration



(f) Front view of 3D model of tilted metal tip configuration in SIMION



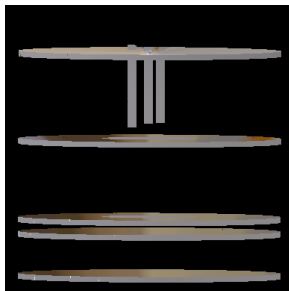
(g) Side view of tilted metal tip configuration



(h) Side view of 3D model of tilted metal tip configuration in SIMION



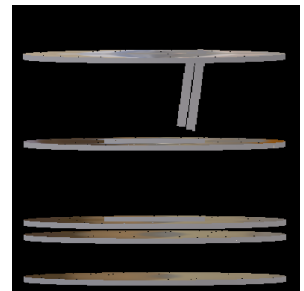
(i) Front view of BaAl getters configuration



(j) Front view of 3D model of BaAl getters configuration in SIMION



(k) Side view of BaAl getters configuration



(l) Side view of 3D model of BaAl getters configuration in SIMION

**Figure 3.32:** Electrode configuration with barium metal and BaAl getters

was tilted about 15 degrees (3.32e-3.32h), and in the third case three BaAl getters were spot welded to the Target plate (3.32i-3.32l).

The spacing between the plates for mobility measurements is listed in Table 3.2. The length of the metal tip varied every time a new piece was installed, but the distance between the Accelerator plate and the lower end of the metal tip was usually around 2 mm.

**Table 3.2:** Configuration of distances between plates for mobility experiments

Distance between plates	
Accelerator to Target	9 mm
Grid 2 to Accelerator	8 mm
Grid 1 to Grid 2	1 mm
Collector to Grid 1	4 mm

The configurations of some of the voltages used for the mobility experiments are listed in Table 3.3. The voltage on the Target, Accelerator and Grid 2 plate were varied proportionally to keep  $d_{eff}^2$  the same, the Collector plate was grounded to a 50  $\Omega$  resistor, and the Grid 1 plate was connected to the electrometer.

**Table 3.3:** Configuration of voltages applied to the electrode plates for mobility experiments

$V_{G1}$	$V_{G2}$	$V_A$	$V_T$
0 V	501 V	1839 V	2173 V
0 V	411 V	1509 V	1783 V
0 V	360 V	1320 V	1560 V
0 V	309 V	1131 V	1337 V
0 V	257 V	943 V	1114 V
0 V	206 V	754 V	891 V
0 V	180 V	660 V	780 V
0 V	154 V	566 V	669 V
0 V	129 V	471 V	557 V
0 V	103 V	377 V	446 V

As in the case of the electron transmission through the grids, it is important to have an appropriate ratio of the electric fields between the grids to ensure the maximum transmission of barium ions. The adequate ratio is found experimentally by varying the ratio of the electric field on top to the electric field below Grid 2 plate and measuring the total ion charge at the G1 plate. Figure 3.33 shows the total amount of charge going through Grid 2 as a function of the ratio of the electric fields. From the fit it was found that with a ratio of electric fields equal to 3, the transmission of barium ion charge is already greater than 90%. A ratio of electric fields equal to 3 was used in the mobility and fluorescence experiments of barium ions in xenon gas both at the accelerator plate grid and the Grid 2 grid.

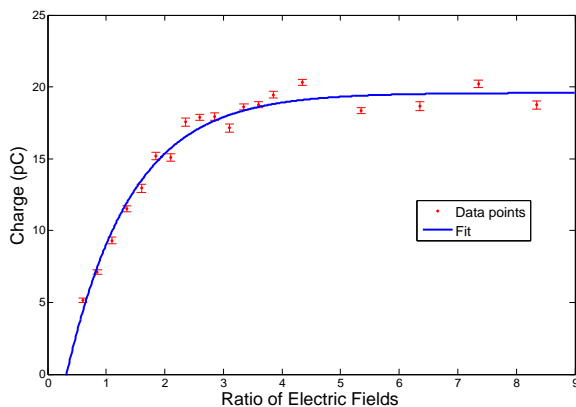


**Figure 3.33:** Charge transmitted through Grid 2 as a function of the ratio of electric fields.

According to Paschen’s law for high pressures, the breakdown voltage decreases as the pressure is reduced. For the range of pressures at which the mobility experiments are performed, between 50 Torr to 700 Torr, the voltage that can be applied to the electrode plates is quite limited at low pressure. Breakdown also prevents doing experiments at very low pressures, typically below 50 Torr, because at low voltages the electric field is not strong enough to pull most of the ions from the barium tip to the G1 plate.

The location of the ablation spot is determined by taking pictures of the metal tip before and after the experiments. A spot on the metal tip can be clearly seen after several ablation pulses hit the metal tip. Two pictures of the metal tip are shown in Figure 3.34. One of the pictures shows the metal tip at the beginning of the experiment, and the second picture

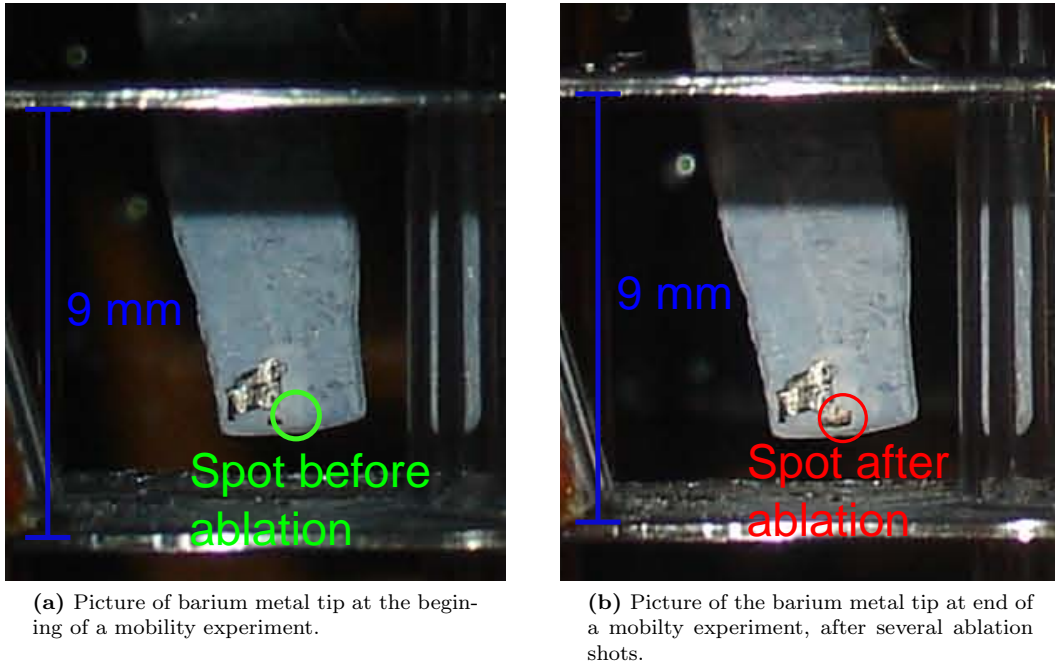


**Figure 3.34:** Pictures of metal tip used to determine the ablation spot.

shows the metal tip at the end of the experiment, in which the ablation spot can be observed. The spacing between the plates and the length of the metal tip are known and are used as a reference to calculate the position of the ablation spot. The resolution of the pictures is high enough to locate the center of the ablation spot with an accuracy of  $\pm 0.1$  mm. In the case of the BaAl getter, the location of the ablation spot is determined by taking a video while the laser light hits the getter; the accuracy in the location of the center of the ablation spot for the getter is  $\pm 0.5$  mm

### 3.4.2 Gas handling for mobility experiments

The gas handling system used for the mobility experiments of  $\text{Ba}^+$  in Xe gas is the same as that in experiments with liquid xenon, including purity measurements [20]. The principle of operation of the gas handling system is the same as discussed in section 3.1.3, except that the mobility experiments are performed with the copper cell at room temperature. Then the xenon gas flows through the SAES MonoTorr purifier, as illustrated in Figure 3.4. A small

portion of the transfer line is first filled with xenon before the purifier, and the cell is slowly filled with xenon gas until the desired pressure is reached. A Wallace & Tiernan absolute pressure gauge model FA-160 PP12079 is used to read the gas pressure inside the copper cell. The pressure gauge has a range from 0 to 800 Torr. The gauge is mounted at the top of the vacuum chamber, on a 3-3/8 inch flange 6-way cross, which connects to the top of the copper cell. After a set of experiments is completed, the xenon gas is pumped away and the copper cell is evacuated.

The mobility of  $\text{Ba}^+$  ions was also measured in Ar gas. The Ar gas was accumulated in the copper cell without going through the SAES MonoTorr purifier. The transfer line between the Ar bottle and the vacuum chamber was filled with Ar gas, and then it was added to the copper cell by slowly opening a swagelok valve between the transfer line and the chamber. The purity of the argon gas used for the experiments, according to the supplier, is 99.9999%. The Ar gas was pumped out of the copper cell after a set of experiments was completed.

### 3.5 Fluorescence Detection

In the fluorescence experiments, barium ions are created by laser ablation of the barium metal target and then drawn to the Grid 1 plate by electric fields. The ions are excited with a 493 nm tunable dye laser beam that passes between the accelerator and the Grid 2 electrode plates. The laser is a Coherent CR599 tunable dye laser, pumped by a Coherent Innova 200 UV Krypton laser. The typical power of the pump laser is between 1.0 W and 2.0 W and the output power of the dye laser is a few mW. The dye laser can be tuned from 450 nm to 510 nm using Coumarin 480 dye. The wavelength is adjusted with a birefringent filter mounted inside the dye laser cavity. The dye is mixed with ethylene glycol (EG) and benzyl alcohol (BzOH) using a proportion EG/BzOH of 7/2. At optimum concentration, the dye absorbs 70% to 80% of the pump laser. During operation, the dye solution tends to

be chemically degraded. Therefore, the dye solution is replaced from time to time, typically after 40 W · hr of use.

### 3.5.1 Light Collection Setup

A simplified schematic diagram of the light collection setup is shown in Figure 3.35. Fluorescence light is collected by a 10 cm focal length lens, which makes the collected light rays approximately parallel. This light was focused by a 50 mm Nikon camera lens, with the focus set to infinity, onto the input slit of the spectrometer. The spectrometer has an f-number of  $f/4$ , which limits the amount of light that can be collected. The combination of the two lenses gives a total magnification of  $\frac{1}{2}$ .

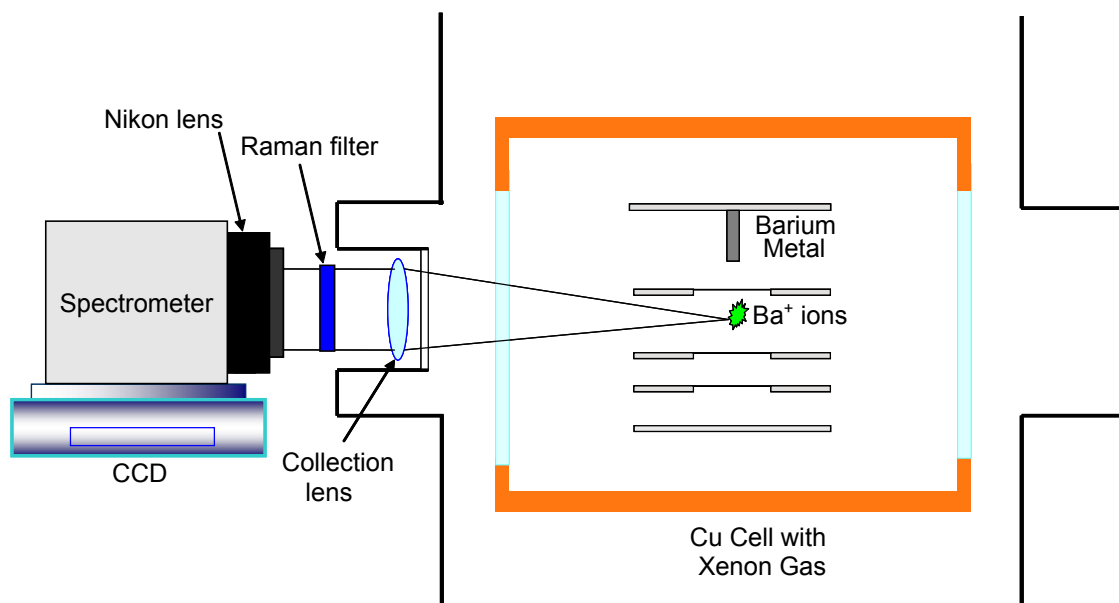


**Figure 3.35:** Schematic diagram of the fluorescence detection setup

A 514 Semrock Raman edge filter placed before the Nikon lens is used to block the scattered light at the excitation wavelength 493.4 nm and pass the emission light at 650 nm. The transmission curve for the Raman edge filter, provided by the manufacturer, is shown in Figure 3.36. It blocks wavelengths below 514 nm at normal incidence with an attenuation greater than OD6 and it has a transmission greater than 98 % above the cutoff wavelength.

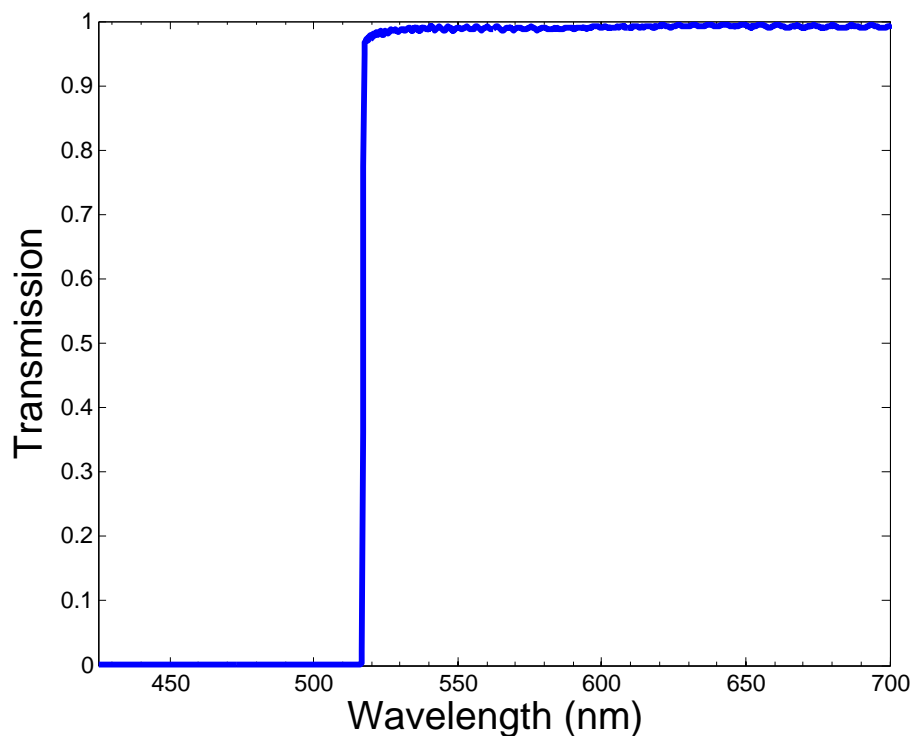


**Figure 3.36:** Transmission of Raman filter

The  $\text{Ba}^+$  fluorescence light is spectrally dispersed in an Acton SP-2150i spectrometer, and then it is detected at the output focus of the spectrometer by a Spec-10 liquid nitrogen cooled CCD camera from Princeton Instruments. The spectrometer has two different gratings, one of them with 300 lines/millimeter (1/mm) and the other with 600 l/mm, with an approximate wavelength resolution of 0.4 nm and 0.2 nm respectively. The gratings can be easily switched with the use of WinSpec software interface for the Spec-10 system. Most of the fluorescence experiments of  $\text{Ba}^+$  in xenon gas were done with the 600 l/mm to achieve better resolution.

The CCD chip is a 2 dimensional array of 1340x400 pixels with dimensions of 26.8 mm by 8 mm. It was cryogenically cooled with liquid nitrogen and operated at temperatures in the range of  $-100^\circ\text{C}$  to  $-120^\circ\text{C}$ . By lowering the temperature of the CCD array the dark current is reduced to essentially zero, and greater sensitivity is achieved. The camera can be operated in imaging or spectroscopy mode. In imaging mode the camera collects real

image data. This mode is useful for the initial setup of the experiment and the alignment of the camera. In spectroscopy mode pixels in a column are grouped together, and the data is displayed as a spectrum. This mode is used to detect the fluorescence of barium ions in xenon gas. In this mode the readout noise is greatly reduced.

The Rayleigh scattered light from the xenon gas was used to align the camera. The alignment was done with the camera in imaging mode, the Raman filter and the spectrometer grating acting as a mirror by setting it for zero-order diffraction. The scattered light from excitation beam was imaged at the input slit of the spectrometer. An adjustable slit with setting between  $100\ \mu\text{m}$  to  $150\ \mu\text{m}$  allows only the region of the excitation laser to be imaged. This eliminates scattering from plates and insulators. Once the camera was aligned and the excitation laser image was centered, the Raman filter was placed in front of the Nikon camera before starting to take spectroscopy data.

### 3.5.2 Single mode operation of excitation laser

Unlike fluorescence spectra of  $\text{Ba}^+$  in solid and liquid xenon where the absorption spectrum is broad, on the order of a few nanometers, the absorption spectrum of  $\text{Ba}^+$  in xenon gas is much narrower, on the order of a few GHz. Thus, it is important to have a laser with a narrow bandwidth to obtain an excitation spectrum of  $\text{Ba}^+$  in xenon gas. The excitation spectrum  $\text{Ba}^+$  in xenon gas was recorded by scanning the frequency of the dye laser across the spectral region near the known resonant frequency of the  $6s\ ^2S_{1/2}$  to  $6p\ ^2P_{1/2}$  transition in vacuum ( $20261.56\ \text{cm}^{-1}$ ).

A diagram of the laser system and monitoring equipment is shown Figure 3.37. The frequency was measured with a Burleigh WA-20VIS wavemeter, which can read the laser frequency with a resolution of  $0.01\ \text{cm}^{-1}$ . The laser frequency could be measured while simultaneously doing experiments by splitting off a small portion of the laser beam with a glass microscope slide. The alignment of the dye laser to the wavemeter was accomplished relatively easily with the use of a trace beam from a He-Ne laser inside the wavemeter. Once

the alignment is completed, the trace beam was blocked with a blue color filter to prevent it from reaching the Xe gas region.

The dye laser was operated in single frequency mode with the use of a thin etalon and thick etalon that have a free spectral range of 225 GHz and 10 GHz respectively. The thin etalon reduces the laser bandwidth to approximately 1.2 GHz in 3 axial modes, and the thick etalon in conjunction with the thin etalon provide operation at single frequency. The frequency was first adjusted with the birefringent filter, and the finer adjustments were done by tilting the angles of the thin and thick etalon. The excitation spectra scans were done in steps of about 500 MHz, by mode hopping the laser with small tilts in the angle of the thick etalon for small frequency shifts and tilting the angle of the thin etalon for larger frequency shifts.

The frequency shift of the dye laser was monitored with a Tropol Model 240 Spectrum analyzer with a Free Spectral Range (FSR) of 7.5 GHz with 1 cm mirrors. It consists of a Fabry-Perot interferometer with two confocal mirrors. When the frequency modes of a stable laser are measured with a the spectrum analyzer, the modes drift less than 30 MHz over 200 seconds.

### 3.5.3 Light Detection Efficiency

The efficiency of the fluorescence light collection and detection, in counts per photon emitted  $\epsilon_{total}$ , depends on a number of factors listed in Table 3.4 and discussed below. One of the most important factors is the collection efficiency  $\epsilon_{CE}$ , which is determined by the solid angle  $\Omega$  of the light rays from the barium ions that pass through the detector. According to Figure 3.38 a lens of effective diameter  $D$  and object distance approximately equal to the focal length  $f$

$$\epsilon_{CE} = \frac{\Omega}{4\pi} \approx \frac{\pi D^2/4}{4\pi f^2} = \frac{D^2}{16f^2} \quad (3.16)$$

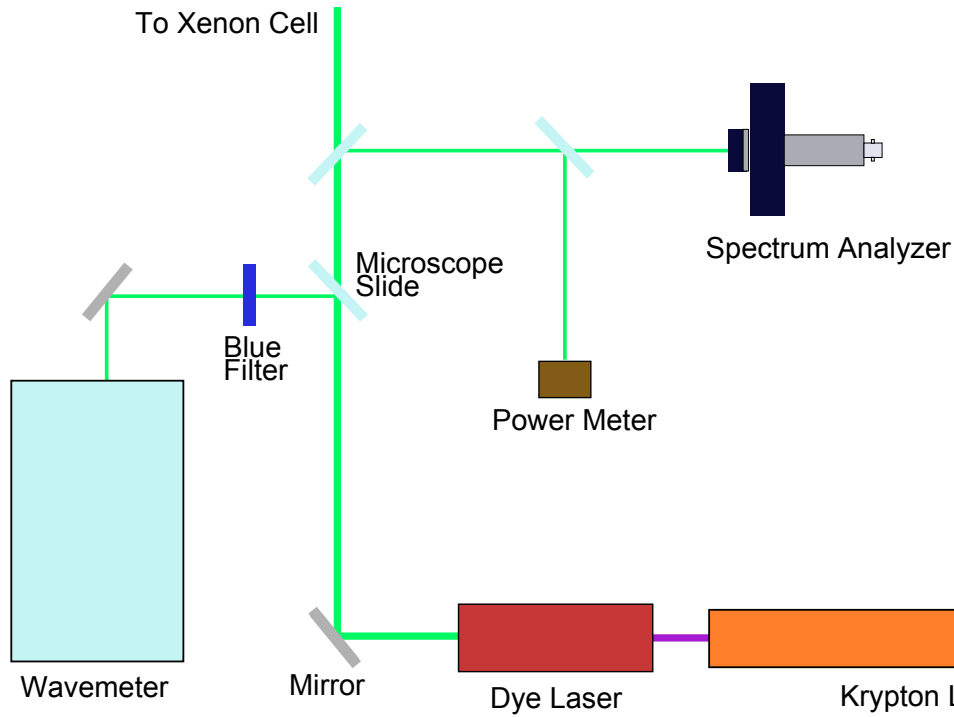


**Figure 3.37:** Schematic diagram of the laser system

The limiting factor for rays in the system is the f-number of the spectrometer,  $f/4$ . This reduces the effective diameter of the cone of light rays collected by the collection lens as can be seen in Figure 3.39. The effective diameter  $D_{eff}$  is related to the f-number of the spectrometer,  $f/\# = f_2/D_{eff}$ , where  $f_2$  is the focal length of the camera lens. Using  $D_{eff} = f_2/4$ , the collection efficiency using (3.16):

$$\epsilon_{CE} = \frac{f_2^2}{256f_1^2} \quad (3.17)$$

For  $f_1=10$  cm, and  $f_2= 50$  mm,  $\epsilon_{CE}=9.8 \times 10^{-4}$ .

The transmission of different optical parts of the detection system are also important. One uncoated lens has 88% transmission and a coated lens 92% transmission. The window of the copper cell and the window of the vacuum chamber have 96% transmission each. The three mirrors used to direct the fluorescence light to the spectrometer have a reflectance of 88% each. The transmission of the Raman filter is 98%. The listed efficiencies of the spectrometer and the CCD camera are for 650 nm light, which is the wavelength detected

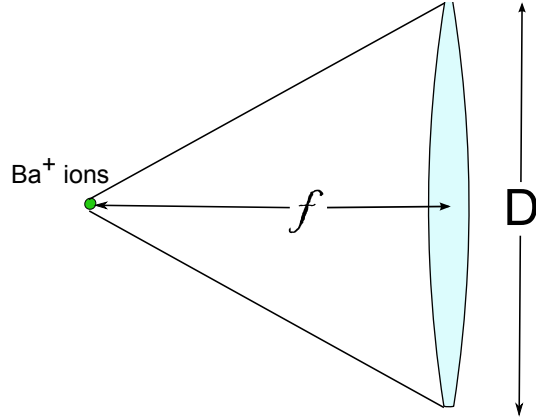


**Figure 3.38:** Solid angle of the collection lens.

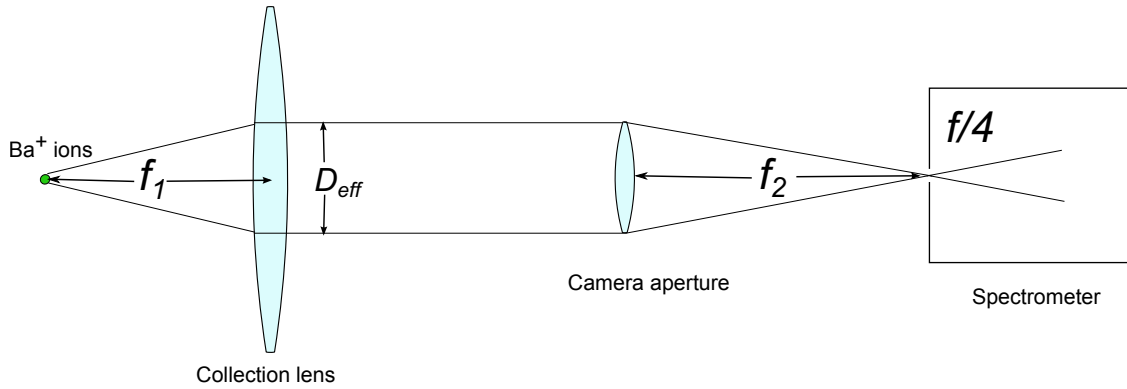


**Figure 3.39:** The solid angle of the collection lens is reduced due to the limitation in the f-number of the spectrometer.

during the fluorescence experiments of barium ions in xenon gas. The manufacturers of the CCD and spectrometer specify a quantum efficiency of the CCD,  $\epsilon_{QE}$ , of 90% at 650 nm, or 0.90 photoelectrons/photon and a grating transmission,  $\epsilon_{grating}$ , of 60% in first order. The CCD camera has a digitization factor,  $\epsilon_{digitization}$ , of 0.5 counts per photoelectron when operating in slow ADC (Analog-to-digital converter) mode. This means that two detected photons are required to generate one count in the CCD detector.

The total detection efficiency including all of the factors contributing to the fluorescence detection efficiency in Table 3.4 is estimated to be  $1.31 \times 10^{-4}$  counts per fluorescence photon emitted. It can be used to estimate the total number of fluorescence counts per ion and

the ion fluorescence efficiency. The predicted number of counts calculations is discussed and compared to the experimental results in Chapter 4.

**Table 3.4:** Detection efficiency

Collection Efficiency	$\epsilon_{CE}$	9.8E-4
Uncoated Lens Transmission	$T_{lens\_uncoat}$	0.88
Coated Lens Transmission	$T_{lens\_coat}$	0.92
Window Transmission	$T_{window}$	0.92
Mirrors Reflection	$R_{mirror}$	0.68
Raman Filter Transmission	$T_{raman}$	0.98
CCD Quantum Efficiency	$\epsilon_{QE}$	0.90
Grating Transmission	$\epsilon_{grating}$	0.60
Digitization Factor	$\epsilon_{digitization}$	0.50
<b>Total Detection Efficiency</b>	<b><math>\epsilon_{total}</math></b>	<b>1.31E-4</b>

The detection efficiency was experimentally measured by detecting scattered light from a 633 nm He-Ne laser on a white card, using the same setup that was used for the fluorescence experiments. A diagram of the setup for the measurement of the detection efficiency is shown in Figure 3.40. An aperture was placed between the white card and the collection lens created an effective diameter of 1.25 cm at the 10 cm lens collection lens. The detection efficiency was calculated by measuring the total number of counts detected by the CCD and comparing them to the power read by a powermeter placed right after the aperture.

The detection efficiency was measured as a function of the distance between the white card and the collection lens to take into account the differing depth of fluorescence sites from the lens. The results are shown in Figure 3.41. The peak value of the detection efficiency is 0.109 counts/photon. The peak total detection efficiency, including the collection efficiency and the transmission of the windows and the raman filter, is then  $0.96 \times 10^{-4}$ . This is not too different from the estimate in Table 3.4.

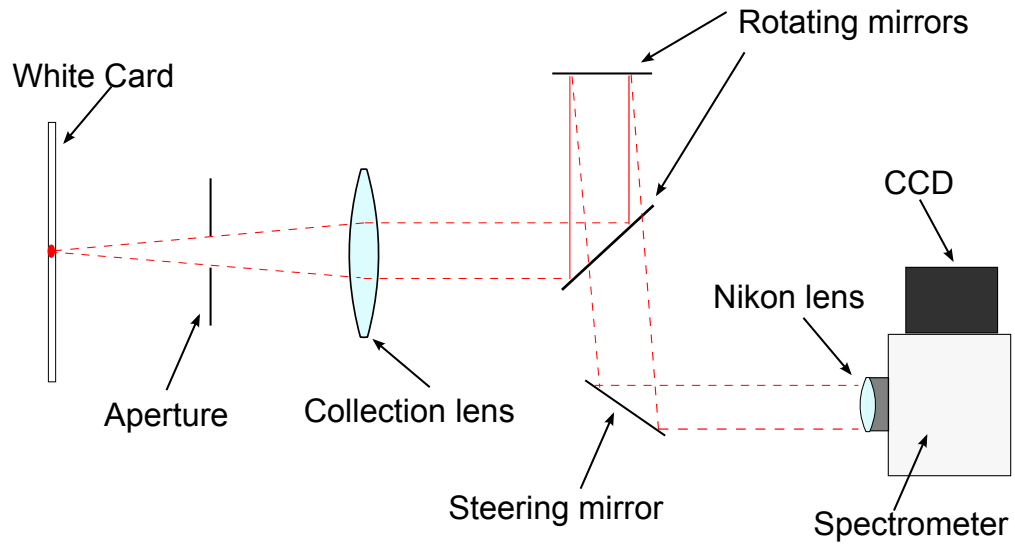


**Figure 3.40:** Diagram of experiment to determine the detection efficiency.

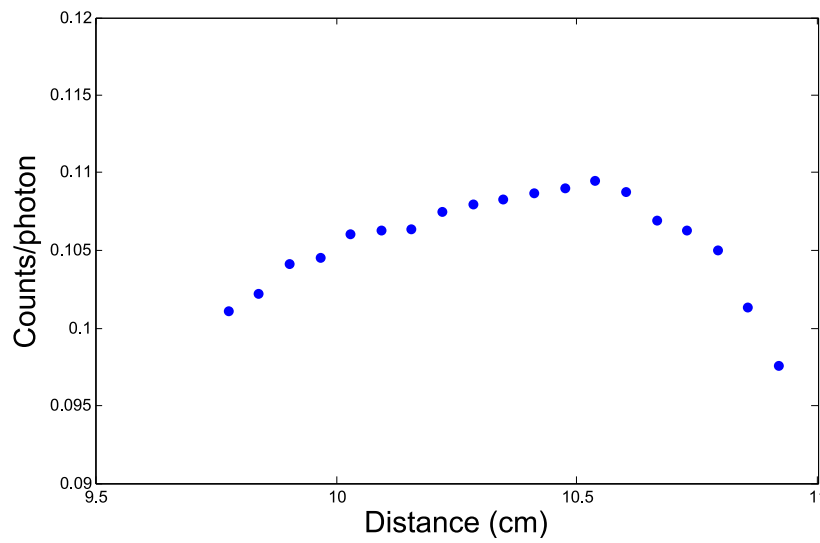


**Figure 3.41:** Detection efficiency versus distance between white card and collection lens.

The detection efficiency was also measured as a function of horizontal position. This was done by moving the position at which the laser hit the white card and detecting the scattered light at different horizontal positions. A plot of the horizontal variation of the detection efficiency is shown in Figure 3.42. It is fairly narrow. The data is fit to a Gaussian function of the form  $A \exp(-(x - b)^2/2\sigma^2)$ .

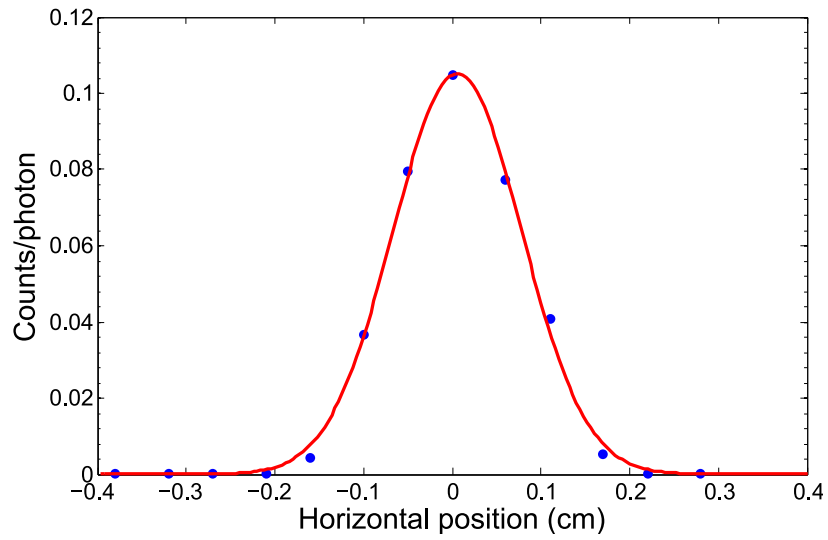


**Figure 3.42:** Variation of the detection efficiency with the collection lens 10.5 cm away from the white card.

The horizontal variation of the detection efficiency was measured for different distances between the collection lens and the white card. The width  $\sigma$  of the Gaussian fit is plotted versus the distance between the lens and the white card in Figure 3.43. The width  $\sigma$  of the Gaussian fit is nearly constant across the region of interest. The average of the width parameter  $\sigma$  is 0.070 cm.

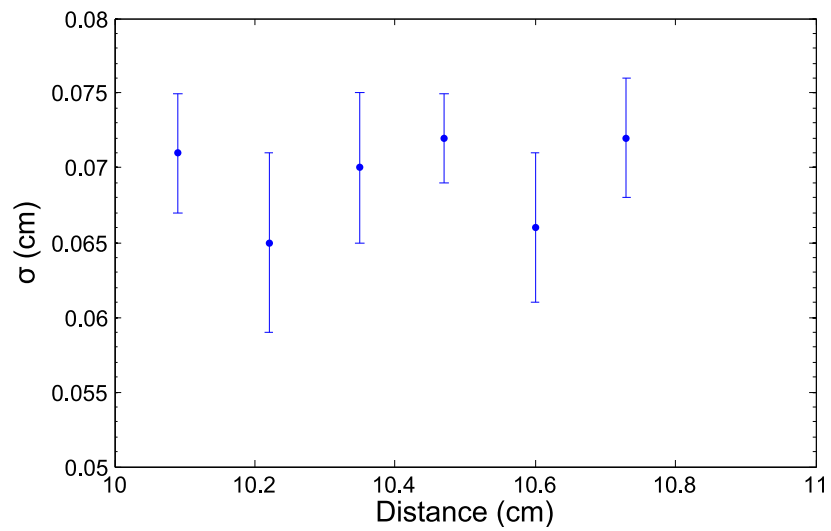


**Figure 3.43:** Width of the horizontal detection efficiency as a function of distance between the collection lens and the white card.

## 4 Results

In this chapter the results and analysis of experiments to measure the purity of liquid xenon and the mobility and fluorescence of  $\text{Ba}^+$  in xenon gas are discussed. Results from purity measurements in liquid xenon are presented in section 4.1. The effects on purity of condensing xenon going through the purifier versus bypassing the purifier and of using the recirculation system are discussed. The effects on the purity of liquid xenon of ablation of a barium metal tip is also discussed. The results of the mobility of barium ions in xenon gas are presented in section 4.2. The dependence of the measured mobility of barium ions in xenon on pressure is discussed, and compared with results of mobility of barium ions in argon gas. The results are interpreted in terms of a molecular association and dissociation model. Finally, in section 4.3, measurements of the pressure broadening and fluorescence efficiency of barium ions in xenon gas are reported.

### 4.1 Purity Measurements

As discussed in Chapter 2, the electron lifetime  $\tau_e$  in LXe is a function of the concentration of electronegative impurities in liquid xenon. The electron lifetime is found by measuring the electron transmission in liquid xenon. The determination of the electron lifetime after purification and recirculation of liquid xenon is presented in this section, as well as the effect of ablation of a barium metal target on the electron lifetime.

#### 4.1.1 Electron Lifetime Measurements

The relationship between the electron lifetime and the electron transmission was discussed in section 3.2.3. The electron transmission  $R$  can be written in terms of the electron lifetime  $\tau_e$  as

$$R = e^{-T_d/\tau_e} \quad (4.1)$$

where  $T_d$  is the electron drift time defined in section 3.2.3 that can be found from the current on the signal plates. The electron lifetime is therefore

$$\tau_e = T_d / (-\ln R) \quad (4.2)$$

The electron transmission as a function of the electron lifetime is plotted in Figure 4.1. The plot is for the electric fields and drift times given in Table 4.1. From this plot it can be seen that the purity monitor has a high sensitivity from 2  $\mu\text{s}$  to 200  $\mu\text{s}$ . Measurements of transmissions greater than 95% are needed to determine lifetimes greater than 100  $\mu\text{s}$ .

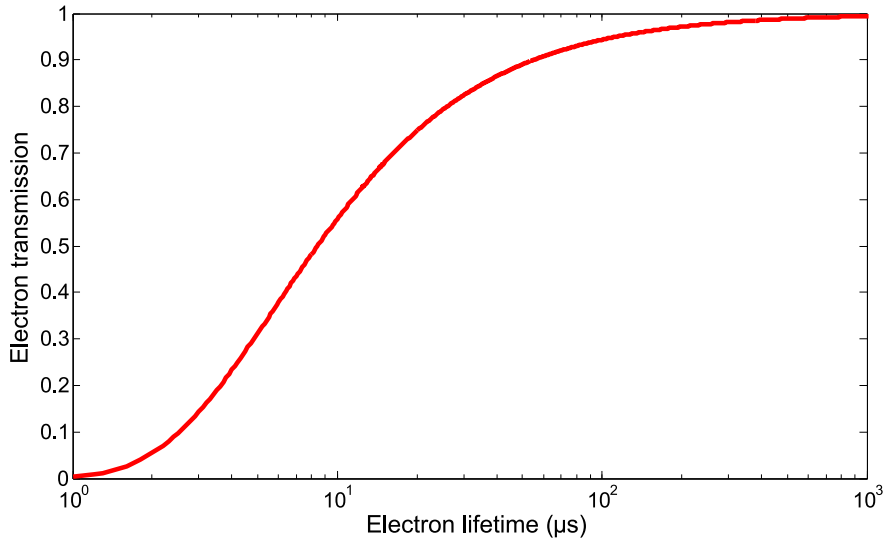


**Figure 4.1:** Electron transmission versus electron lifetime.

**Table 4.1:** Typical voltages configuration, electric fields and drift times.

$V_C = 0 \text{ V}$	$E_1 = 50 \text{ V/cm}$	$T_C = 3.3 \mu\text{s}$	$k_s = 1.7 \times 10^{11} \text{ M}^{-1} \text{ s}^{-1}$
$V_{G1} = 20 \text{ V}$	$E_2 = 150 \text{ V/cm}$	$T_G = 2.6 \mu\text{s}$	$k_s = 1.2 \times 10^{11} \text{ M}^{-1} \text{ s}^{-1}$
$V_{G2} = 35 \text{ V}$	$E_3 = 406 \text{ V/cm}$	$T_A = 3.1 \mu\text{s}$	$k_s = 1.1 \times 10^{11} \text{ M}^{-1} \text{ s}^{-1}$
$V_A = 360 \text{ V}$			

The sensitivity of the electron lifetime can be improved by increasing the drift time. This can be done by increasing the length of the purity monitor. However, the purity monitor at Colorado State University is limited to the current dimension of the liquid xenon cell. In

larger detectors like in EXO-200 or nEXO, where the electrons drift tens of centimeters, the drift time is increased by 1-2 orders of magnitude.

The electron lifetime is related to the oxygen equivalent concentration of impurities  $[X]$  by

$$\tau_e = \frac{1}{k_s[X]} \quad (4.3)$$

where the attachment rate constant for  $O_2$  at 100 V/cm is  $k_s = 1.6 \times 10^{11} \text{ M}^{-1}\text{s}^{-1}$  and  $7 \times 10^{11} \text{ M}^{-1}\text{s}^{-1}$  at 1000 V/cm [30]. The weighted average of  $k_s$  for the voltages listed in Table 4.1 is  $k_s = 1.35 \times 10^{11} \text{ M}^{-1}\text{s}^{-1}$ . An oxygen equivalent impurity concentration is an impurity number density scaled by the relative attachment rates of that species and oxygen.

The relationship between electron transmission and concentration of impurities in part per billion (ppb) for the voltage configuration and drift times from Table 4.1 is given in Figure 4.2. There is a high sensitivity to impurity concentrations in the 2-200 ppb range in this purity monitor.

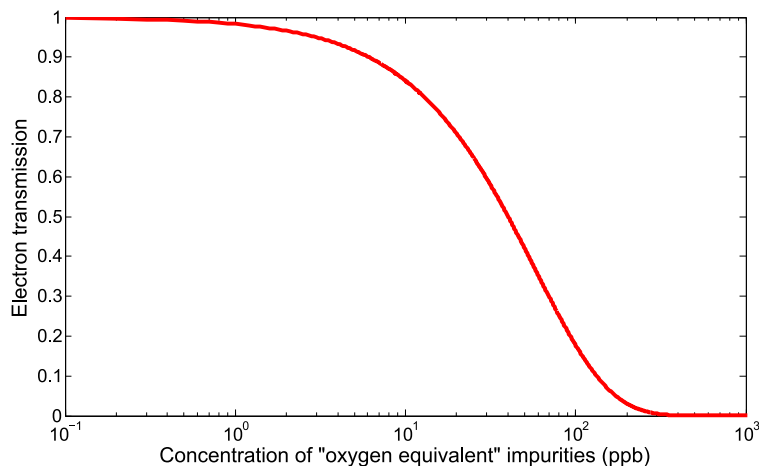


**Figure 4.2:** Electron transmission versus impurity concentration for voltages listed in Table 4.1

### 4.1.2 Effects of Recirculation on the Electron Lifetime

The recirculation system removes impurities in the liquid xenon in the copper cell by evaporating liquid xenon in the recirculation pipe, flowing it through the SAES purifier and then recondensing it in the cell. The flow of xenon is proportional to the heat applied to the

recirculation pipe, as can be seen in Figure 4.3. There is a gradual response of the flow to a change in heat applied to the recirculation pipe, and after some time it becomes stable.

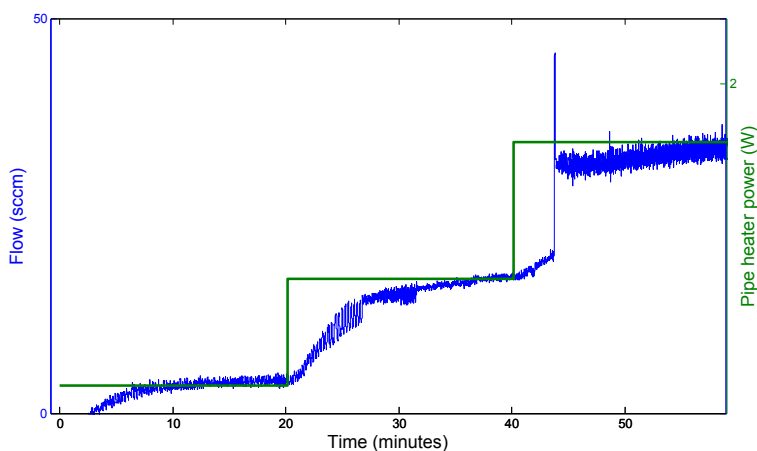


**Figure 4.3:** Xenon flow and heat applied to the recirculation pipe. The temperature of the copper cell was kept constant at 170 K while doing this experiment.

The flow can be steady for several hours; this allows spectroscopy experiments and purity measurements to be performed while recirculating. Steady recirculation for a period of more than 16 hours at a flow rate of approximately 65 sccm is shown in Figure 4.4. Since the copper cell is filled with approximately 86 standard liters of xenon, a complete recirculation takes about 22 hours.

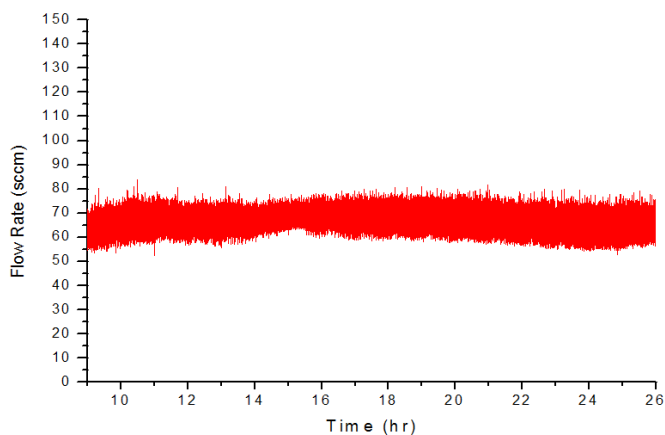


**Figure 4.4:** Steady recirculation

One way to test if the recirculation of xenon actually helps to remove impurities is by measuring the electron lifetime before and after recirculation. Figure 4.5 shows the electron transmission before and after recirculation. Xenon was purified with the SAES purifier before it was condensed in the copper cell. After the liquid xenon was condensed, purity measurements were taken for about 85 minutes. Then xenon was recirculated for about three hours while taking purity measurements at the same time. The average transmission after condensation though the purifier and before recirculation was very high is  $0.976(0.003)$ . After starting recirculation the average transmission was also high  $0.983(0.002)$ . The slight increase in transmission is smaller than the systematic error. The initial created charge was 170 fC on average, which would give a systematic error of about 3%, according to the fit obtained in Chapter 3 that relates the transmission to the initial charge. This transmission level corresponds to an electron lifetime of approximately  $300 \mu\text{s}$ , according to Figure 4.1.

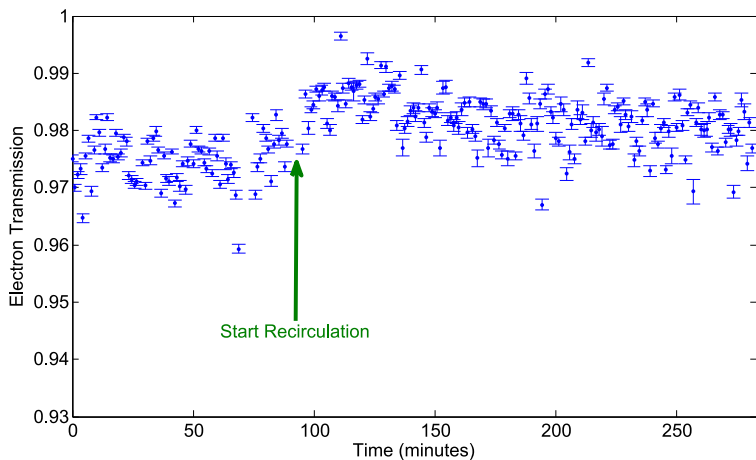


**Figure 4.5:** Electron transmission before and after recirculation. The liquid xenon was initially condensed by going through the SAES purifier. Error bars are statistical only.

In a different experiment, the effects of recirculation on the electron life time were tested with xenon initially condensed bypassing the purifier. The results are shown in Figure 4.6. The experiment was done using electrode plate Configuration A from table 3.1 and voltages  $V_C = 0V$ ,  $V_{G1} = 45V$ ,  $V_{G2} = 112.5V$ , and  $V_A = 1750$ . The purity right after condensing the xenon ( $t=0$ ) was noticeably lower, with an electron transmission of less than 0.5, which corresponds an electron lifetime of  $< 8 \mu\text{s}$  and an impurity levels of  $\sim 40$  ppb from Figure 4.2.

Purity measurements were taken approximately every minute. The electron transmission increased for the first three hours from 0.5 to about 0.8 without recirculating. Then, the electron transmission stayed constant around 0.8. Recirculation at a flow rate of approximately 60 sccm was started approximately 12 hours after condensation. The electron transmission decreased right after the recirculation started, from 0.8 to roughly the same initial transmission measured after condensation. The recirculation continued and it took more than 45 hours to increase the electron transmission from 0.5 to more than 0.8, which corresponds to an electron lifetime of approximately  $26 \mu\text{s}$ .

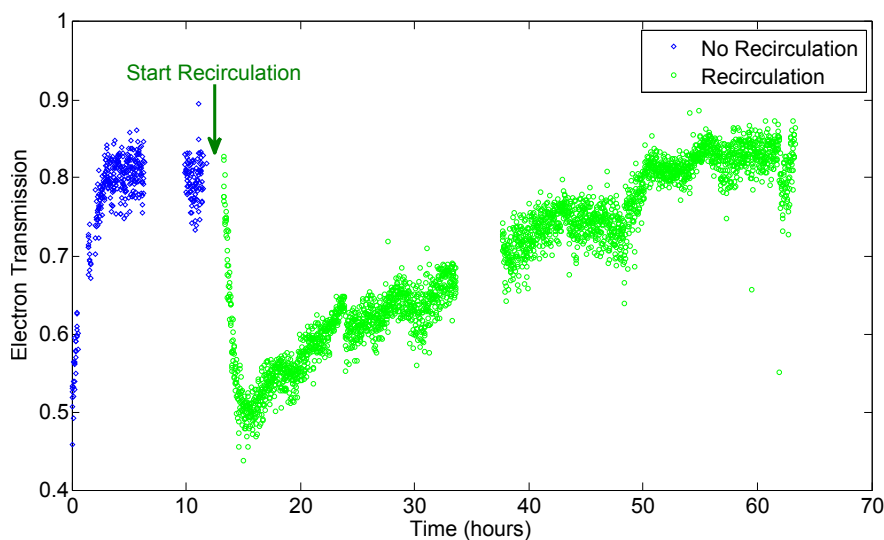


**Figure 4.6:** Electron transmission ( $\frac{Q_A}{Q_{C+G1}}$ ) before and after recirculation. The liquid xenon was initially condensed bypassing the SAES purifier.

Three main conclusions can be drawn from these experiments: (1) condensing the liquid xenon through the purifier results in a high purity; (2) condensing liquid xenon bypassing the purifier results in a lower electron lifetime; (3) recirculating liquid xenon is effective in increasing the electron lifetime when the concentration of impurities is substantial.

### 4.1.3 Effects of Ablation on the Electron Lifetime

The electron lifetime was measured after some spectroscopy experiments on barium ions in liquid xenon in which a barium target was ablated to find out if the ablation process

introduced impurities into the liquid. The measurements shown in Figure 4.7 were performed with the electrode plates in the Configuration A of Table 3.1. Various combination of voltages on the plates were used which produced different ratios of electric fields that are shown in Table 4.2.

**Table 4.2:** Configuration of voltages for purity measurements.

E Field Ratio	$V_C$	$V_{G1}$	$V_{G2}$	$V_A$
$\frac{E_3}{E_2} = \frac{E_2}{E_1} = 3$	0 V	20 V	35 V	360 V
$\frac{E_3}{E_2} = \frac{E_2}{E_1} = 4$	0 V	20 V	40 V	690 V
$\frac{E_3}{E_2} = \frac{E_2}{E_1} = 5$	0 V	20 V	45 V	1050 V
$\frac{E_3}{E_2} = \frac{E_2}{E_1} = 6$	0 V	20 V	50 V	1500 V

For results of purity experiments shown in Figure 4.7, xenon was always condensed before ablation using the purifier and there was no recirculation. The purity measurements were performed a few minutes after the last laser ablation was done. The purpose of these measurements is to show the effect of ablation on the purity of liquid xenon, as well as seeing the effect of varying the ratio of electric fields between the plates. In all cases, even after hundreds of ablation shots, the electron transmission was close to 1. For transmission  $> 98\%$  a lower limit for the electron lifetime after hundreds of ablation shots is  $\tau > 300 \mu s$ , and oxygen equivalent impurities  $< 1$  ppb.

The purity measurements shown in Figure 4.7 were done at an average initial charge of approximately 50 fC. From Chapter 3, the electron transmission  $R$  depends on the initial charge  $Q$  as  $R = a + bQ + cQ^2$ , with  $a = 1.004 \pm 0.006$ ,  $b = -1.58 \pm 1.02 \times 10^{-4}$ , and  $c = -7.98 \pm 41 \times 10^{-8}$ , with the charge  $Q$  in fC. Using this charge dependence, the value of  $R$  at 50 fC is 0.992, which is off by 1.2% from the value of  $R$  at zero charge, it can be used as an estimate for the systematic error due to charge for these measurements. There is not noticeable change in the transmission when the ratio of electric fields between plates is increased. Increasing the ratios to values greater than 3 should not have a large effect in the electron transmission, as it was shown in section 3.2.5. In summary, the purity of liquid xenon remains high, with a

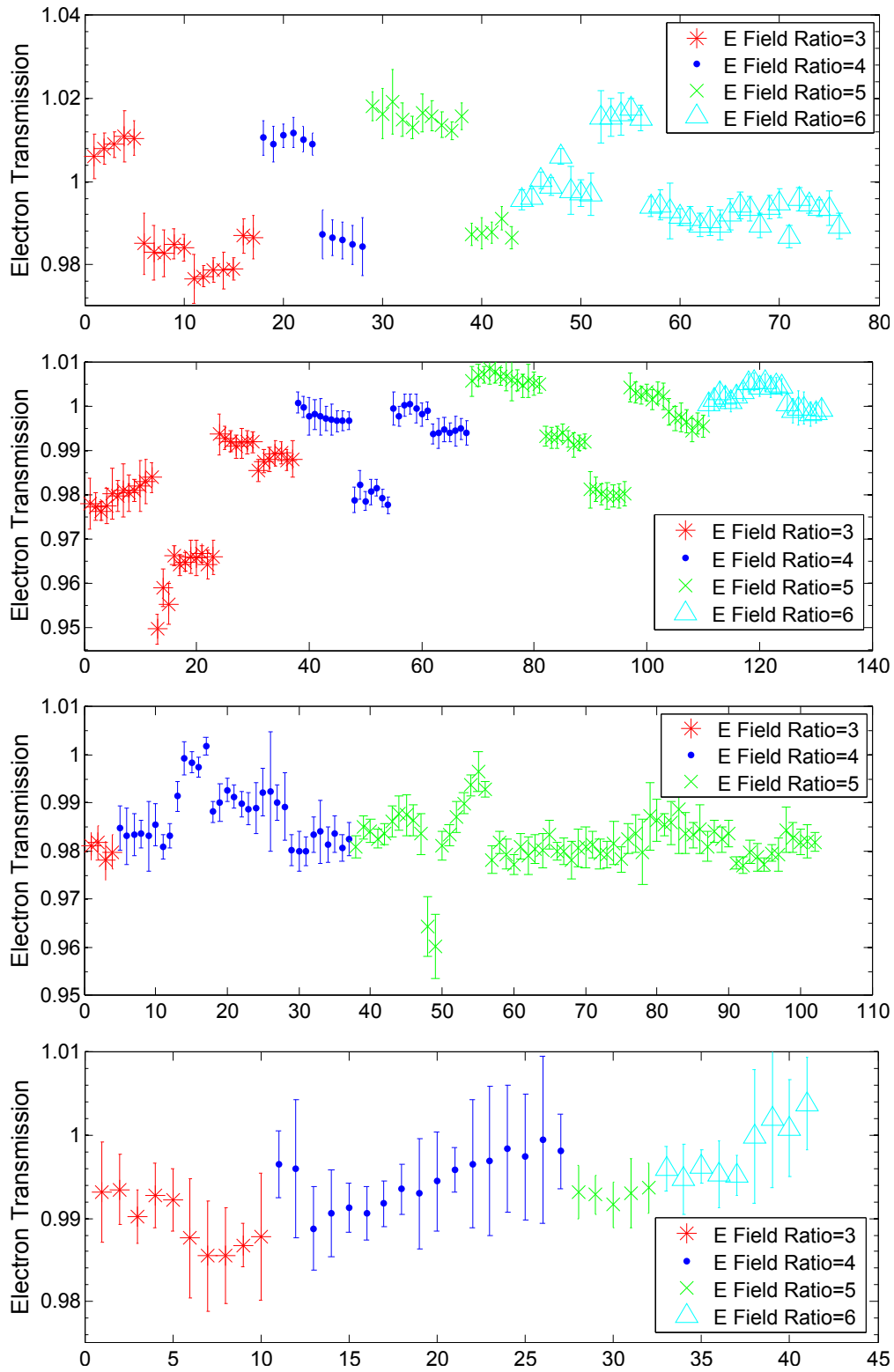


**Figure 4.7:** Purity measurements in liquid xenon after performing on the order of hundreds of ablation shots. The  $x$  axis shows the number of each purity measurements in the sequence taken.

transmission higher than 98%, even after hundreds of ablation shots. Purity measurements taken with ratio of electric fields higher than 3 give consistent results.

A plot of purity measurements before and after ablation is shown in Figure 4.8. The xenon was purified before being condensed. Purity measurements were taken for about 40 minutes before any ablation shot. The cause of the small decrease in transmission from 98% to 97% is not known. A few ablation shots were done, and then the purity was measured about 80 minutes later. No noticeable change in the electron transmission after ablation was observed. The observation that the ablation process does not introduce impurities in

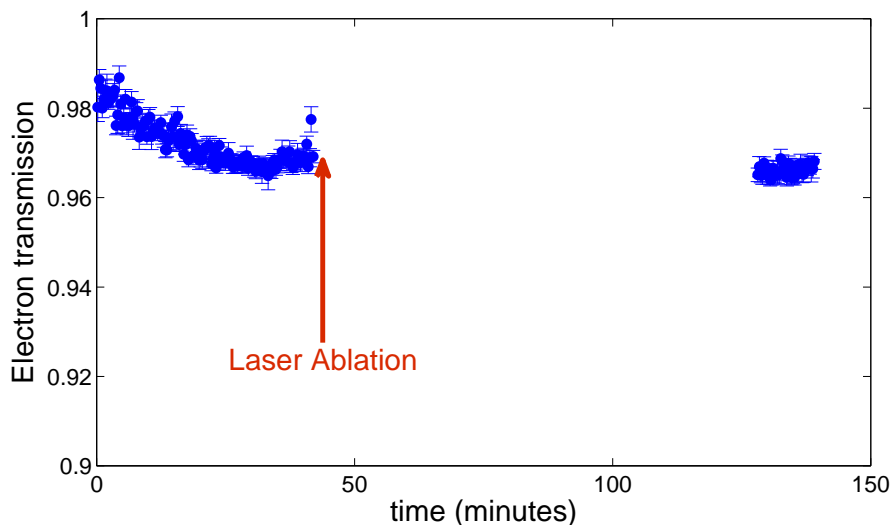


**Figure 4.8:** Measurements of the purity of liquid xenon before and after ablation.

the liquid is important for  $\text{Ba}^+$  spectroscopy experiments in liquid xenon and solid frozen xenon from liquid xenon because attachment of barium ions to electronegative impurities could make them non interacting with the laser beam.

## 4.2 Mobility Experiments

The original motivation for making mobility measurements of  $\text{Ba}^+$  in xenon gas was to know how fast the ions travel during the fluorescence experiments. However, the results of the mobility experiments turned out to be interesting in themselves. The mobility of  $\text{Ba}^+$

in xenon gas was measured first at a pressure of 1 atmosphere. However, the experimental result obtained did not agree with the theoretical value reported by M. F. McGuirk et al. [33]. There were no other experimental data for the mobility of Ba<sup>+</sup> in xenon gas. The mobility of Ba<sup>+</sup> in argon was also measured at 1 atmosphere of pressure to verify if the measurements with the CSU apparatus were consistent with the predicted theoretical values [33], and with a previous experimental result reported by S. M. Penn et al. [41] at an argon pressure of 0.2 Torr. Contrary to the mobility measurements of Ba<sup>+</sup> in xenon gas, the measured mobility of Ba<sup>+</sup> in argon gas was consistent with the predicted theoretical value and with a previous experimental result, although there was a large systematic error in those initial measurements. To resolve this discrepancy, measurements at a range of pressures were made and the formation of molecular ions in argon and xenon gas was considered. Details of these measurements and the molecular model are discussed in the following sections.

#### 4.2.1 Charge Dependence of Ionic Mobility

The mobility measurement can be affected by induced fluid motion resulting from friction forces with the moving ion charge cloud. The larger the charge, the larger is the fluid motion and its effect on the mobility measurement. A method was developed to eliminate this effect in measurements of the mobility of alkaline earth ions in liquid xenon by Jeng et. al. [34]. The true mobility is calculated with the use of equation 2.30,  $\mu_{app} = \mu_{true} + cQ^{n(E)}$ . The  $n$  power is related to the electric field, which in turn depends on the voltage applied to the Target plate. The values of  $\mu_{true}$  and  $n$  can be found by fitting the mobility data of Ba<sup>+</sup> in gaseous xenon as a function of charge to equation 2.30.

Mobility measurements of Ba<sup>+</sup> in Xe gas, at 660 Torr and 296 K with different applied voltages on the Target plate using a BaAl getter, are shown in Figure 4.9. The mobility is constant at low charge and increases at high charge. This experiment was performed using the longest of the three BaAl getters as ablation target from Figure 3.32i. The value of  $d_{eff}^2$

was  $1.7 \text{ cm}^2$ . The solid lines are fits of the data to equation 2.30. Each fit gives a value of the intercept,  $\mu_{true}$ , and a value of the power  $n$ .

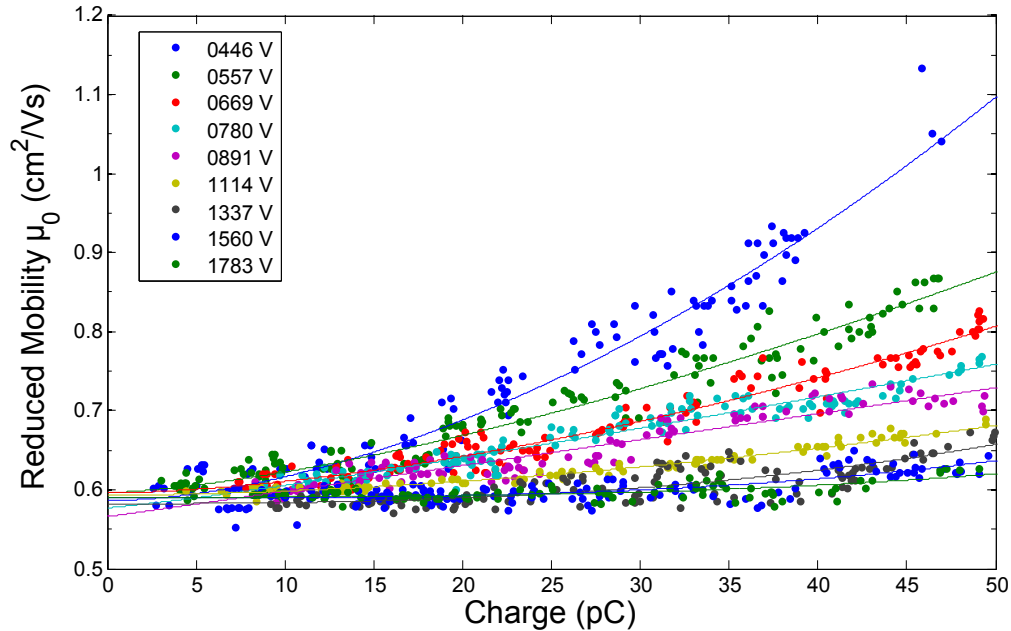


**Figure 4.9:** Charge dependence of the mobility of  $\text{Ba}^+$  in xenon gas at a pressure of 660 Torr using a BaAl getter.

The intercept of the fits is plotted as a function of the applied voltage on the Target plate in Figure 4.10. It is seen that the intercept is independent of the applied voltage on the Target plate. The red line in Figure 4.10 represents the value of the weighted average of the intercept from the fits in Figure 4.9.

The power of charge dependence is plotted as a function of the Target voltage in In Figure 4.11. For high applied voltages on the Target plate, the uncertainty in the  $n$  power is large because the measured mobility is almost independent of charge for high voltages, as seen in Figure 4.9. In Figure 4.11, the red line represents a weighted fit of the  $n$  power as a function the voltage on the Target plate. The data points with voltages 1337 V and higher are excluded from the fit due to the large uncertainty. From Figure 4.11, a constant value of  $n= 1.5$  is a reasonable choice. The data in Figure 4.9 fit with a fixed value of  $n = 1.5$  are shown in Figure 4.12. By eye, the fit looks good.

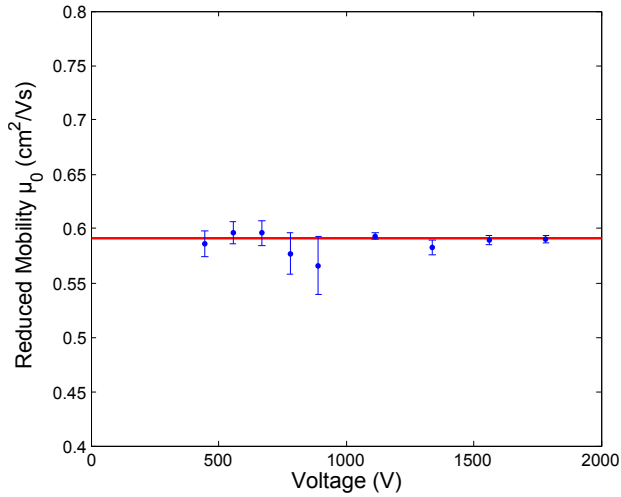


**Figure 4.10:** Intercept of the mobility as a function of voltage applied on the Target plate with xenon gas pressure of 660 Torr

A plot of the intercept as a function of applied voltage on the Target plate for  $n=1.5$  is shown in Figure 4.13. Again, the value of the intercept is seen to be independent of the voltage. The errors are reduced compared to Figure 4.10. The red line represents the weighted average of the reduced mobility. It can be seen that the both approaches produce similar average values,  $0.591 \text{ cm}^2/\text{Vs}$  in Figure 4.10 and  $0.587 \text{ cm}^2/\text{Vs}$  in Figure 4.13.

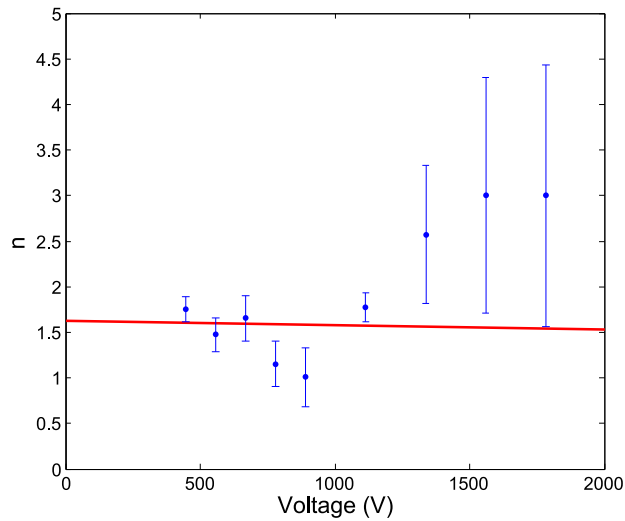


**Figure 4.11:** Power of charge dependence as a function of voltage applied on the Target plate with xenon gas pressure of 660 Torr

Mobility data of  $\text{Ba}^+$  were also taken using a metal tip as ablation target, for the configuration shown in Figure 3.32e. The charge dependence of the mobility of  $\text{Ba}^+$  in xenon at a

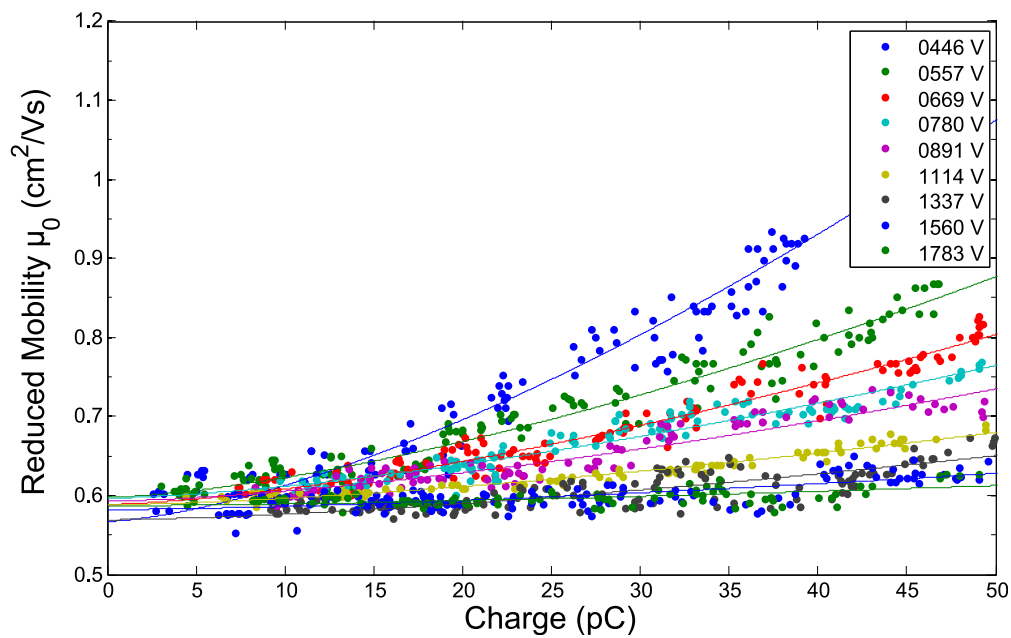


**Figure 4.12:** Charge dependence of the mobility of  $\text{Ba}^+$  in xenon gas at a pressure of 660 Torr. The fits were done with a power of  $n = 1.5$

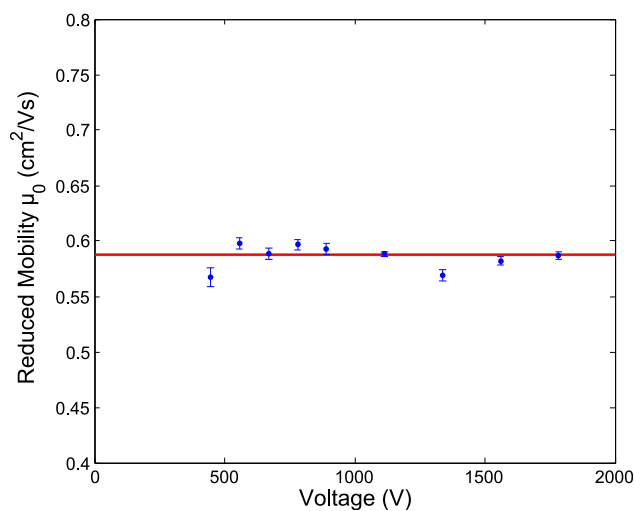


**Figure 4.13:** Intercept of the mobility as a function of voltage applied on the Target plate with xenon gas pressure of 660 Torr using a BaAl getter. The intercepts were obtained by fitting the data with a power of  $n = 1.5$

pressure of 670 Torr is shown in Figure 4.14. The fits to find the intercept were done using  $n = 1.5$ . A plot of the intercepts as a function of the applied voltage is shown in Figure 4.15 with an average value of  $0.530(0.004) \text{ cm}^2/\text{Vs}$ .

The mobility of  $\text{Ba}^+$  in argon at a pressure of 620 Torr was recorded as a function of charge. The configuration used was the barium metal tip shown in Figure 3.32e. The data is shown in Figure 4.16 and the intercept as a function of applied voltage is shown in Figure 4.17. The mobility of barium ions in argon also has a similar dependence on the charge, thus the same method to find the intercept can be applied. The value of the intercept is  $1.808(0.004) \text{ cm}^2/\text{Vs}$ .

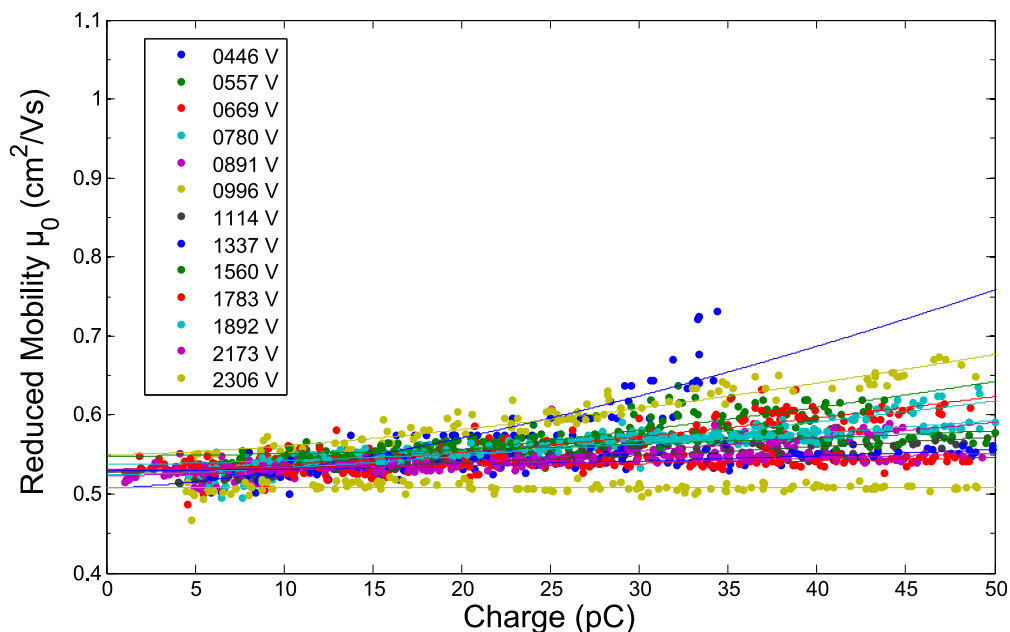


**Figure 4.14:** Charge dependence of the mobility of  $\text{Ba}^+$  in xenon gas at a pressure of 670 Torr using a barium metal tip.

The parameter with the largest fractional systematic uncertainty in these mobility measurements is  $d_{eff}^2$ . In order to assess the accuracy of the calculated  $d_{eff}^2$ , the mobility of  $\text{Ba}^+$  in xenon was measured hitting two different spots on the metal tip. The applied voltage and the xenon pressure were the same. In one case the metal tip was ablated 0.5 mm above the lower end of the tip. The calculation of  $d_{eff}^2$  with SIMION was  $d_{eff1}^2 = 1.84 \text{ cm}^2$  for this case.

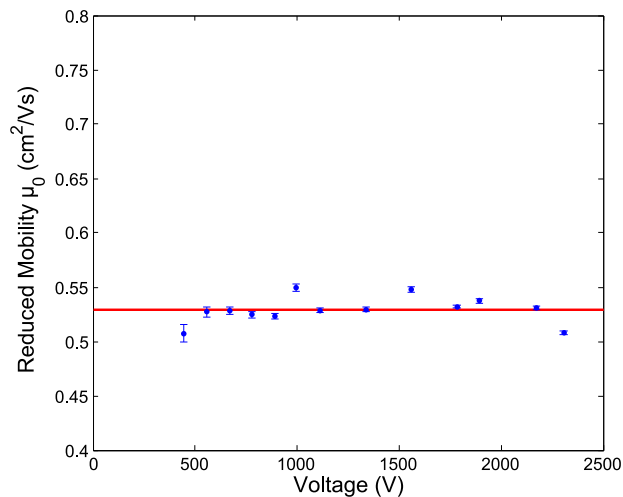


**Figure 4.15:** Intercept of the mobility as a function of voltage applied on the Target plate with xenon gas pressure of 670 Torr using a barium metal tip.

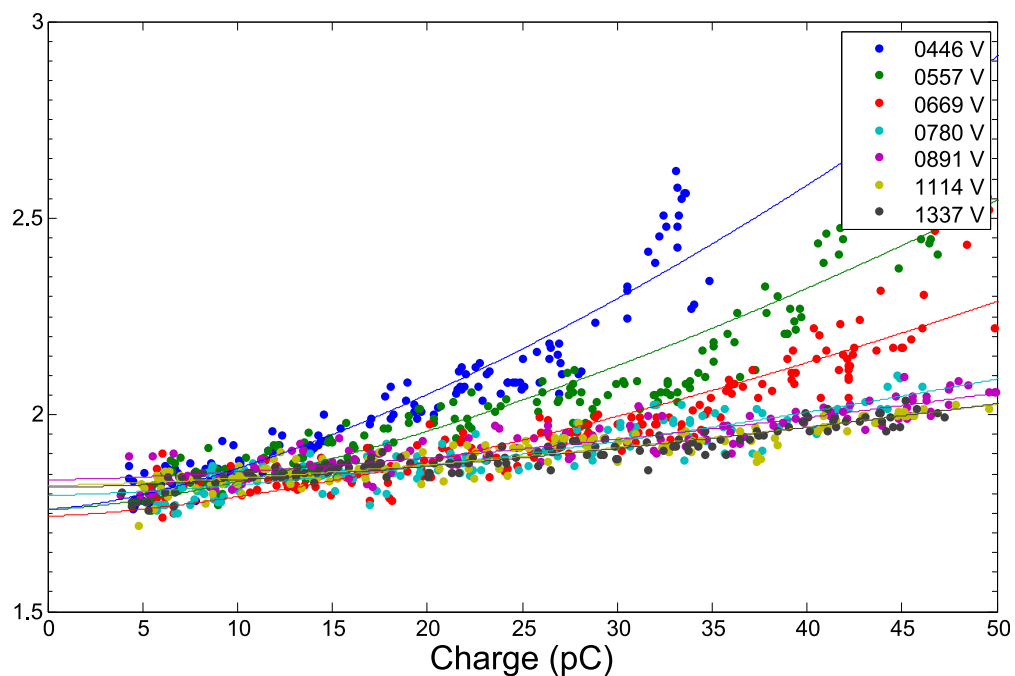


**Figure 4.16:** Charge dependence of the mobility of  $\text{Ba}^+$  in argon gas at a pressure of 620 Torr using a barium metal tip

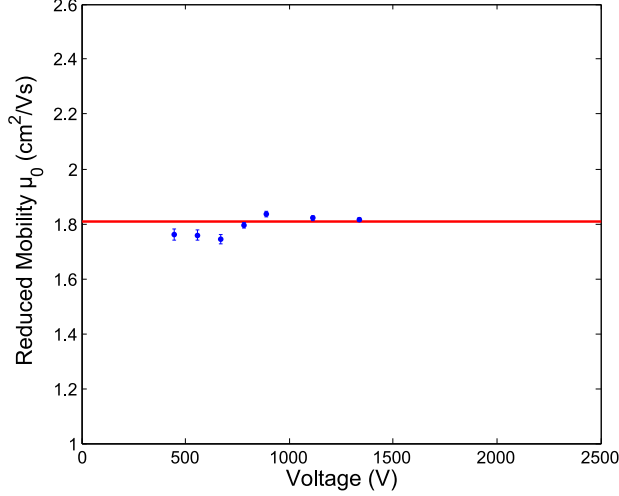


**Figure 4.17:** Intercept of the mobility as a function of voltage applied on the Target plate with argon gas pressure of 620 Torr using a barium metal tip.

The second ablation spot was 0.9 mm above the lower end of the tip. The calculated value for this position was  $d_{eff2}^2 = 2.24 \text{ cm}^2$ .

A plot of the mobility as a function of charge for these two ablation positions is shown in Figure 4.18. It is seen that the charge has more effect at higher positions, where the electric field near the tip is lower. The values of the intercepts are  $\mu_0 = 0.667 \pm 0.005 \text{ cm}^2/\text{Vs}$  when the metal tip is ablated at the low position, with  $d_{eff1}^2 = 1.84 \text{ cm}^2$ , and  $\mu_0 = 0.675 \pm 0.006 \text{ cm}^2/\text{Vs}$  when the ablation spot is high,  $d_{eff2}^2 = 2.24 \text{ cm}^2$ . Although the  $d_{eff}^2$  values were substantially different for these two ablation position, the true mobility values were almost identical within statistical uncertainties. These results may be used to asses the accuracy of SIMION calculations of  $d_{eff}^2$ . The largest uncertainty is in the location of the center of the spot from photographs to  $\pm 0.1 \text{ mm}$ . The systematic error in  $d_{eff}^2$  due to the spot position can then be estimated as  $\Delta d_{eff}^2 = \frac{0.1\text{mm}}{0.4\text{mm}}(2.24\text{cm}^2 - 1.84\text{cm}^2) = 0.10 \text{ cm}^2$ . Thus a systematic error limit for  $d_{eff}^2$  is set at  $\pm 0.10 \text{ cm}^2$  for experiments using the metal tip. In the case of the experiments with the getter, the uncertainty in the center of the spot is larger, about 0.5 mm because the ablation spot left on the getter is not as easy to distinguish as in the barium metal. Then, the systematic error is five times larger when the getter is used,  $\Delta d_{eff}^2 = 0.50 \text{ cm}^2$ .

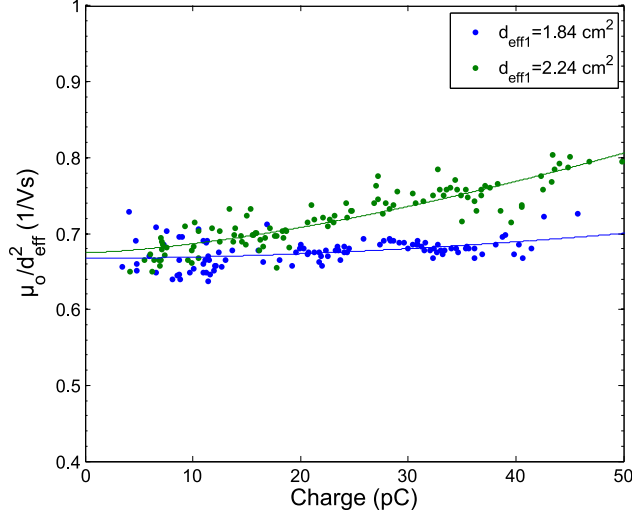


**Figure 4.18:** Plot of reduced mobility versus charge hitting two different positions on the barium metal tip.

## 4.2.2 Mobility Results

The mobility at different pressures was measured using the method described above except with fewer voltages. Some examples of the mobility measurements at different pressures are shown in Figure 4.19. The experiments were performed using a metal tip as ablation target, and  $d_{eff}^2 = 1.84 \text{ cm}^2$ . The plots of mobility versus charge were done at different voltages on the Target plate. The value of the mobility at each pressure was calculated by taking a weighted average of the intercept at different voltages.

The measured mobilities at different pressures of barium ions in xenon using a tilted barium metal tip are summarized and compared with predicted theoretical values in Table 4.3. Some samples of mobility measurements listed in Table 4.3 are shown in Figure 4.19. The reduced mobility of  $\text{Ba}^+$  in xenon is close to the theoretical value at low pressures, but at pressures higher than 600 Torr it decreases and differs from the predicted value by more than 20%.

The reduced mobility of  $\text{Ba}^+$  in argon gas was measured the same way, using a tilted barium metal tip. The measured reduced mobility for  $\text{Ba}^+$  in Ar gas at different pressures

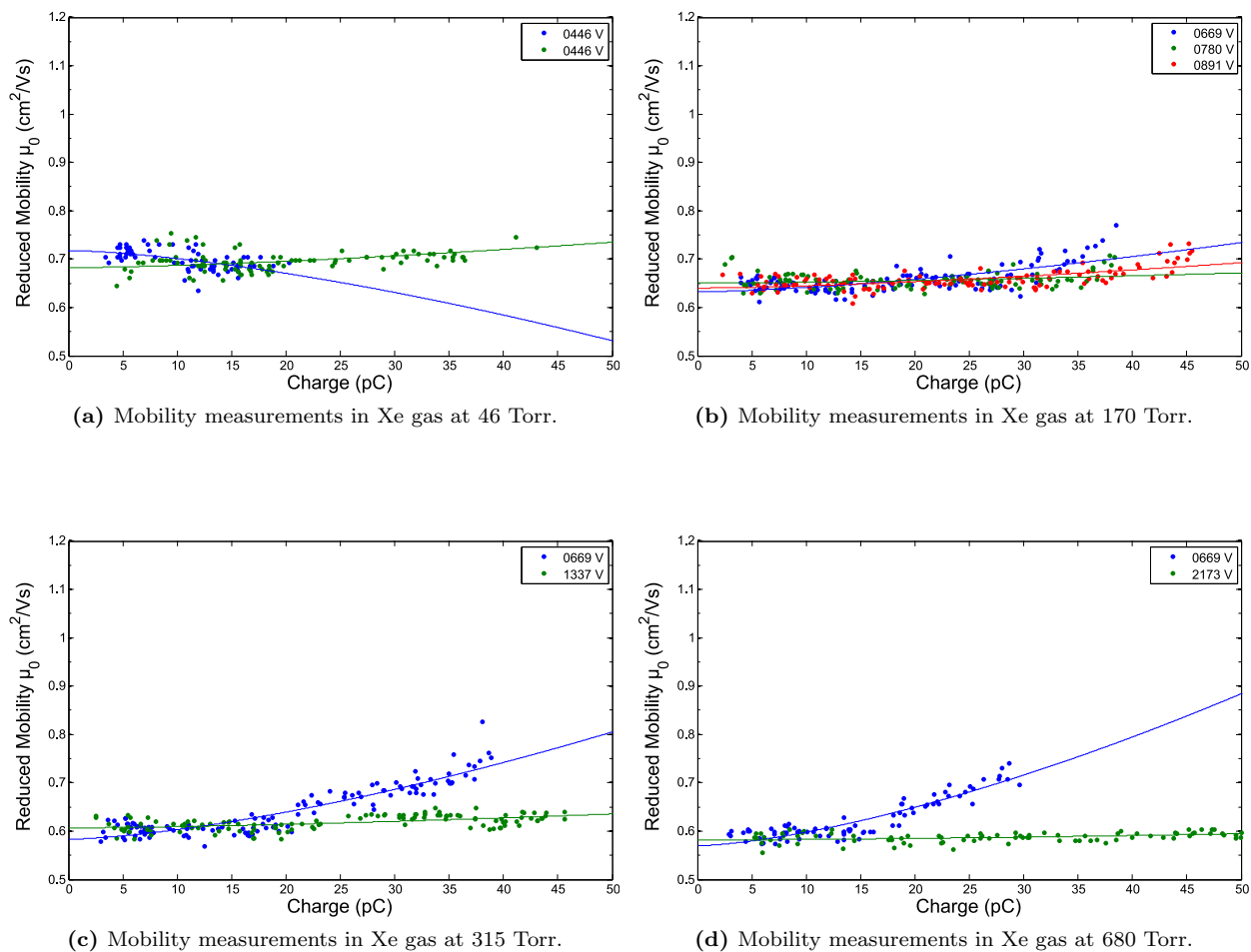


**Figure 4.19:** Sample of mobility measurements in xenon gas at different pressures using a tilted barium metal tip.

is listed at the end of Table 4.3. It is close to the predicted theoretical values and consistent within error limits of the previous measurements.

**Table 4.3:** Comparison of mobility measurements of  $\text{Ba}^+$  in xenon, and argon with predicted theoretical values. All of the measurements shown were done with a tilted barium metal tip. Errors shown for these results is statistical only.

Gas	Pressure (Torr)	Experimental $\mu_0$ ( $\text{cm}^2/\text{Vs}$ )	Theoretical $\mu_0$ ( $\text{cm}^2/\text{Vs}$ ) [33]	Previous results at 0.2 Torr $\mu_0$ ( $\text{cm}^2/\text{Vs}$ ) [41]
Xe	46	0.725 (0.018)	0.785	
Xe	46	0.697 (0.006)	0.785	
Xe	107	0.681 (0.004)	0.785	
Xe	110	0.652 (0.003)	0.785	
Xe	110	0.666 (0.005)	0.785	
Xe	110	0.654 (0.012)	0.785	
Xe	165	0.638 (0.011)	0.785	
Xe	170	0.641 (0.003)	0.785	
Xe	170	0.662 (0.003)	0.785	
Xe	315	0.599 (0.003)	0.785	
Xe	324	0.623 (0.014)	0.785	
Xe	344	0.603 (0.004)	0.785	
Xe	664	0.565 (0.003)	0.785	
Xe	665	0.600 (0.065)	0.785	
Xe	680	0.579 (0.003)	0.785	
Ar	87	1.726 (0.013)	1.88	1.80(0.16)
Ar	167	1.723 (0.020)	1.88	1.80(0.16)
Ar	332	1.716 (0.016)	1.88	1.80(0.16)
Ar	662	1.673 (0.027)	1.88	1.80(0.16)

### 4.2.3 Molecular Ion Formation

The variation of the measured mobility of  $\text{Ba}^+$  in xenon gas with pressure and the disagreement with the predicted theoretical values at high pressures suggest that there may

be more than one species of ions traveling through gas. As mentioned in the Chapter 2, termolecular association of  $\text{Ba}^+$  with two Xe atoms can form  $\text{BaXe}^+$ , and collisional dissociation can break up the molecular ions in collisions to atomic species. The apparent measured mobility is then an average of the mobility of the two different species weighted by the species fractions. The apparent mobility then can be written as follows:

$$\mu_{measured} = f_{(Ba^+)}\mu_{(Ba^+)} + f_{(BaXe^+)}\mu_{(BaXe^+)} \quad (4.4)$$

where  $f_{(Ba^+)}$  and  $f_{(BaXe^+)}$  are the percentages of the travel time that ions are  $\text{Ba}^+$  and  $\text{BaXe}^+$ , respectively, and  $\mu_{(Ba^+)}$  and  $\mu_{(BaXe^+)}$  are the mobilities  $\text{Ba}^+$  and  $\text{BaXe}^+$ , respectively. Using equation 2.39 which relates the percentage of  $\text{Ba}^+$  to the gas pressure  $p$ , and the fact that  $f_{(Ba^+)} + f_{(BaXe^+)} = 1$ , equation 4.4 can be written as

$$\mu_{measured} = \frac{1}{1 + bp}(\mu_{(Ba^+)} - \mu_{(BaXe^+)}) + \mu_{(BaXe^+)}, \quad (4.5)$$

where  $b$  is a constant defined in (2.40) that depends on the the ratio of the association to the dissociation rate constants, and  $p$  is the gas pressure in Torr.

A plot of mobility versus pressure is shown in Figure 4.20. Because all measurements were made with the same ablation spot position, the common systematic error in  $d_{eff}^2$  due to ablation spot position is omitted from this graph. The model fits the data well. The fit value of  $b$  is  $0.0039(7) \text{ Torr}^{-1}$ . The reduced mobility of  $\text{Ba}^+$  in xenon gas obtained from the fit is  $\mu_{0Ba^+} = 0.734 \pm 0.010(\text{stat}) \pm 0.040(\text{syst}) \text{ cm}^2/\text{Vs}$ . The statistical errors in these fits are 1 sigma values. The systematic error in  $\mu_{0Ba^+}$  is calculated using  $\Delta\mu_{syst} = \mu(\Delta d_{eff}^2)_{syst}/d_{eff}^2$ . This result is within the error limit to the theoretical value of  $0.784 \text{ cm}^2/\text{Vs}$ . The value of the mobility of  $\text{BaXe}^+$  in xenon calculated from the fit is  $\mu_{0BaXe^+} = 0.508 \pm 0.010(\text{stat}) \pm 0.028(\text{syst}) \text{ cm}^2/\text{Vs}$ . There is no reported theoretical mobility of  $\text{BaXe}^+$  in xenon gas to compare to. Since the molecular ion is larger than the atomic ion, it might be expected to have lower mobility.

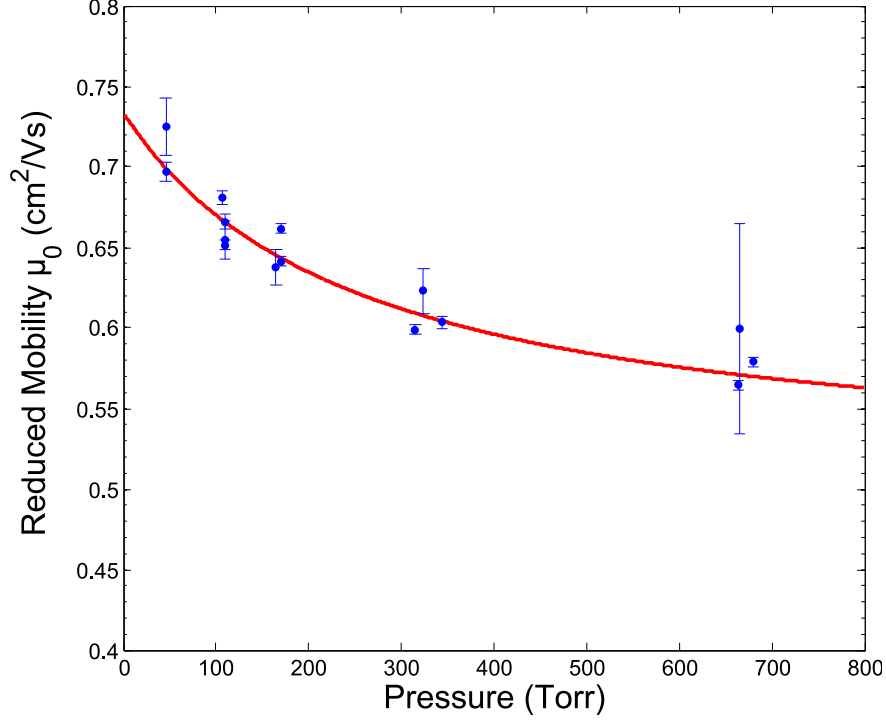


**Figure 4.20:** Reduced mobility in xenon gas as a function of pressure. Errors shown are statistical only, as common ablation spot was used.

An additional systematic error from the position of the ablation spot due to the variation in the laser position. The beam position is stable and fluctuations in position might be as large as a few percent. This variation produces a systematic error of  $\Delta d_{eff}^2 = 0.02 \text{ cm}^2$ , which is about 1% of  $d_{eff}^2 = 1.84 \text{ cm}^2$ . This systematic error can be added in quadrature to the statistical error of the individual measurements of the mobilities at different pressures. Figure 4.21 shows the a fit of mobility versus pressure and the percentage of  $\text{Ba}^+$  and  $\text{BaXe}^+$  ions as a function of pressure when 1% systematic error in  $d_{eff}^2$  is used. The values obtained from this fit are  $b = 0.0043(15) \text{ Torr}^{-1}$ ,  $\mu_{0\text{Ba}^+} = 0.739 \pm 0.018(\text{stat}) \pm 0.040(\text{syst}) \text{ cm}^2/\text{Vs}$ , and  $\mu_{0\text{BaXe}^+} = 0.513 \pm 0.019(\text{stat}) \pm 0.028(\text{syst}) \text{ cm}^2/\text{Vs}$ . This results are comparable to those obtained using only statistical errors.

The percentage of  $\text{Ba}^+$  ions as a function of pressure is calculated as

$$\frac{[\text{Ba}^+]}{[\text{Ba}^+] + [\text{BaXe}^+]} = \frac{1}{1 + bp} \quad (4.6)$$

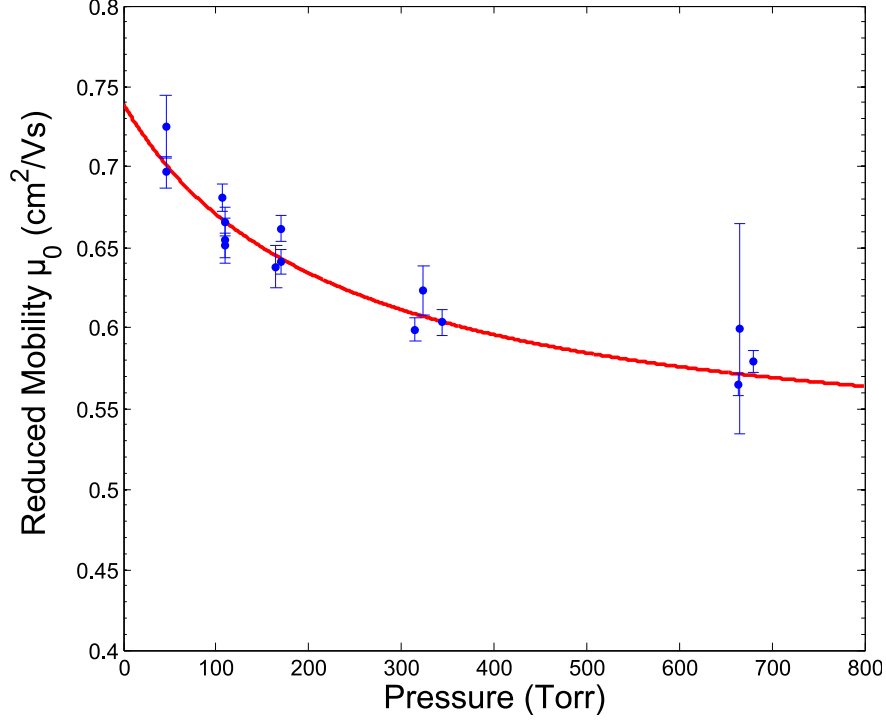


**Figure 4.21:** Reduced mobility in xenon gas as a function of pressure. Errors shown are the sum of statistical and 1% systematic error.

Using the derived  $b$ , the extracted percentage of  $\text{Ba}^+$  is shown in Figure 4.22. At a pressure of 1 atmosphere the percentage of  $\text{Ba}^+$  is about 25%. Figure 4.23 shows the percentage of  $\text{Ba}^+$  and  $\text{BaXe}^+$  ions as a function of pressure when 1% systematic error in  $d_{eff}^2$  is used.

The ratio of the association rate constant to the dissociation rate constant  $k_{assoc}/k_{dissoc}$  can be calculated from the value of the constant  $b$  with

$$b = \frac{k_{assoc}}{k_{dissoc}} \left( \frac{2.69 \times 10^{19} \text{cm}^{-3}}{760 \text{Torr}} \right) \left( \frac{273.15 \text{K}}{T} \right) \quad (4.7)$$

The result is  $k_{assoc}/k_{dissoc} = 1.3(0.4) \times 10^{-19} \text{cm}^3$ , using  $b = 0.0043(15) \text{Torr}^{-1}$ . For comparison, using estimated values of the association and dissociation rate constants of  $k_{assoc} = 10^{-31} \text{cm}^6/\text{s}$  and  $k_{dissoc} = 6.1 \times 10^{-13} \text{cm}^3/\text{s}$  given in Table 2.4, a ratio of  $k_{assoc}/k_{dissoc} = 1.6 \times 10^{-19} \text{cm}^3$  is obtained. The rough order of magnitude estimate agrees remarkably well with the experimental ratio.

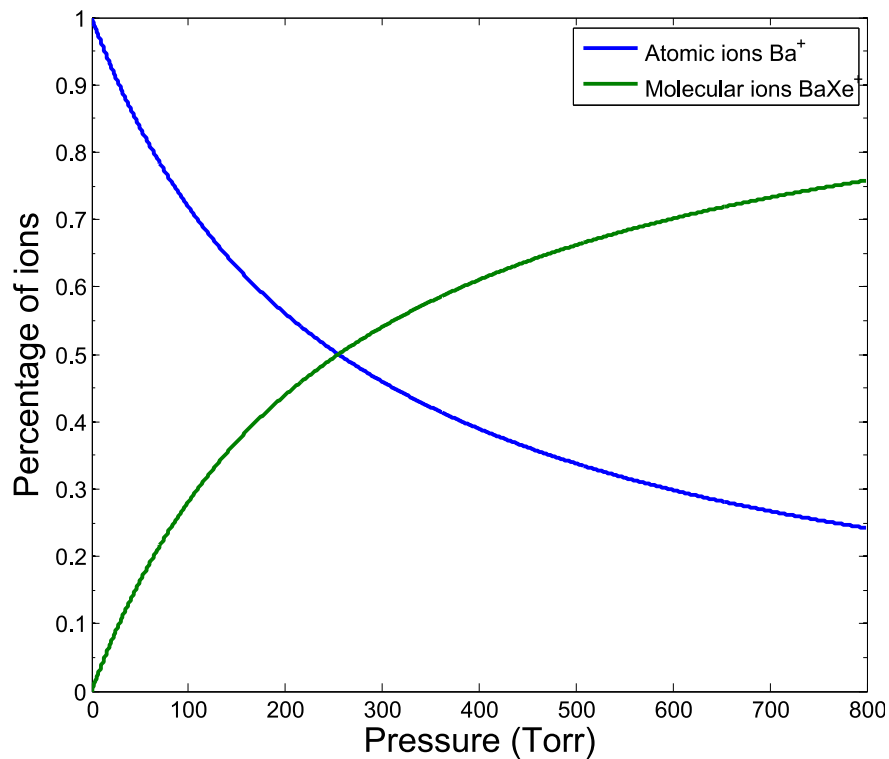


**Figure 4.22:** Percentage of Ba<sup>+</sup> and BaXe<sup>+</sup> ions in xenon gas as a function of xenon pressure.

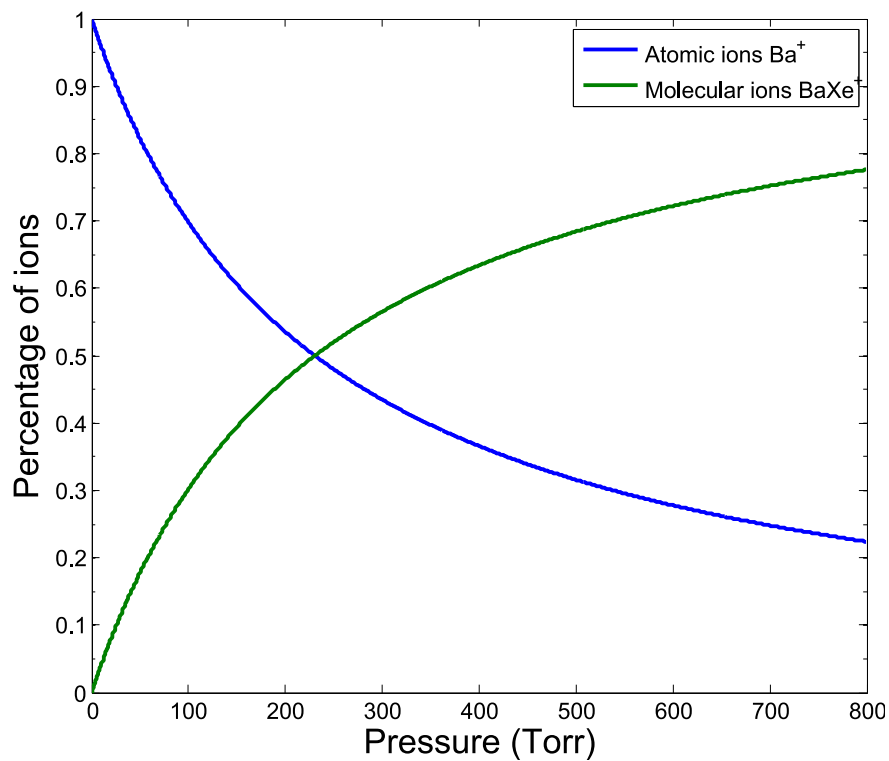


**Figure 4.23:** Percentage of Ba<sup>+</sup> and BaXe<sup>+</sup> ions in xenon gas as a function of xenon pressure when 1% systematic error is used in the fit of mobility versus pressure.

Measurements of the mobility of barium ions in argon gas at different pressures are shown in Figure 4.24. There is much less variation of the mobility with pressure in argon than in xenon. In the case of  $\text{Ba}^+$  in argon gas, the estimated ratio of the association to the dissociation rate constant, using the values from Table 2.4, is  $k_{\text{assoc}}/k_{\text{dissoc}} = 2 \times 10^{-21} \text{ cm}^3$ . The estimated ratio is 2 orders of magnitude smaller for argon gas than for xenon gas. The consequence of the ratio being smaller in argon gas is that even at 1 atmosphere, the mobility is expected to remain about almost constant since the percentage of molecular ions is small in the pressure range from 0 to 700 Torr of pressure.

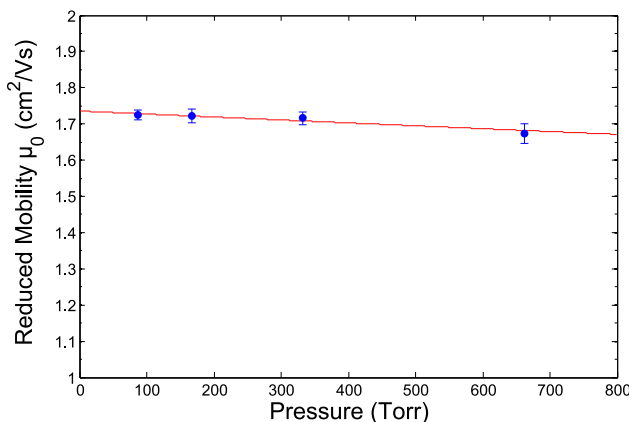


**Figure 4.24:** Reduced mobility in argon gas as a function of pressure with the percentage of atomic ions denoted for each pressure.

The mobility of barium ions in argon at zero pressure found from the fit is  $\mu_{\text{Ba}^+} = 1.736 \pm 0.028(\text{stat}) \pm 0.094(\text{syst}) \text{ cm}^2/\text{Vs}$ . The measured mobility of  $\text{Ba}^+$  in argon gas at zero pressure is about 1.2 error limit below the predicted value,  $1.88 \text{ cm}^2/\text{Vs}$ , [33] and are consistent with a previous measurement,  $1.80(16) \text{ cm}^2/\text{Vs}$ , [41], within error limits.

### 4.3 Fluorescence Experiments

In this section, results from the fluorescence of  $\text{Ba}^+$  ions in xenon gas are presented. The fluorescence of  $\text{Ba}^+$  ions in vacuum is well known. When  $\text{Ba}^+$  ions are surrounded by xenon gas, the excitation spectrum broadens as the pressure increases. Measurements of the linewidth of the excitation spectrum in the pressure range of 40 to 200 Torr are presented

in section 4.3.2. The fluorescence count rate per ion as a function of pressure is discussed in section 4.3.3. A model that includes nonradiative decays is discussed, and limits on nonradiative decay rates are estimated using the model.

### 4.3.1 Fluorescence Spectra

The barium ions are excited from the ground state,  $6s\ ^2S_{1/2}$  to the excited state  $6p\ ^2P_{1/2}$  with the use of a tunable dye laser. The ions can decay back to the ground state emitting 493.4 nm light or to the metastable state  $5d\ ^2D_{3/2}$  emitting 649.7 nm light. In this experiment, fluorescence is detected at 649.7 nm wavelength so that the scattered light from the excitation laser can be blocked with a Raman filter. In vacuum the  $\text{Ba}^+$  ions decay about one fourth of the time to the metastable state  $5d\ ^2D_{3/2}$ . In order to measure the pressure broadening of this transition, the dye laser is scanned around the resonant wavelength in vacuum, which is 493.4 nm. In analyzing the results, the buildup of population in the metastable state must be taken into account.

There are two backgrounds that must be subtracted from the fluorescence spectra. One is the background from scattered light produced by the excitation laser when it goes through the system. A spectrum is shown in Figure 4.25. This background spectrum is almost flat at the fluorescence wavelength. The other source of background comes from the scattered emission light from the plasma due to the laser ablation. Even though the ablation and the excitation of the ions with the dye laser occur at different times, the CCD camera is not fast enough to differentiate these two events since it takes about 0.25 seconds to process information in between frames, and the drift time of the ions in xenon gas in the range of pressures at which the experiments were performed is on the order of a few milliseconds.

A plasma emission spectra taken by imaging the ablation spot is shown in Figure 4.26. Most of the largest peaks correspond to  $\text{Ba}^+$  emission lines, which are labeled in the figure. The rest of the major peaks correspond to  $\text{Ba}^+$  and Ba neutral transitions. The integrated

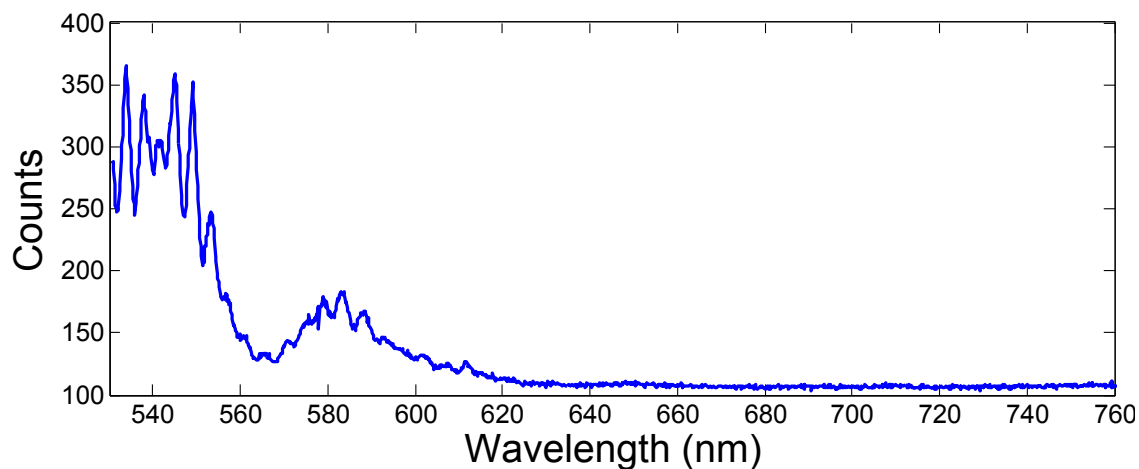


**Figure 4.25:** Background scattered light from dye laser laser going through the system.

plasma emission depends on the amount of charge created during ablation; the larger the charge, the larger the total plasma emission, as can be seen in Figure 4.27.

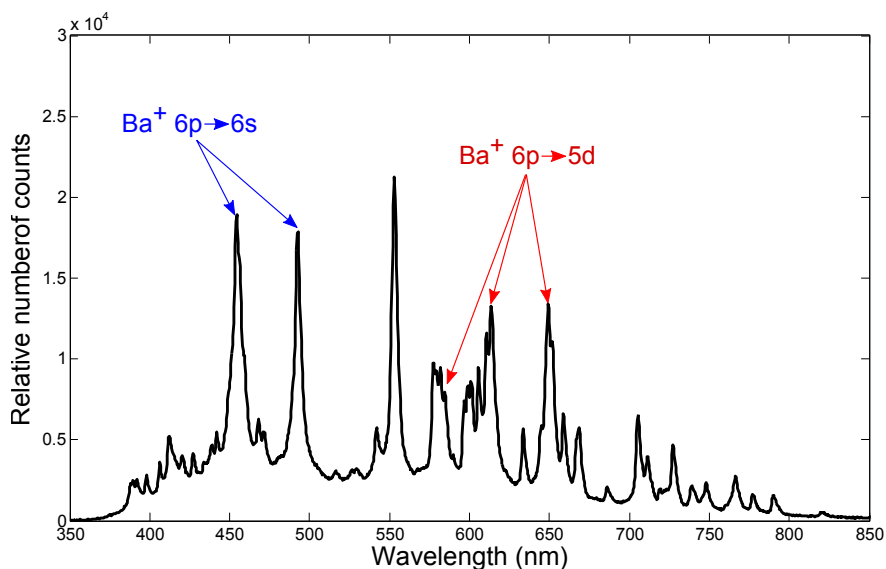


**Figure 4.26:** Plasma Spectra.

The amount of scattered plasma light collected is much less than the light collected by directly imaging the plasma since the scattered plasma light is mostly out of the field of view and out of focus in the configuration for fluorescence collection. The background due to the plasma emission can be reduced by decreasing the charge created during ablation; however, the fluorescence signal also decreases since it is proportional to the charge. Sample background signals with different average charge per shot are shown in Figure 4.28. Each

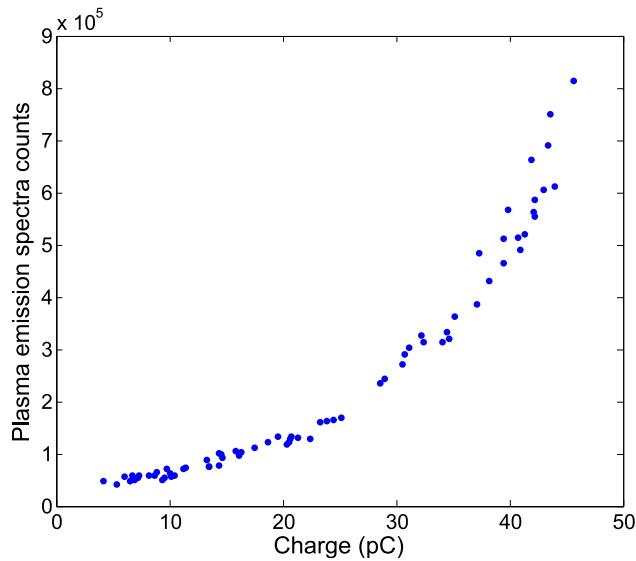


**Figure 4.27:** Plasma counts of the 650 nm peak versus ion charge.

frame includes the signal from 5 ablation shots in each frame to get higher signal to noise ratio. Since plasma background increases greater than linearly with the charge, using a lower charge gives a higher fluorescence to background ratio. By trying different average charge per shot it was determined that ablation shots creating an average charge between 1 and 5 pC generate a background low enough to separate the fluorescence signal from the scattered emission light of the plasma.

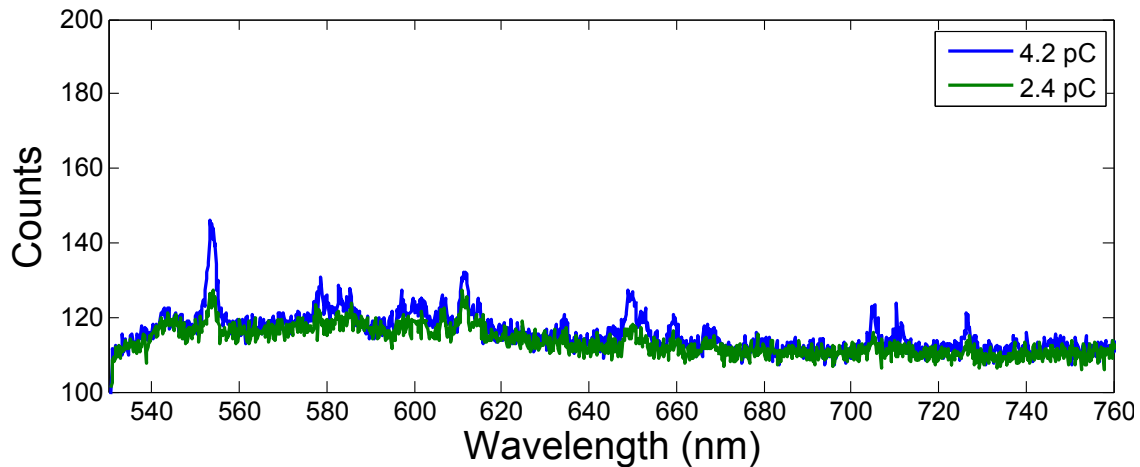


**Figure 4.28:** Background spectrum from scattered ablation light.

Figure 4.29 shows an example of fluorescence signal after the backgrounds are subtracted. The fluorescence spectrum is narrower than the background from the scattered light of the

ablation plasma, which also helps to distinguish it from the background. The fluorescence signal is fitted to a gaussian, and the total fluorescence counts are calculated by taking the integral of the gaussian fit. A slit size of  $150 \mu\text{m}$  is wide enough to pass all of the fluorescence light while maintaining good spectral resolution.

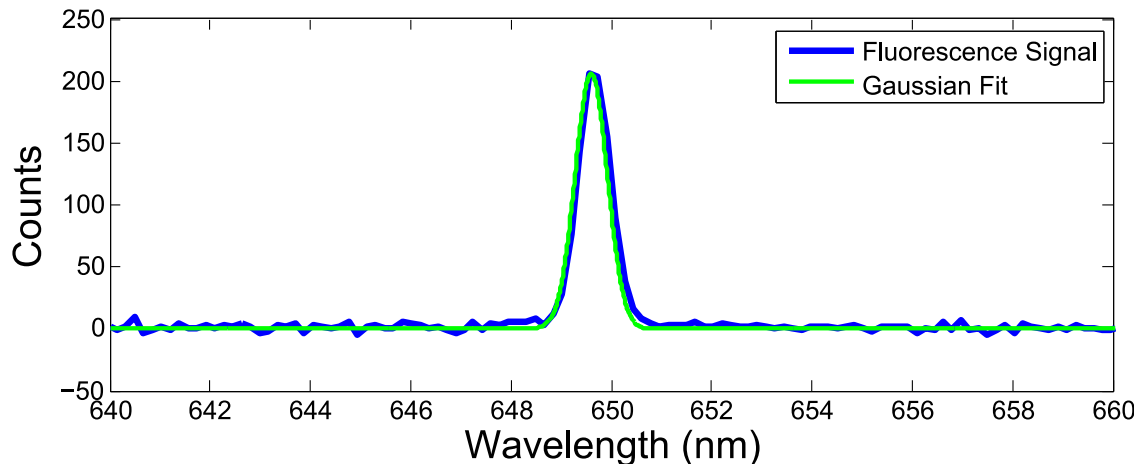


**Figure 4.29:** Background subtracted fluorescence spectrum of  $\text{Ba}^+$  in xenon gas from the transition ( $6p \ ^2P_{1/2} - 5d \ ^2D_{3/2}$ ) with excitation at 493.4 nm. The average charge per shot is 3 pC and the xenon gas pressure is 55 Torr.

### 4.3.2 Pressure Broadening

The excitation spectrum of  $\text{Ba}^+$  in xenon gas at different pressures was measured by scanning the dye laser frequency between  $20261.20 \text{ cm}^{-1}$  and  $20262.00 \text{ cm}^{-1}$ . The resonant frequency of the transition ( $6s \ ^2S_{1/2} - 6p \ ^2P_{1/2}$ ) in vacuum is  $20261.56 \text{ cm}^{-1}$ . The change in frequency during the scans was measured by determining the shift in the fringe pattern in the spectrum analyzer. Two spectrum analyzer transmission curves are shown in Figure 4.30. The blue signal corresponds to the initial frequency spectrum, and the green signal correspond to the frequency spectrum after shifting the frequency of the dye laser by  $0.034 \text{ cm}^{-1}$ . The peaks were fit to gaussians in order to calculate the shift of the peaks relative to the mode spacing.

To measure the fluorescence signal of  $\text{Ba}^+$  ions at a specific wavelength, the dye laser was set at the desired frequency. Then the ablation laser was triggered at a frequency rate

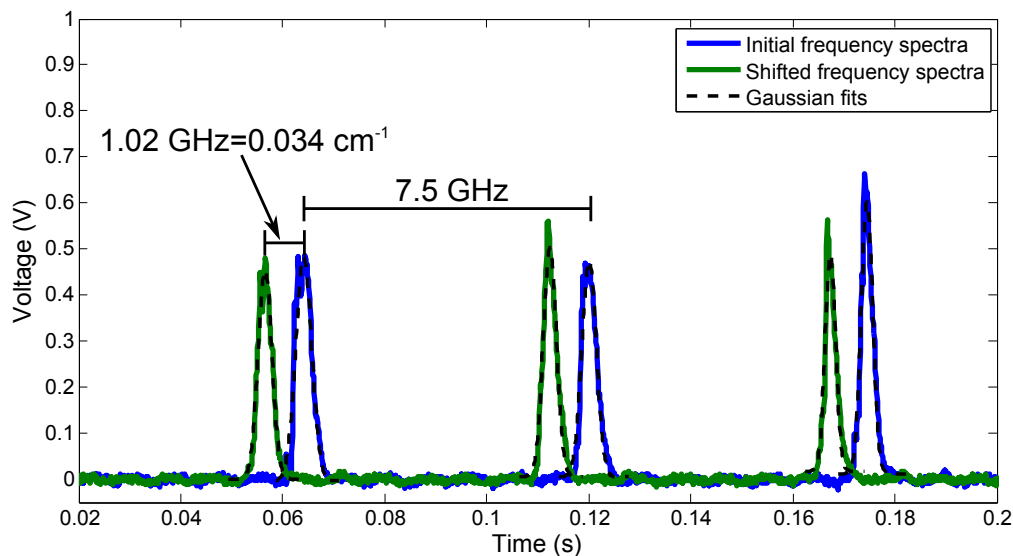


**Figure 4.30:** Shift in laser frequency detected by spectrum analyzer.

of 2.5 Hz; the ions produced by laser ablation drifted to the excitation laser and then to the Grid 1 plate, where the ion current was detected. As the ions passed through the excitation laser they fluoresced, and the emitted fluorescence light at 650 nm was measured through the spectrometer on the CCD chip. The shutter of the CCD camera was open for 2 seconds; thus one frame included the fluorescence signal from five  $\text{Ba}^+$  ion clouds. Five frames were taken for each wavelength. Fluorescence signals in the five frames were averaged as well as the current signals from the ions. The laser power was measured during each frame and then averaged. One data point in a pressure broadened spectrum is the averaged fluorescence signal at that particular laser wavelength. An attempt was made to keep the total ion charge constant through the whole scan of the dye laser frequencies, but there were variations. The laser power also varied as the laser was scanned. In order to correct for these two variations, the total number of fluorescence counts was divided by the average charge and the average laser power for each measurement.

The broadening of the excitation spectra is a combination of pressure and Doppler broadening. The line shape due to the Doppler broadening is a Gaussian profile and its full width

at half maximum (FWHM) is given by

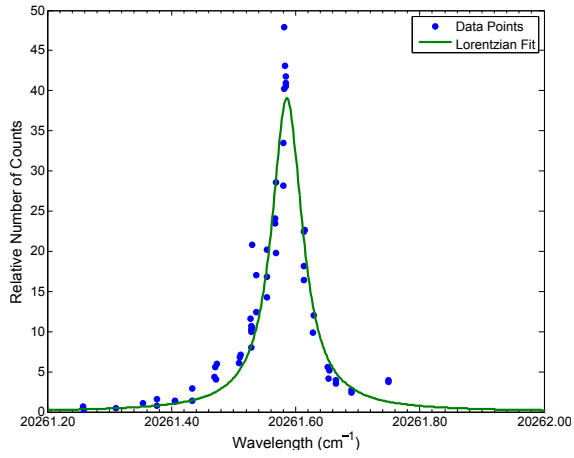
$$\Delta\nu_D = 2\nu_0 \left( \frac{2kT \ln 2}{Mc^2} \right)^{1/2} \quad (4.8)$$

The temperature of the xenon gas during the experiment was 296 K,  $M$  is the mass of a barium ion and  $\nu_0$  is the resonant frequency of the transition ( $6s\ ^2S_{1/2} - 6p\ ^2P_{1/2}$ ) in vacuum. Using these numbers, the Doppler width is  $\Delta\nu_D = 639$  MHz or  $\Delta\nu_D = 0.0213$  cm<sup>-1</sup>. At relatively high pressures, higher than 100 Torr, the broadening due to the gas pressure is expected to dominate, since typical values for pressure broadening are around 10 to 20 MHz/Torr. At pressures around 100 Torr, the pressure broadening will be comparable to the Doppler broadening. As discussed in Chapter 2, when the pressure broadening dominates, the excitation spectrum has a Lorentzian line shape. At the pressures used in this work, the line shape is a Voigt profile, which is a combination of a Gaussian and a Lorentzian distribution. However, to simplify the analysis, experimental spectra were fit to a Lorentzian function and a correction for the Voigt profile was made later. The Lorentzian function is of the form

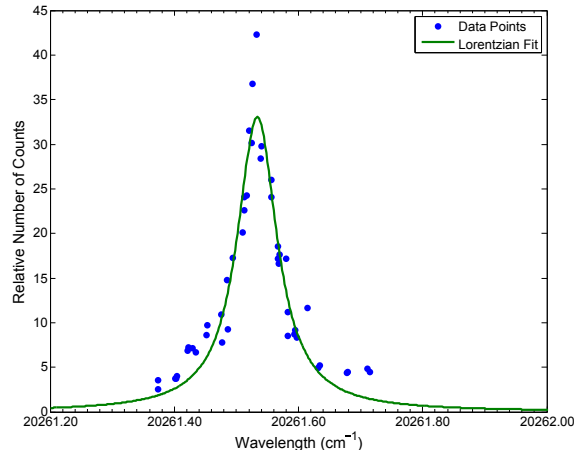
$$g(\nu) = \frac{C(\Delta\nu/2)^2}{(\nu_0 - \nu)^2 + (\Delta\nu/2)^2} \quad (4.9)$$

where  $C$  is the amplitude of the Lorentzian, and  $\Delta\nu$  is the FWHM of the Lorentzian.

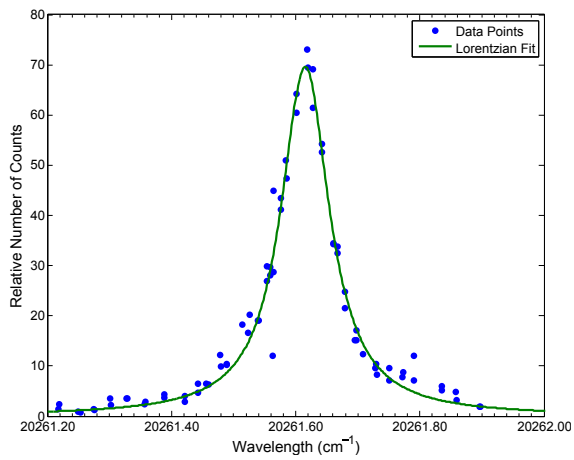
Some plots of the excitation spectra and their fit are shown in Figure 4.31. It can be seen that the peak broadens as the pressure increases. The raw FWHM of the excitation spectra is plotted as a function of pressure in Figure 4.32. The  $y$  intercept of a linear fit to the data should be roughly the Doppler broadening, since it will be the dominant broadening mechanism when the pressure approaches zero. The value of the intercept obtained from the fit is  $1230 \pm 190$  MHz. This value is twice as large the estimated value using equation 4.8. This discrepancy can be explained because this model does not take optical pumping into account. At the peak of the excitation spectra the cross section is higher, which translates in



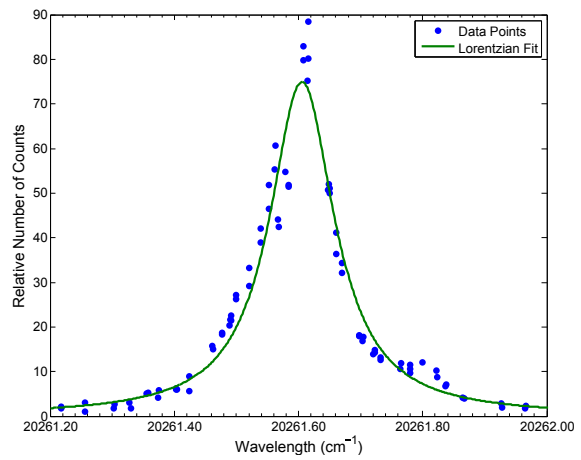
(a) Excitation spectrum at 40 Torr



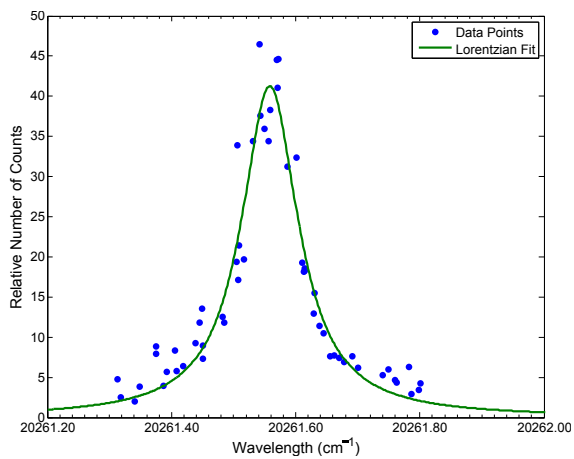
(b) Excitation spectrum at 55 Torr



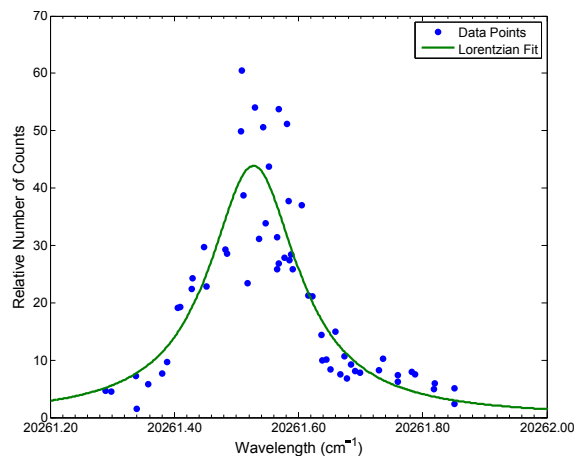
(c) Excitation spectrum at 100 Torr



(d) Excitation spectrum at 125 Torr



(e) Excitation spectrum at 150 Torr



(f) Excitation spectrum at 200 Torr

**Figure 4.31:** Excitation spectra of  $\text{Ba}^+$  in xenon gas at different pressures

a higher excitation rate and thus more optical pumping. At the wings of excitation spectra the cross section is smaller; thus there is less optical pumping. The net effect of optical pumping is that the width of the Lorentzian fit to the raw data is wider than the width of the actual excitation spectrum since near the peak there is more loss of fluorescence due to optical pumping than in the wings.

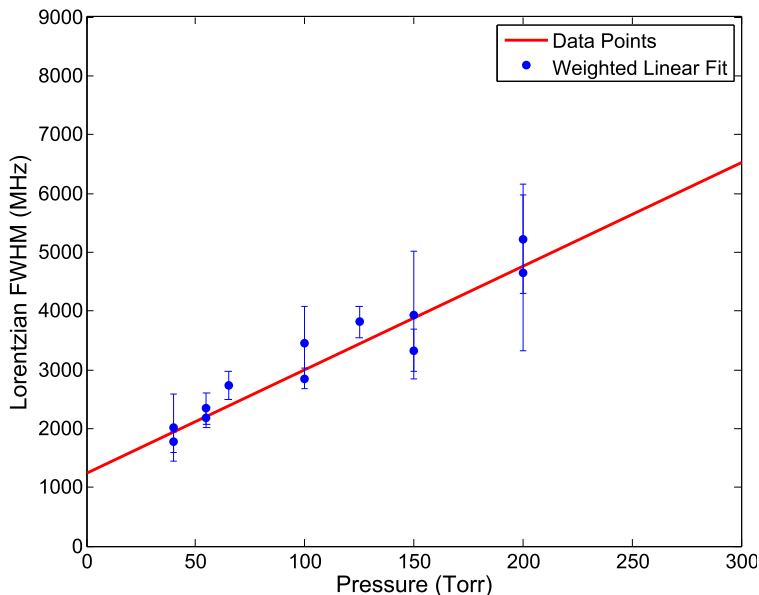


**Figure 4.32:** Pressure broadening of the uncorrected excitation spectra of  $\text{Ba}^+$  in xenon gas.

The number of counts as a function of laser power can be predicted using the model described below in section 4.3.3. Figure 4.33 shows a plot of predicted number of counts on resonance versus laser power  $P$  for different pressures. The cross sections used were those determined from the raw spectral widths of the fits in Figure 4.32. If there were no optical pumping, the plot of counts versus laser power would be a straight line. From the bending of the curves, it is observed that there is significant optical pumping. The number of counts versus laser power is fit to a function of the form  $y = m_1 P / (1 + P/m_2)$ .

The correction factor, i. e., the factor by which the fluorescence on resonance is reduced by optical pumping, is  $\frac{m_1}{m_1/(1+P/m_2)}$ . This is calculated for some laser powers and the plotted versus relative signal  $y$ , a normalized value from the  $y$  axis of the Figure 4.33. Figure 4.34 shows fits of the correction factor as a function of relative signal for different pressures. The

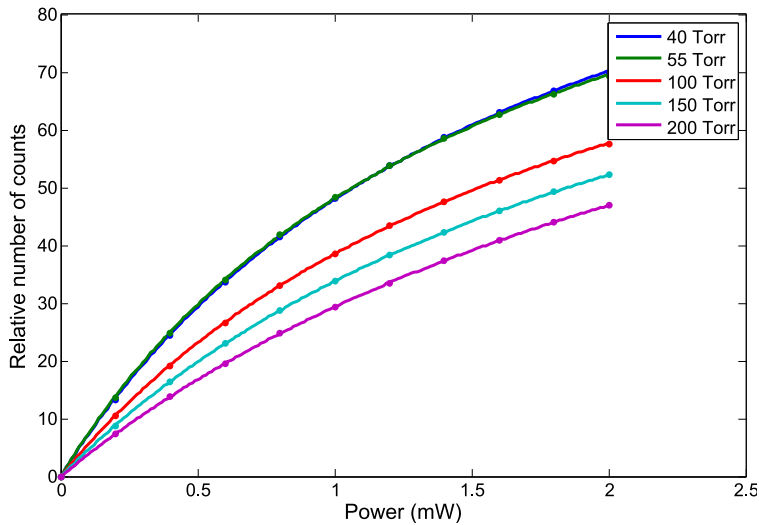


**Figure 4.33:** Predicted number of counts versus laser power.

resulting curve is fitted to a polynomial of order 3 of the form  $a_0 + a_1y + a_2y^2 + a_3y^3$ . Since a reduction in laser power is equivalent to corresponding reduction in cross section when the frequency is off resonance, this polynomial fit can be used to correct the counts from the raw excitation spectra. The correction is expected to be small at low relative signal (far off resonance), and larger at high relative signal (near resonance). The data in Figure 4.33 and 4.34 represents the corrections for the first iteration step in optical pumping corrections.

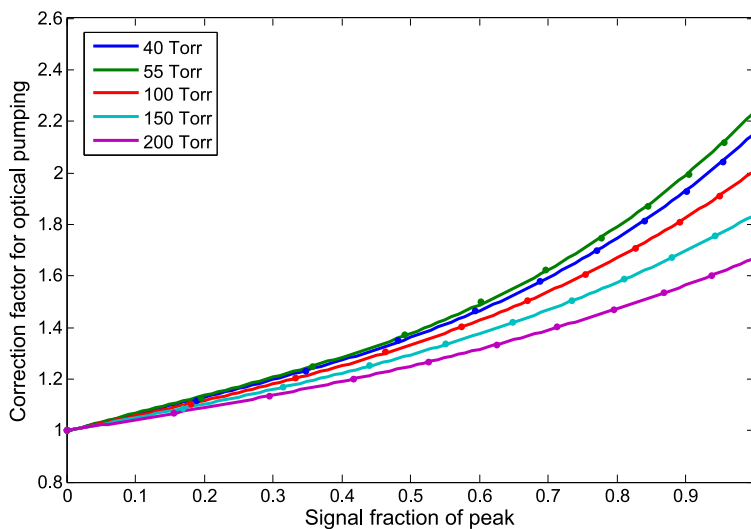


**Figure 4.34:** Correction factor versus relative signal.

The correction factor for each frequency  $\nu$  was obtained by evaluating the cubic fit equation at the relative signal obtained from the normalized Lorentzian fit to uncorrected spectrum at frequency  $\nu$ . Each data point from the uncorrected spectrum is multiplied by the corresponding correction factor, and then the corrected data points are obtained. A plot comparing the fit of an uncorrected excitation spectrum at 40 Torr with a fit from a corrected excitation spectrum is shown in Figure 4.35. The data points near the peak have a larger correction factor, while the points at the wings have a smaller correction factor. Therefore, the corrected spectrum has a higher peak and is narrower. It represents a first guess at the signal that would have been obtained had there been no optical pumping.

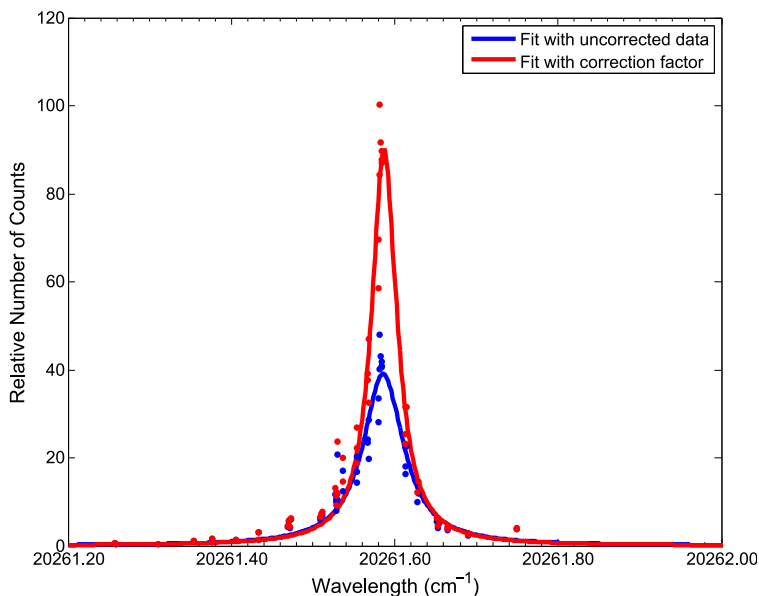


**Figure 4.35:** Comparison of an uncorrected excitation spectrum with the first iteration corrected spectrum at 40 Torr.

The cross sections used for the first estimates of optical pumping corrections were based on raw spectral widths and therefore were not quite correct. Thus the process must be iterated until the correct widths without optical pumping are obtained. For the next iterations, the corrected spectra spectra are fit again to a Lorentzian. Since the corrected spectra are narrower, the new calculated cross sections are higher, which in turns affects the predicted number of counts. Figures 4.34 and 4.35 are recalculated using the new correction factors obtained from the predicted number of counts calculated with the new cross sections. This

process was iterated four times. The corrected spectrum at 55 Torr for five iterations is shown in Figure 4.36. After the first correction, the width of the spectrum decreases by

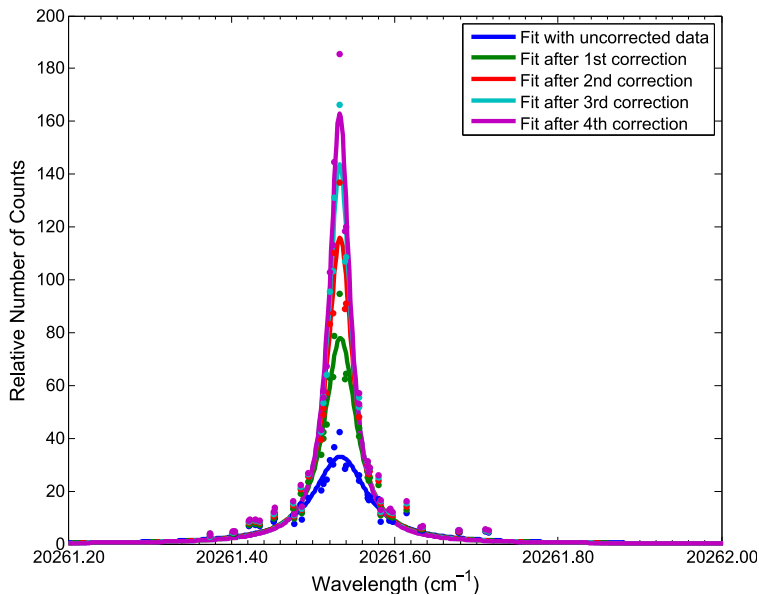


**Figure 4.36:** Corrected excitation spectra at 55 Torr for five iterations.

about a factor of two. Subsequent iterations continue to reduce the width but by a smaller factor. The difference in the width between the third and fourth correction is less than 10%.

A plot of the cross section versus iteration number is shown in Figure 4.37. It can be seen that after 5 iterations the cross section value still does not converge, specially for high pressures, meaning that more iterations are needed. The cross section versus iteration number is fit to a function of the form  $m_1 - m_2 \exp(-x/m_3)$ . The value of the cross section extrapolated to an infinite number of iterations is equal to the parameter  $m_1$  obtained from the fit.

It is expected that the values of sigma do not change with subsequent iterations after the excitation spectra are corrected with the extrapolated cross sections. In order to check if the cross section values converge, two more iterations to correct the excitation spectra were done. Figure 4.38 shows the cross section after using the extrapolation to infinite number of iterations. The first value of the cross section is the value after the extrapolation, and the next two are values after subsequent iterations. For low pressures the cross section stays

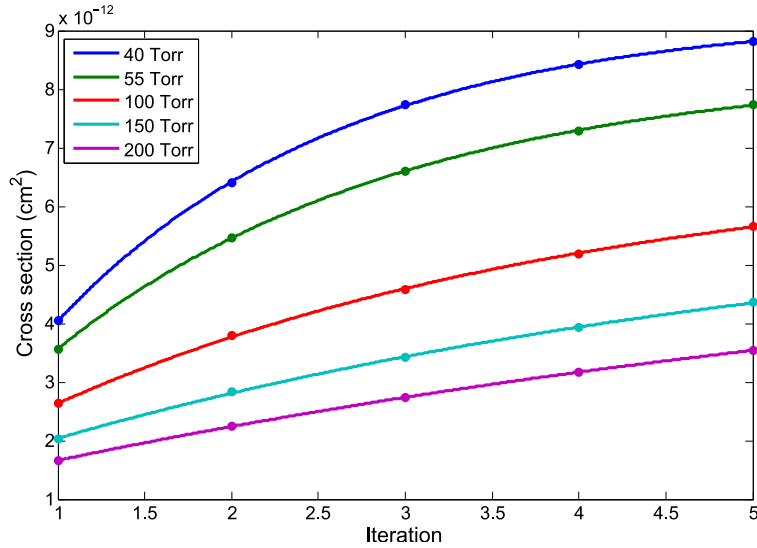


**Figure 4.37:** Calculated cross section versus number of iterative corrections.

about the same after the extrapolation; at 150 and 200 Torr the cross section decreases after the first iteration but for the second iteration the variation is less. This means that the extrapolation gave a good correction factor for low pressures but over corrected the cross section values for high pressures.

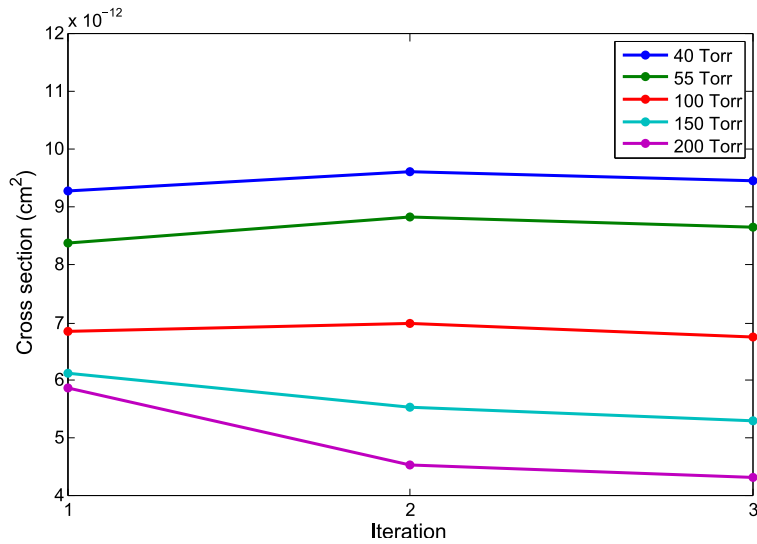


**Figure 4.38:** Calculated cross section after extrapolating to infinite number of iterations.

After this work errors in the ion interaction time  $\Delta t$  and the in value of  $\sigma_0$  were discovered. The correction was iterated two more times with the correct  $\Delta t$  and  $\sigma_0$  to find the corrected widths of the spectra and the cross sections. Figure 4.39 shows the calculated cross sections

for different pressures for 2 iterations. The last cross section is an extrapolation using an exponential to find the best estimate. The final corrected widths of the spectra are plotted versus xenon pressure in Figure 4.40. It can be seen that the correct widths are a factor of 2-3 less than the raw widths in Figure 4.32.

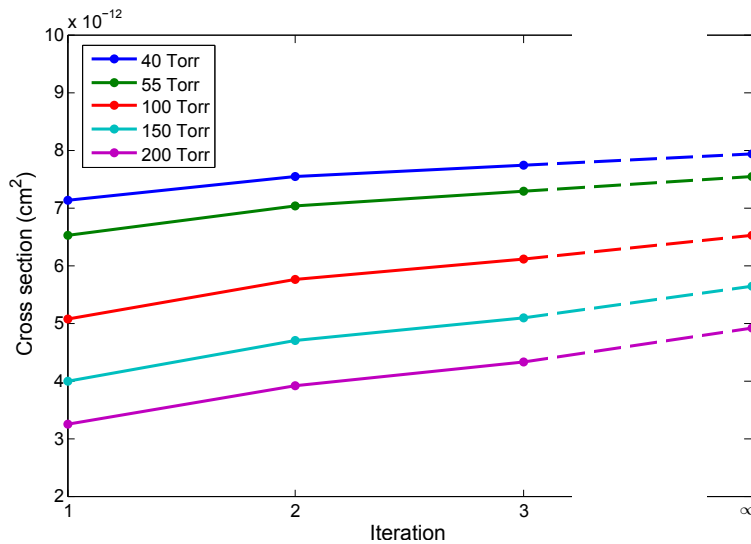


**Figure 4.39:** Calculated cross section using the correct interaction time and  $\sigma_0$ .

To determine the pressure broadening coefficients, corrections for the Gaussian component in the Voigt profile and the effect of using a Lorentzian fit must be accounted for. A fairly accurate simple expression relates the Voigt width  $\Delta\nu_V$  to the Gaussian width  $\Delta\nu_G$  and the Lorentzian width  $\Delta\nu_L$  as [42]

$$\Delta\nu_V \approx 0.5346\Delta\nu_L + \sqrt{0.2166(\Delta\nu_L)^2 + \Delta\nu_G} \quad (4.10)$$

Since the natural linewidth is negligible the pressure broadening width can be written as  $\Delta\nu_L = Cp$  where  $C$  is the pressure broadening coefficient in MHz/Torr, and  $p$  is the gas pressure. Then equation 4.10 is

$$\Delta\nu_V \approx 0.5346Cp + \sqrt{0.2166(Cp)^2 + \Delta\nu_G} \quad (4.11)$$

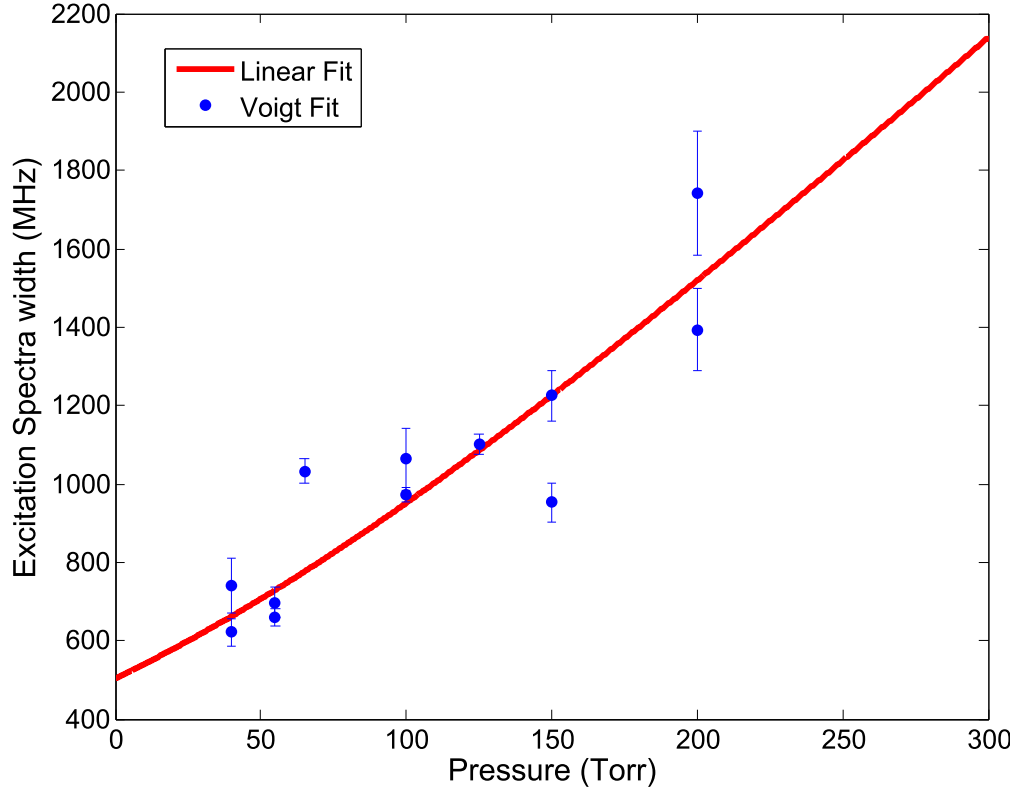


**Figure 4.40:** Final corrected excitation spectra width versus xenon pressure.

Since the excitation spectra are fit to a Lorentzian, the value of the Doppler width in equation 4.11 may need to be adjusted since a Lorentzian function does not fit a Gaussian very well. A pure Gaussian with FWHM of 639 MHz fit to a Lorentzian is shown in Figure 4.41. The Lorentzian fit has a width 503 MHz. This value used as the Doppler width  $\Delta\nu_G$  in the Voigt approximation in equation 4.11 will give the correct limit at low pressure in equation 4.11.

In order to verify that using  $\Delta\nu_G = 503$  MHz equation 4.11 is correct for higher pressures, a pseudo-Voigt function [43] that has a Gaussian width of 639 MHz and Lorentzian widths varying 50-10000 MHz is fit to a Lorentzian. Then the width of the Lorentzian fit is compared to equation 4.10 with a Gaussian component of width of 503 MHz.

Figure 4.42 shows an example of a Lorentzian fit to a pseudo-Voigt function. It can be seen the Lorentzian fit is a fairly good approximation to a Voigt function. The Lorentzian fit width in this case is 948 MHz, whereas the Voigt width is 1042 MHz.

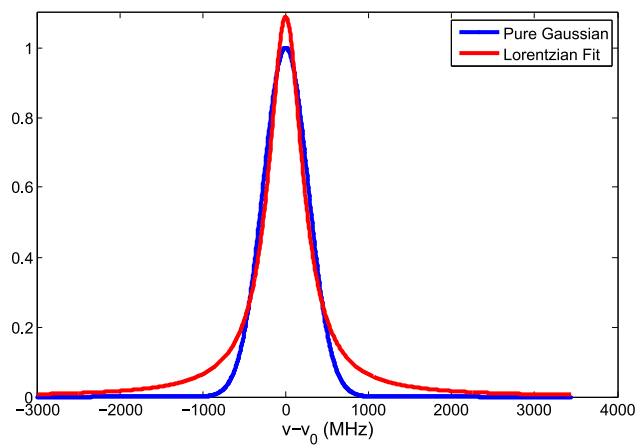


**Figure 4.41:** Lorentzian fit to a pure Gaussian.

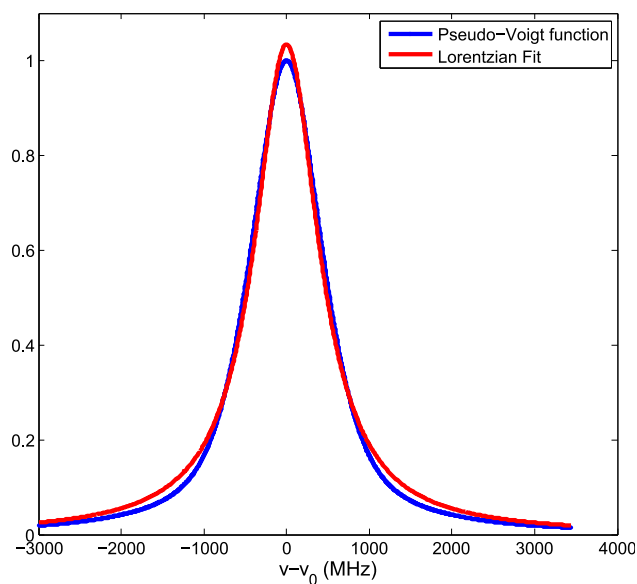


**Figure 4.42:** Lorentzian fit to a pseudo-Voigt function with  $\Delta\nu_G=639$  MHz and  $\Delta\nu_L=700$  MHz.

The width of the Lorentzian fit  $\Delta\nu_{fit}$  to the Voigt function and the width from equation 4.10, with  $\Delta\nu_G=503\text{MHz}$ , both normalized to the actual Voigt width  $\Delta\nu_V$  calculated using  $\Delta\nu_G=639\text{ MHz}$  are plotted in Figure 4.43. The error on the red points comes from the uncertainty in the Lorentzian fit. It is seen that there is a very good agreement between these two ratios, within 2%. This proves that equation 4.10 with Gaussian width of 503 MHz corrects fairly well for the effects of using a Lorentzian fit function rather than a Voigt function.

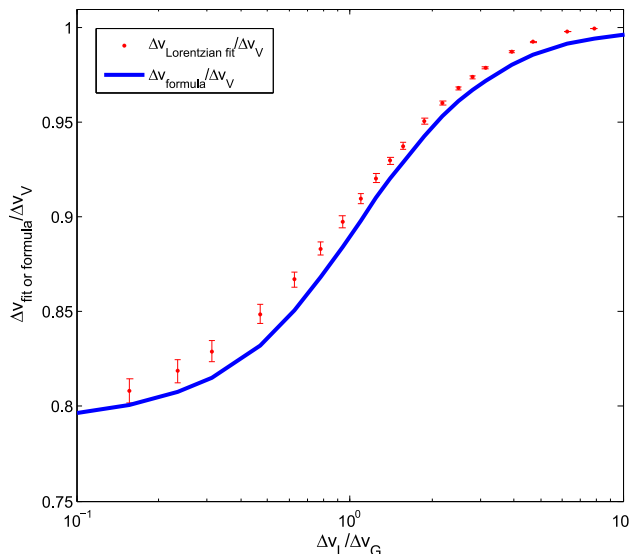


**Figure 4.43:** Measured  $\Delta\nu/p$  versus pressure.

The fit of the excitation spectra versus pressure to equation 4.11 with  $\Delta\nu_G=503\text{MHz}$  is shown in Figure 4.40. It fits the data well and gives a pressure broadening coefficient of  $6.69\pm 0.14\text{ MHz}$ . Another way to calculate the pressure broadening coefficient  $C$  is by calculating  $C$  for each measurement using the quadratic solution to equation 4.11 and then taking a weighted average of the result, as shown in Figure 4.44. The weighted average gives a value of  $6.73\pm 0.81\text{ MHz/Torr}$ . This value is very similar to the value obtained from the fit to equation 4.11. However, the error from the fit in Figure 4.40 assumes purely statistical errors, while the error from the weighted average takes into account actual weighted deviations from the average, which are clearly non-statistical.

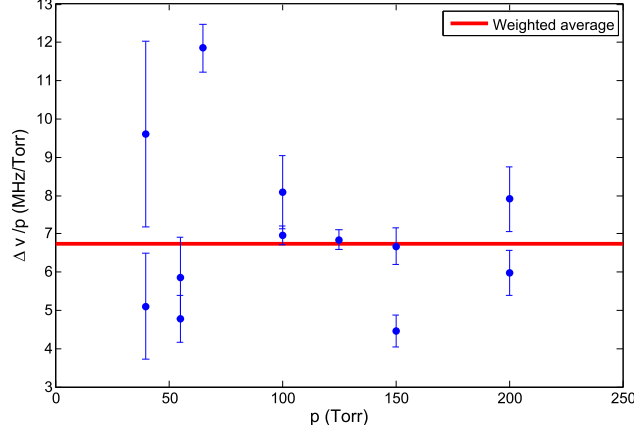


**Figure 4.44:** Measured  $\Delta\nu/p$  versus pressure.

The measured pressure broadening coefficient of  $\text{Ba}^+$  in xenon gas is compared with some pressure broadening coefficients of different atoms and ions with one valence electron in noble gases in Table 4.4. The literature values have been converted from broadening per density

**Table 4.4:** Pressure broadening coefficients in MHz/Torr scaled to 295 K for various atoms and ions in rare gases.

Atom	He	Ne	Ar	Kr	Xe	
Na	7.79(17)	6.27(8)	12.71(9)	11.07(17)	13.40(26)	[45]
Na	8.46(8)	4.38(11)	11.16(9)	12.45(35)	13.66(61)	[46]
K	7.07(14)	3.94(9)	11.56(18)	10.94(27)	13.07(18)	[47]
$\text{Ca}^+$	3.92(21)		5.56(14)			[48]
Rb	9.69(1.81)	4.96(67)	9.58(1.25)	9.58(86)	11.02(1.25)	[49]
Cs	9.62(69)	5.01(39)	9.82(1.08)	9.91(1.18)	10.70(1.28)	[50]
$\text{Ba}^+$	9.68(44)		13.97(67)			[44]
$\text{Ba}^+$					6.73(81)	(this work)

values with an additional scaling of  $T^{0.4}$  for He,  $T^{0.35}$  for Ne and  $T^{0.3}$  for Ar-Xe. This is the first reported measurement of the pressure broadening coefficient of  $\text{Ba}^+$  in Xe gas. It is interesting to compare the measurements of pressure broadening coefficients of ions with measurements of atoms that have the same number of electrons, for example  $\text{Ca}^+$  and K. The pressure broadening coefficient of  $\text{Ca}^+$  is about half the value of the coefficient of Cs in He and in Ar. Another example is  $\text{Ba}^+$  and Cs. The measurements by Zokai et. al. [44] of  $\text{Ba}^+$  in He and Ar have equal or larger pressure broadening coefficients as Cs. The measurement of pressure broadening coefficient of  $\text{Ba}^+$  in Xe presented in this work, compared with the

measurement of Cs in Xe, is in between the other two cases, between half the value and equal to the measurement of Cs in Xe.

A plot of the center frequency of the raw Lorentzian fit versus pressure is shown in Figure 4.45. The error bars on each point are obtained by adding in quadrature the error obtained from the Lorentzian fit and the systematic error of the wavemeter, which is  $\pm 0.01 \text{ cm}^{-1}$ . The pressure shift is the slope of a weighted linear fit to the data. The calculated value of the pressure shift is  $-7 \pm 30 \text{ MHz/Torr}$ . Clearly the scatter of the points is too large to determine the pressure shift.

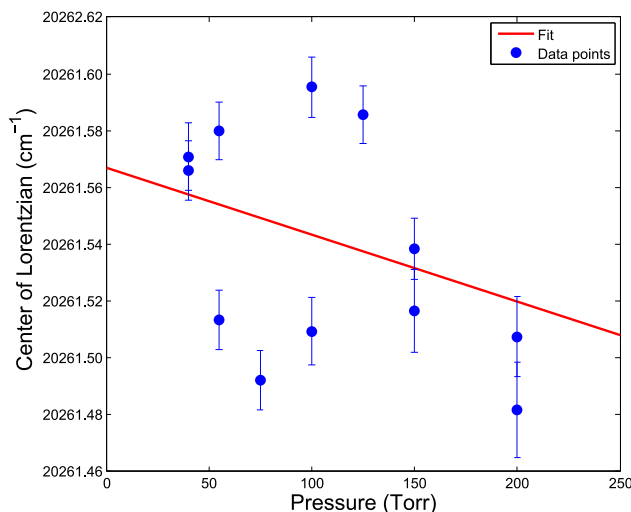


**Figure 4.45:** Pressure shift of the excitation spectra of  $\text{Ba}^+$  in xenon gas.

### 4.3.3 Predicted Fluorescence Counts and Nonradiative Decays

The total excitation rate  $W_{12}$  for an ion at low power can be calculated as

$$W_{12} = \sigma_{12}(\nu) \frac{I}{h\nu} \quad (4.12)$$

where  $\sigma_{12}(\nu)$  is the cross section of the excitation transition,  $I$  is the intensity of the excitation laser, and  $h\nu$  is the photon energy. In the case of  $\text{Ba}^+$  in xenon gas the peak cross section varies with pressure according to

$$\sigma_{12}(\nu_0) \approx \sigma_0 \frac{\Delta\nu_N}{\Delta\nu_p} \quad (4.13)$$

where  $\sigma_0=2.92 \times 10^{-10} \text{ cm}^2$  is the peak cross section for the transition ( $6s \ ^2S_{1/2} - 6p \ ^2P_{1/2}$ ) in vacuum.  $\Delta\nu_N$  is the natural width, 20.1 MHz, and  $\Delta\nu_p$  is the pressure broadening width determined in the previous section. This model is valid at high pressures, but at lower pressures in this experiment, the Doppler broadening complicates the analysis. To approximately account for effects of  $\Delta\nu_D$ , the Lorentzian fit widths in the spectra are used in place of  $\Delta\nu_p$  in equation 4.13.

The excitation laser was focused in the vertical dimension ( $z$ -axis) into an elliptical cross section using a cylindrical lens with  $f=25$  cm. The width of the laser in the horizontal dimension ( $x$ - axis) remains the same throughout the excitation region. The dimensions of the excitation beam were measured by taking beam profiles with a razor blade. A plot of the beam size  $w_z$  as a function of the distance from the cylindrical lens is shown in Figure 4.46. The minimum spot size is  $w_{0z}=0.0015 \pm 0.0001$  cm; it is found by fitting the data to  $w_z(y) = w_{0z} \sqrt{1 + (y/y_0)^2}$ , where  $y_0 = \pi w_{0z}^2 / \lambda$ , and  $\lambda=493.4$  nm. The position of the focus is  $25.88 \pm 0.07$  cm from the lens. The measured beam size in the horizontal direction is  $w_x=0.25$  cm.

The total fluorescence counts/pC/mW at the resonant frequency is obtained from the amplitude of the Lorentzian fit to the uncorrected excitation spectra. The predicted number of emitted photons by one ion is calculated by integrating  $N_2 A_{23rad}$  over the time that the ion interacts with the laser. The population  $N_2(t)$  for a three level system, is given in equation 2.10, and  $A_{23rad}= 3.1 \times 10^7 \text{ s}^{-1}$ .

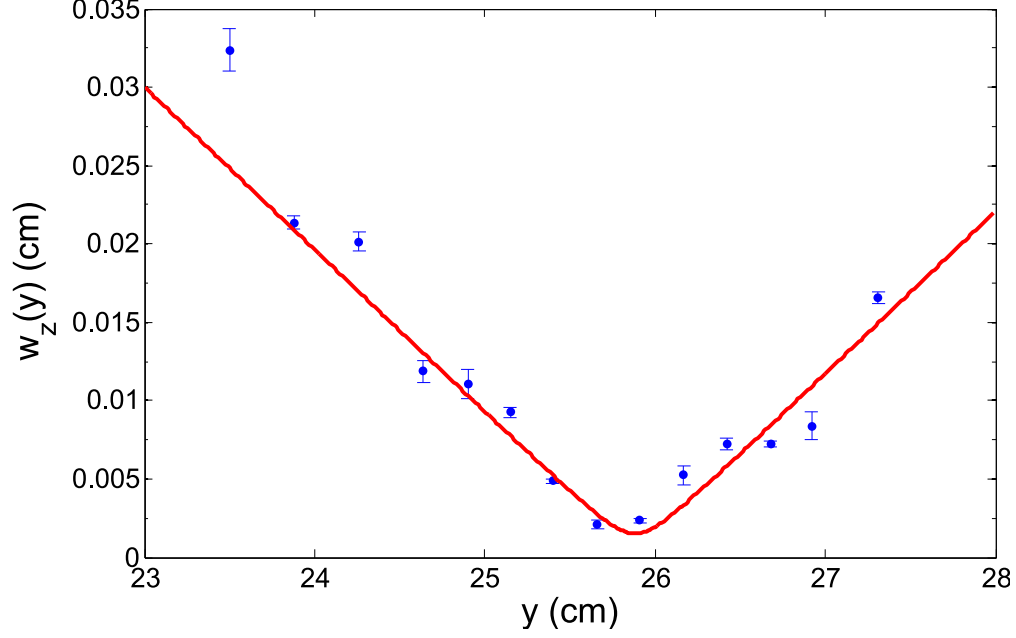


**Figure 4.46:** Laser beam profile in the vertical direction after focusing with a cylindrical lens.

As seen in Chapter 2, the population  $N_2(t)$  depends on the excitation rate  $W_{12}$ , which in turn depends on the intensity. The intensity as a function of  $x$ ,  $y$  and  $z$  is given as

$$I(x, y, z) = I_0 e^{-2x^2/w_x^2} e^{-2z^2/w_z(y)^2} \quad (4.14)$$

where  $x$  is along the direction of the lens,  $y$  is along the laser beam and  $z$  is vertical, along the ion path. The peak intensity is related to the laser power  $P$  by

$$I_0 = \frac{2P}{\pi w_x w_z(y)} \quad (4.15)$$

To simplify calculations with the optical pumping model, the exponential term in equation 4.14 that depends on  $z$  is substituted by a box of constant intensity with width  $2w_z(y)$  and intensity  $hI(x, y, 0)$  where  $h=0.62$ . Then the intensity becomes

$$I(x, y) = I_0 e^{-2x^2/w_x^2} h \quad (4.16)$$

and the  $z$ -dependence of the intensity is eliminated. The interaction time  $\Delta t$  that the ion interact with the laser is

$$\Delta t(y) = \frac{2w_z(y)}{v} = \frac{2w_z(y)}{\mu E} \quad (4.17)$$

$w_z(y)$  is the  $1/e^2$  radius of the laser beam along the ion path at the position  $y$  along the focused beam,  $\mu$  is the measured mobility of the ion from section 4.2, and  $E$  is the electric field in the region where the ion is excited.

The ion cloud is modeled as a uniform sphere of charge of radius  $R$ . The number of ions per area that go through the excitation laser at a position  $(x, y)$  is given by

$$2N\sqrt{R^2 - x^2 - y^2}/(4\pi R^3/3) \quad (4.18)$$

where  $N$  is the total number of ions.

The total number of counts is obtained by calculating the following integral.

$$\# Counts = \int_{-R}^R \int_0^{\Delta t(y)} \int_{-\sqrt{R^2-y^2}}^{\sqrt{R^2-y^2}} NN_2 A_{23rad} \frac{2\sqrt{R^2 - x^2 - y^2}}{\frac{4}{3}\pi R^3} \epsilon(y) f \, dy dt dx \quad (4.19)$$

where  $N_2$  is the population in state 2,  $f$  is the fraction of atomic ions at a given pressure calculated from Section 4.2.3, and  $\epsilon(y)$  is the light detection efficiency as a function of  $y$  reported in Section 3.5.3.

The radius of the ion cloud at the time when it goes through the excitation laser was not specifically measured. It can be estimated by considering the expansion of the ion cloud due to Coulomb repulsion as it travels through xenon gas. The electric field  $E_s$  at the surface of the sphere is

$$E_s = \frac{Q}{4\pi\epsilon_0 R^2} \quad (4.20)$$

The rate of variation of the radius of the ion cloud is

$$\frac{dR}{dt} = \mu E_s = \mu \frac{Q}{4\pi\epsilon_0 R^2} \quad (4.21)$$

After integrating, the radius of the ion cloud at time  $t$  is

$$R = \sqrt[3]{\frac{\mu Q}{4\pi\epsilon_0} t + R_0^3} \quad (4.22)$$

where  $R_0$  is the cloud radius at  $t=0$ . The radius of the ion cloud depends on the mobility of the ions  $\mu$ , the total charge  $Q$ , and the time that the ion cloud travels through xenon gas. The time that the ions travel through xenon gas depends on how fast the ions move, and it can be estimated using the mobility of the ions at each pressure. The total drift time from the tip to the Grid 1 plate is  $t_d = d_{eff}/\mu V_T$ . A straight barium metal tip was used for the fluorescence experiments. The calculated value of  $d_{eff}$  for the position at which the tip was hit during the fluorescence experiments is  $d_{eff}=2.2 \text{ cm}^2$ . Most of the expansion of the ion cloud is going to occur in the region between the barium metal tip and the accelerator, where the ions travel slower since the electric field is weaker in that region. The radius of the ion cloud at the laser region then can be estimated using the time it expands as the total drift time. Table 4.5 shows a summary of drift times and ion cloud radius at different pressures for an initial charge of 2.5 pC. Due to the roughness of this model assigning a 30% systematic uncertainty on  $R$  seems reasonable.

A summary of measured fluorescence counts, expected fluorescence counts, and experimental parameters at different pressures is given in Table 4.6. The expected fluorescence counts/pC/mW is calculated from the integral(equation 4.19) with  $N=(10^{-12}/1.6\times 10^{-19})$ , and then dividing it by the laser power. The measured counts are obtained from the peak of the Lorentzian fit to the uncorrected excitation spectra. The cross sections used to predict the number of fluorescence counts were obtained in section 4.3.2. It is seen that the measured counts are a factor of 3-4 smaller than the predicted counts.

**Table 4.5:** Summary of drift times and estimated radius of ion cloud for different xenon pressures.

Pressure (Torr)	40	55	100	150	200
$d_{eff}^2$ (cm <sup>2</sup> )	2.2	2.2	2.2	2.2	2.2
Voltage target $V_T$ (V)	400	446	669	780	891
$\mu$ (cm <sup>2</sup> /Vs)	14.4	10.3	5.5	3.5	2.6
Charge (pC)	2.5	2.5	2.5	2.5	2.5
$t_d$ (ms)	0.38	0.48	0.60	0.81	0.95
$R$ (cm)	<b>0.33(10)</b>	<b>0.32(10)</b>	<b>0.28(9)</b>	<b>0.27(8)</b>	<b>0.26(8)</b>

Nonradiative decay rates  $A_{23nonrad}$  from state 2 to state 3 affect the total number of fluorescence counts detected. The larger  $A_{23nonrad}$  is, the smaller the number of fluorescence counts at 650 nm are. Figure 4.47 shows the predicted fluorescence counts with  $A_{31}=0$  and different rate constants for  $A_{23nonrad}$ . For rate constants up to  $10^4$  s<sup>-1</sup>/Torr, there is not much effect on the predicted counts. For higher rate constants, it can be seen that the fluorescence counts decrease as the rate constant for  $A_{23nonrad}$  increases. For rates constants greater than  $10^6$  s<sup>-1</sup>/Torr the predicted number of counts becomes smaller than the measured number of counts.

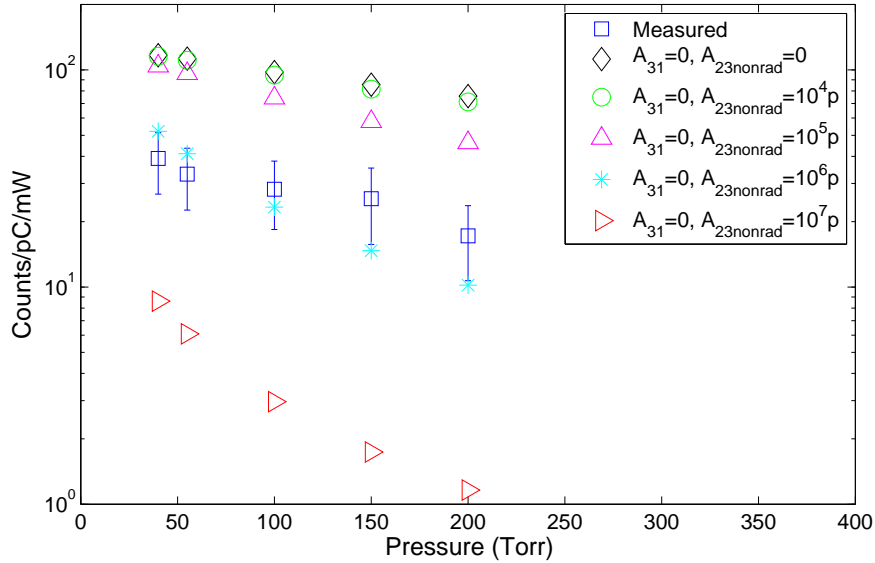


**Figure 4.47:** Predicted number of counts with  $A_{31}=0$  and varying  $A_{23nonrad}$ .

**Table 4.6:** Summary of measured and predicted 650 nm fluorescence counts/pC/mW at the resonant frequency, without nonradiative decays.

<b>Pressure (Torr)</b>	<b>40</b>	<b>55</b>	<b>100</b>	<b>150</b>	<b>200</b>
$\mu_0$ (cm <sup>2</sup> /Vs)	0.71	0.70	0.67	0.65	0.63
Electric field V/cm	307.5	342.5	515	600	685
Ion cloud radius (cm)	0.33	0.32	0.28	0.27	0.26
Photon energy $h\nu$ (mJ)	4.03E-16	4.03E-16	4.03E-16	4.03E-16	4.03E-16
$\Delta\nu_p$ (MHz)	822	899	1152	1465	1801
$\sigma$ (cm <sup>2</sup> )	7.96E-12	7.56E-12	6.54E-12	5.65E-12	4.94E-12
$W_{12}$ (s <sup>-1</sup> ) at laser focus	4.16E7	3.95E7	3.42E7	2.95E7	2.58E7
Max Detection efficiency $\epsilon_0$	0.96E-04	0.96E-04	0.96E-04	0.96E-04	0.96E-04
Percentage of Ba <sup>+</sup>	0.81	0.76	0.64	0.54	0.47
<b><u>Predicted counts</u></b> <b>pC · mW</b>	116.9	112.6	97.7	85.5	75.7
<b><u>Measured counts</u></b> <b>pC · mW</b>	39.1(12.3)	33.1(10.5)	28.2(9.8)	25.5(9.8)	17.3(6.5)

Nonradiative decays out of the metastable state at rate  $A_{31}$  can also affect the number of fluorescence counts detected. Figure 4.48 shows a plot of predicted number of counts with  $A_{23nonrad}=0$ , and different rate constants for  $A_{31}$ . By increasing the rate constant  $A_{31}/p$ , more ions will decay from the 3 state to the ground state. This causes the fluorescence counts to increase because more ions are available to excite in the ground state. As can be seen in Figure 4.48, the effect is more pronounced at higher pressures.

Figure 4.49 shows different combinations of rate constants for  $A_{23nonrad}$  and  $A_{31}$  that give predicted values within the uncertainties of the measured counts. The uncertainty of the measured counts is calculated by adding the statistical error from the peak of the Lorentzian fit, and the systematic error due to detection efficiency. This systematic error is estimated from the the difference between the measured detected efficiency and the estimated detection efficiency calculated in Chapter 3.

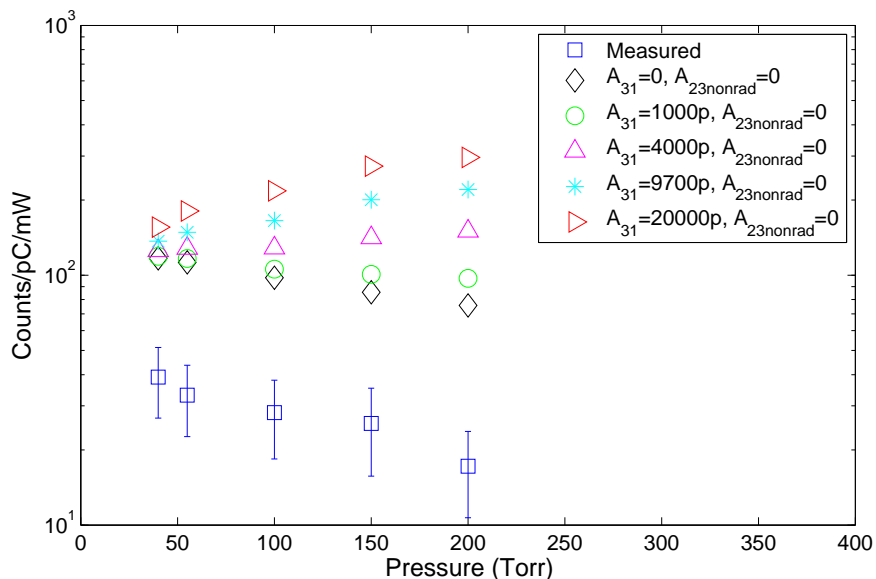


**Figure 4.48:** Predicted number of counts with  $A_{23nonrad}=0$  and varying  $A_{31}$ .

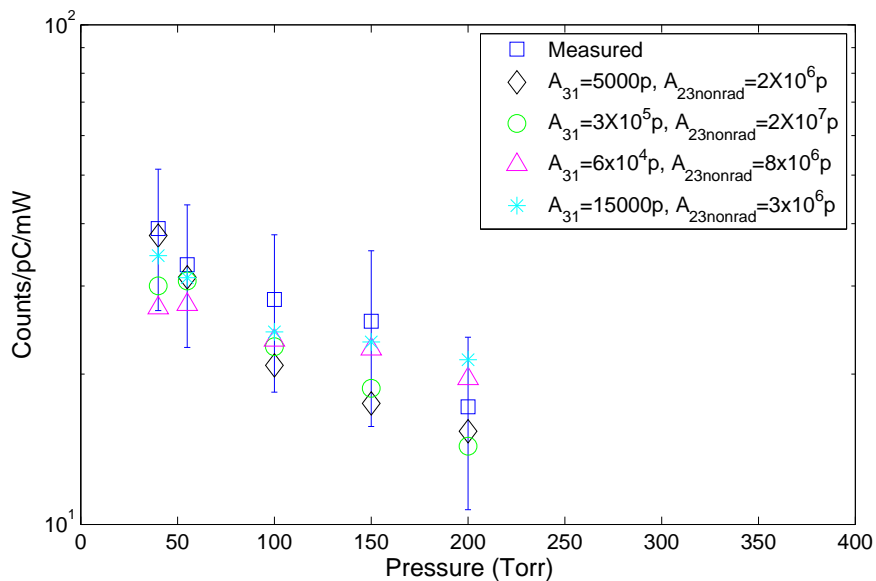


**Figure 4.49:** Different combinations of rate constants for  $A_{23nonrad}$  for  $A_{31}$  that give predicted values within the uncertainty of the measured counts.

A summary of combination of rate constants for  $A_{23nonrad}$  and  $A_{31}$  that give predicted number of counts within the uncertainty limits are shown in Figure 4.50 . The red dots represent the combinations of values of  $A_{23nonrad}$  for  $A_{31}$  with predicted number of counts within the uncertainty limits, while the crosses represent predictions that are outside the uncertainty limits. The plot shows a that  $A_{23nonrad}$  is between  $2 \times 10^6$  and  $3 \times 10^7$   $s^{-1}/\text{Torr}$ , and  $A_{31}$  is between 4000 and  $3 \times 10^6$   $s^{-1}/\text{Torr}$ . For comparison the measured rate constant for collisional de-excitation of  $D$  states of  $\text{Ba}^+$  in helium is  $9.7 \times 10^3$   $s^{-1}/\text{Torr}$  [26].

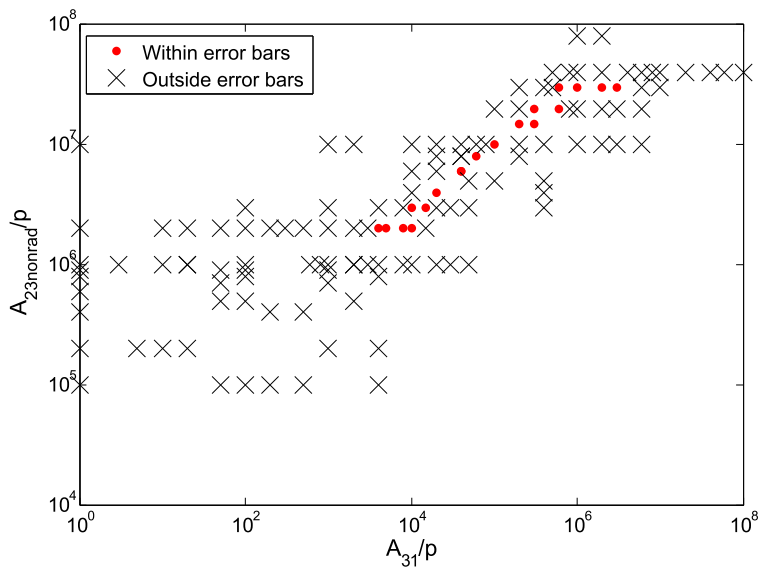


**Figure 4.50:** Plot of region allowed in  $A_{nonrad}$  space.

The uncertainty in the radius of the ion cloud adds additional uncertainty in the predicted number of counts. Figure 4.51 shows the predicted number of counts using the ion cloud radius and its upper and lower limits given in Table 4.5, with  $A_{23nonrad}=0$  and  $A_{31}=0$ . It is seen that for the lower limit of radius the predicted counts increase. This is expected since more ions will go through the laser and through the region where the detection efficiency is higher. For the upper limit of the radius the effect is the opposite. Thus less correction by nonradiative rates is needed for the ion radius and the upper limit, and more corrections is needed at the lower limit.

Plots of the allowed region for the rate constants  $A_{23nonrad}$  and  $A_{31}$  for the lower and upper limit of the ion cloud radius are shown in Figure 4.52 and Figure 4.53, respectively.

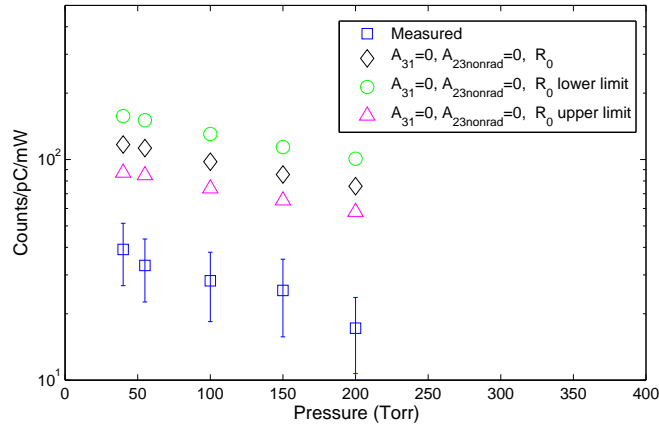


**Figure 4.51:** Comparison of predicted number of counts for the upper and lower limit of the radius of the ion cloud.

The allowed region for the lower limit is about the same as the region in Figure 4.50. It shifts to slightly higher  $A_{23nonrad}$  values and slightly lower  $A_{31}$  values, as expected. For the upper limit on ion radius, the range of allowed values of  $A_{31}$  and  $A_{23nonrad}$  increases. The allowed values in this case are  $6 \times 10^5$  to  $2 \times 10^7$   $\text{s}^{-1}/\text{Torr}$  for  $A_{23nonrad}$ , and 0 to  $1 \times 10^7$   $\text{s}^{-1}/\text{Torr}$  for  $A_{31}$ .

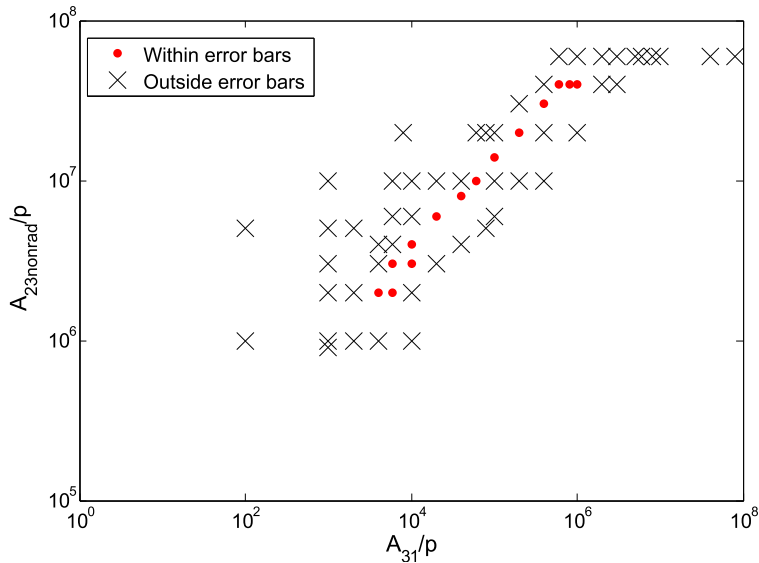


**Figure 4.52:** Plot of region allowed in  $A_{nonrad}$  space with 30% smaller ion cloud radius.

The range of allowed values are plotted in the  $A_{nonrad}$  space, and fit to a function of the form  $y = m\sqrt{x}$ . The allowed values and the fits are shown in Figure 4.54. From the fits,

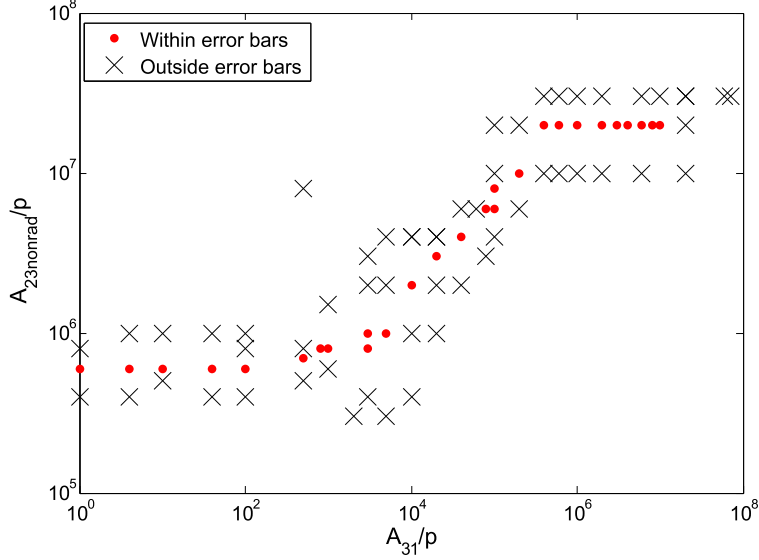


**Figure 4.53:** Plot of region allowed in  $A_{nonrad}$  space with 30% larger ion cloud radius.

a ratio  $A_{23nonrad}/p/\sqrt{A_{31}/p}$  is obtained for each ion cloud radius. For the central value of the ion cloud radius  $A_{23nonrad}/p/\sqrt{A_{31}/p}=3.14(12)\times 10^4 \text{ MHz}^{1/2}/\text{Torr}^{1/2}$ . For the lower and upper limit of the ion cloud radius, the ratios obtained are  $4.49(12)\times 10^4$  and  $2.36(7)\times 10^4 \text{ MHz}^{1/2}/\text{Torr}^{1/2}$ , respectively.

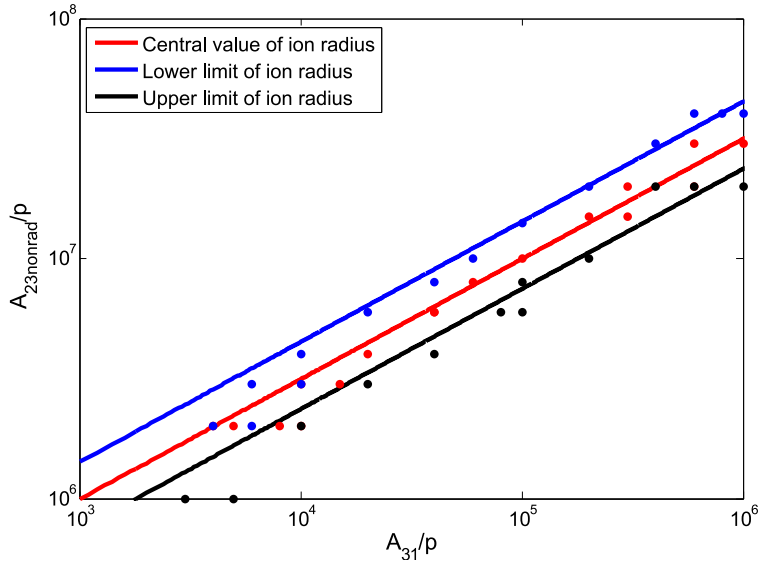


**Figure 4.54:** Plot of allowed values of  $A_{nonrad}$ .

In conclusion, a decrease in the fluorescence with increasing pressure was observed. It is due to the combination of three effects: a decrease in the cross section due to pressure

broadening, a decrease on the number of atomic ions, and an increase in non radiative decays. The predicted number of counts agree with the measured counts for various combinations of  $A_{23nonrad}$  and  $A_{31}$ , and a range of possible values was given. Radiative decays in the fluorescence of  $Ba^+$  in xenon gas are comparable to the nonradiative decays at the range of pressures measured. The plots of the allowed values of  $A_{23nonrad}$  suggest that the nonradiative decay rate constant for  $A_{23nonrad}$  is between  $6 \times 10^5$  and  $4 \times 10^7$   $s^{-1}/Torr$ .

#### 4.3.4 Single Ion Detection at High Pressure Xenon Gas

A single  $Ba^+$  ion in high pressure xenon gas, e.g. in an EXO gas TPC, could be detected using the photon burst detector technique used for counting  $Mg^+$  atoms [51]. The number of photons emitted is  $N_2 A_{23rad} \Delta t f_{Ba^+}$ , where  $N_2$  is the probability that the ion is state 2,  $A_{23rad}$  the radiative decay rate from state 2 to state 3,  $\Delta t$  is the time that the ion interacts with the laser, and  $f_{Ba^+}$  the fraction of time that the ion is in atomic state. To overcome optical pumping a repump laser might be used to pump out atoms out of the metastable state 3 ( $^2D_{3/2}$ ).

In steady state  $N_2$  is given by solution of the rate equations for a three level system

$$N_2 = \frac{W_{12}(A_{31} + W_{32})}{(A_{21} + A_{23} + W_{12})(A_{31} + W_{32}) - A_{23}W_{32} + W_{12}A_{23}} \quad (4.23)$$

where  $W_{12}$  and  $W_{32}$  are the excitation rates from state 1 to 2, and from state 3 to 2, respectively and  $A_{ij}$  are the decay rates from state  $i$  to state  $j$ .

Figure 4.55 shows a a simple diagram of a possible detection scheme of  $Ba^+$  in high pressure xenon gas. A laser going parallel to the plane of the photomultiplier (or APD) front face, and passing along the line focus of an elliptical cylinder, excites a barium ion moving along the laser at a speed  $v$ . The fluorescence emitted by the ion is detected by the photomultiplier (PMT).

A list of parameters needed for the calculation of the number of counts detected by a photon burst detector is shown in Table 4.7. The expected number of fluorescence counts

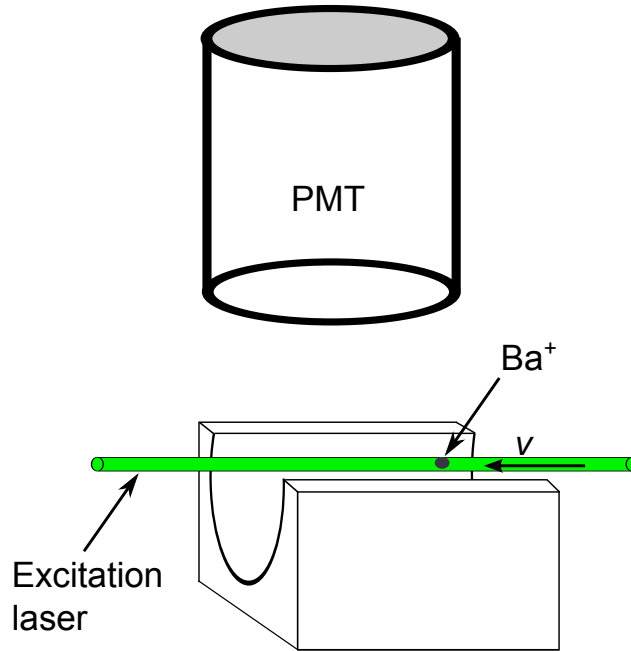


**Figure 4.55:** Schematic diagram of a photon burst detector used to detect  $\text{Ba}^+$  in high pressure xenon gas.

using a 2" diameter end window photomultiplier, with a quantum efficiency of 0.15 and a collection efficiency of 0.6, and using a pumping laser is given in Table 4.8 for sample constants spanning the allowed range and  $P=10$  mW for both lasers. The ion is assumed to drift in a constant electric field of 100 V/cm. Predicted photons emitted and the burst detected at different pressures are shown for two cases: when a repumping laser is used, and when no repumping laser is used. Since the exact value of the rate constants is not known, calculations for different allowable values of  $A_{23nonrad}$  and  $A_{31}$  are shown. Table 4.9 shows the predicted photons emitted when no pumping laser is used.

Figure 4.56 shows a plot of excitation laser power versus photon counts with  $A_{23nonrad}=10^7p$  and  $A_{31}=10^5p$ . For these intermediate decay rate constants, increasing the repumping laser power does not increase the number of counts significantly. Increasing the excitation laser power has a larger effect in increasing the number of counts. Figure 4.57 shows a plot of excitation laser power versus photon counts for the lowest allowed constants,  $A_{23nonrad}=6 \times 10^5p$  and  $A_{31}=0$ . In this case increasing the excitation laser power does not significantly increase the number of counts, but increasing the repump laser power has a larger effect in this case.

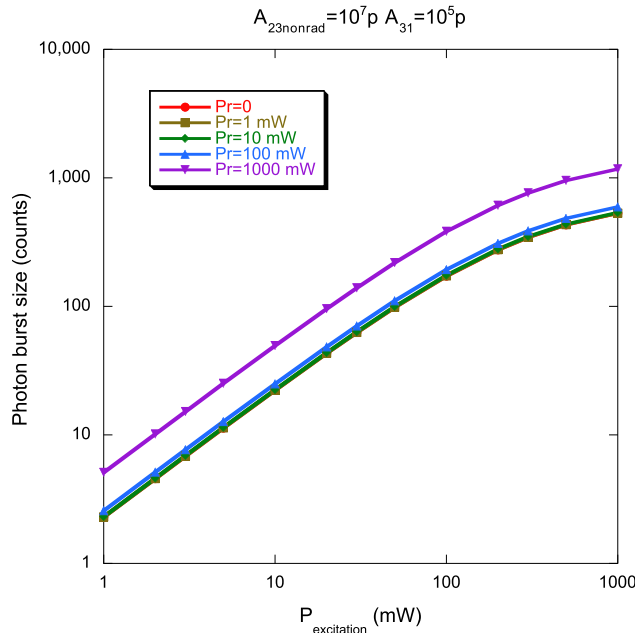


**Figure 4.56:** Burst counts versus laser power using different pumping laser power with  $A_{23nonrad}=10^7 p$  and  $A_{31}=10^5 p$  at 5 atm pressure.

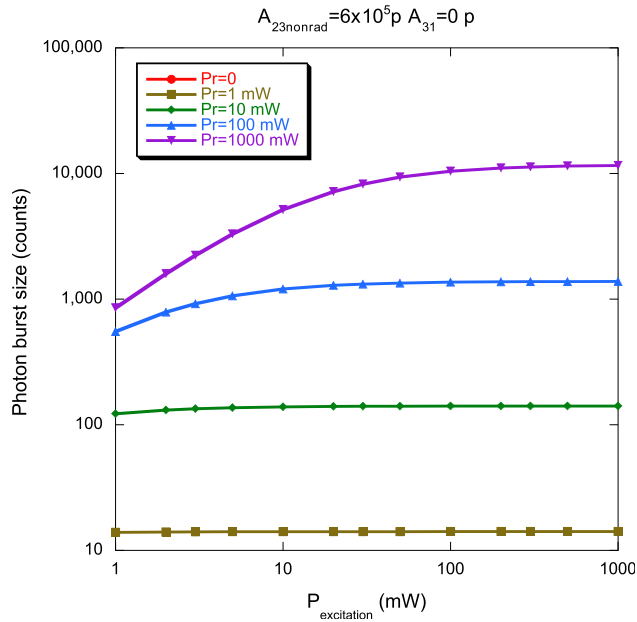


**Figure 4.57:** Burst counts versus laser power using different pumping laser power with  $A_{23nonrad}=6 \times 10^5 p$  and  $A_{31}=0$  at 5 atm pressure.

**Table 4.7:** Summary of parameters used in the calculation of the counts of a photon burst detector.

Pressure (Torr)	40	100	200	760	3800	7600
$\sigma_{12}$ (cm <sup>2</sup> )	7.96E-12	6.54E-12	4.94E-12	1.14E-12	2.29E-13	1.15E-13
$\sigma_{32}$ (cm <sup>2</sup> )	2.25E-12	1.85E-12	1.40E-12	3.21E-13	6.49E-14	3.24E-14
$\mu$ (cm <sup>2</sup> /Vs)	14.71	5.59	2.64	0.62	0.12	0.06
$\Delta t$ (s)	3.40E-3	8.94E-3	1.89E-2	8.06E-2	4.34E-1	8.78E-1
Percentage of Ba <sup>+</sup>	0.85	0.70	0.54	0.23	0.06	0.03

**Table 4.8:** Predicted number of photons and burst detected from fluorescence of Ba<sup>+</sup> in Xe gas using a pumping laser with 10 mW of power for both the excitation and pumping laser and radius  $w= 1$  mm.

Pressure (Torr)	40	100	200	760	3800	7600
$A_{23nonrad}=10^7$ p, $A_{31}=10^5$ p Burst detected	109	129	128	78	23	11
$A_{23nonrad}=2 \times 10^6$ p, $A_{31}=10^4$ p Burst detected	260	333	340	249	96	54
$A_{23nonrad}=3 \times 10^7$ p, $A_{31}=10^6$ p Burst detected	65	65	56	28	8	4
$A_{23nonrad}=6 \times 10^5$ p, $A_{31}=0$ Burst detected	398	623	695	468	139	73

The calculations show that it may be possible to get large photon burst from a single Ba<sup>+</sup> ion in xenon gas at pressures between 1 and 10 atm. Even with no pumping laser it may be possible to detect Ba<sup>+</sup> if the decay rate constant  $A_{31}/p$  is on the order of  $10^4$  s<sup>-1</sup>/Torr or higher. If  $A_{31}$  is close to zero, then a repump laser will be needed.

**Table 4.9:** Predicted number of photons and burst detected from fluorescence of Ba<sup>+</sup> in Xe gas with no pumping laser. Using 10 mW of power for the excitation laser

<b>Pressure (Torr)</b>	<b>40</b>	<b>100</b>	<b>200</b>	<b>760</b>	<b>3800</b>	<b>7600</b>
$A_{23nonrad}=10^7$ p, $A_{31}=10^5$ p Burst detected	53	87	98	66	19	10
$A_{23nonrad}=2 \times 10^6$ p, $A_{31}=10^4$ p Burst detected	27	65	103	140	74	44
$A_{23nonrad}=3 \times 10^7$ p, $A_{31}=10^6$ p Burst detected	58	60	52	26	7	3
$A_{23nonrad}=6 \times 10^5$ p, $A_{31}=0$ Burst detected	0	0	0	0	0	0

## 5 Conclusion

The mobility of barium ions in xenon gas and the pressure broadening of  $\text{Ba}^+$  in xenon gas at pressures between 40 to 200 Torr mobility was measured for the first time. A liquid xenon purity monitoring scheme was also implemented using the existing electrodes in our liquid xenon test apparatus, and purity measurements were made for various experimental conditions. These results have importance for ongoing work on barium tagging for the EXO collaboration. Some of these impacts are discussed in the following paragraphs.

Through electron lifetime measurements in liquid xenon, it was determined that after passing Xe gas through a commercial purifier, the electron lifetime in liquid xenon was greater than  $300 \mu\text{s}$ . This corresponds to impurity concentrations of less than 1 ppb. An important finding was that the ablation of a barium metal tip does not noticeably affect the purity of liquid xenon at this level. This is significant for future experiments in our research group. The liquid xenon system is currently being adapted for extraction of  $\text{Ba}^+$  ions by capture in frozen xenon on the end of a cryotip. The plan is to detect the ions on the frozen tip using the spectroscopy methods for detection of barium atoms and ions in solid xenon developed by Brian Mong and Shon Cook [19, 21]. For initial tests, barium ions will be implanted in liquid xenon by laser ablation. Having pure xenon is of considerable importance for the detection of barium in solid xenon. Previous work reported in Shon Cook's thesis [52] suggests that impurities in solid xenon at the percent level may reduce the fluorescence efficiency. Having concentration of impurities of less than 2 ppb in liquid xenon should remove any impurity effect on the fluorescence efficiency.

The mobility measurements of barium ions in xenon gas are significant for the EXO collaboration because one possibility for the next generation  $0\nu\beta\beta$  decay experiment is to use a xenon gas detector. The measured mobility is close to theoretical calculations. It was also concluded from mobility measurements as a function of xenon gas pressure that  $\text{Ba}^+$  reacts with xenon atoms to form  $\text{BaXe}^+$ , and molecular ions become dominant at high

pressures. The results indicate that at 1 atmosphere only 1/5 of ions will be  $\text{Ba}^+$  at a given time. The proposed EXO gas detector is expected to run at pressures around 5 to 10 atmospheres. At such high pressures only a few percent of ions are expected to be  $\text{Ba}^+$  at a time. Alternatively, if the ion is to be extracted from the high pressure chamber to a low pressure chamber and then to a vacuum chamber for detection, the relevant mobility at high pressure will be mainly that measured for  $\text{BaXe}^+$ . The ion is planned to be extracted through the nozzle using an RF carpet. It is desired that the ion comes out as atomic since it is planned to capture and detect it as  $\text{Ba}^+$  in a trap. In equilibrium the ion is  $\text{Ba}^+$  at low pressure. However, if the ion is initially in the molecular state and it travels faster through the nozzle than the dissociation rate, the ion will be extracted in the molecular state. If the ion moves more slowly, then the final state is expected to be  $\text{Ba}^+$ . Integration of velocity and gas density in nozzle simulations and using the results of this thesis indicate that  $\text{Ba}^+$  is the likely extracted ion. This is good news for this proposed barium tagging scheme.

The pressure broadening of the excitation spectra of  $\text{Ba}^+$  in xenon gas was reported in this thesis. The measured pressured broadening coefficient is  $6.73 \pm 0.81$  MHz/Torr. A model that takes into account the collection efficiency, the time that the ions interact with the laser, the percentage of atomic ions in xenon gas, which were calculated using the mobility results, and optical pumping was developed to predict the number of fluorescence counts. The main conclusion from the model is that nonradiative decays from the  $^2\text{P}_{1/2}$  state 2 to the  $^2\text{D}_{3/2}$  and from the  $^2\text{D}_{3/2}$  state to the  $^2\text{S}_{1/2}$  state in the range of pressures between 40 and 200 Torr may be comparable to or larger than the radiative decays. From the data and the optical pumping model, a range of possible values for the rate constants  $A_{23\text{nonrad}}/p$  and  $A_{31}/p$  were determined. It may be possible to detect  $\text{Ba}^+$  directly in a high pressure xenon gas TPC. The main factors that decrease the fluorescence counts are the percentage of the time the barium ion will be in atomic state, only a few percent at TPC pressures, and nonradiative decays. From the model used to predict the number of fluorescence counts it was observed that to some degree the fluorescence gain from  $D \rightarrow S$  nonradiative decays at high pressures

compensates for fluorescence loss due to  $P \rightarrow D$  non radiative decays. A predicted burst of hundreds to thousands of counts of fluorescence from a single Ba<sup>+</sup> ion in high pressure xenon gas in a photon burst detector suggests that it may be feasible to detect single <sup>136</sup>Ba<sup>+</sup> daughters of <sup>136</sup>Xe double beta decay in 5 atm xenon gas by this method.

# References

- [1] S. M. Bilenky. Neutrino. History of a unique particle. *The European Physical Journal H*, 38(3). 1, 6
- [2] B. Pontecorvo. Mesonium and antimesonium. *J. Exptl. Theort. Phys.*, 34(247), 1958. 2
- [3] R. Davis Jr, D. Harmer, and K. Hoffman. Search for neutrinos from the sun. *Physical Review Letters*, 20(21), 1968. 2
- [4] K. Zuber. *Neutrino Physics*. Institute of Physics Publishing, 2004. 2, 4
- [5] J. M. Levy. On the derivation of the neutrino oscillation length formula. *arXiv:hep-ph/0004221*, 2000. 3
- [6] S. M. Bilenky and Carlo Giunti. Neutrinoless double-beta decay:A brief review. *Mod. Phys. Lett.*, A27(1230015), 2012. 4, 8, 13
- [7] F.P. An et. al. Spectral measurement of electron antineutrino oscillation amplitude and frequency at Daya Bay. *arXiv:1310.6732*, 2013. 4
- [8] C. P. Burgess and G. D. Moore. *The Standard Model: A Primer*. Institute of Physics Publishing, 2004. 6
- [9] S. R. Elliot and P. Vogel. Double Beta Decay. *Ann. Rev. Nucl. Part. Sci.*, 52(115), 2002. 7
- [10] H.V. Klapdor-Kleingrothaus et. al. Latest results from the HEIDELBERG-MOSCOW double beta decay experiment. *The European Physical Journal A*, 12, 2001. 8
- [11] M. Agostini et. al. Results on neutrinoless double- $\beta$  decay of  $^{76}\text{Ge}$  from phase I of the GERDA experiment. *Physical Review Letters*, 111(122503), 2013. 8

- [12] A. Gando et. al. Limit on neutrinoless  $\beta\beta$  decay of  $^{136}\text{Xe}$  from the first phase of the KamLAND-Zen an comparison with the positive claim in  $^{76}\text{Ge}$ . *Physical Review Letters*, 110(062502), 2013. 9
- [13] M. et. al. M. Auger. Search for neutrinoless double-beta decay in  $^{136}\text{Xe}$  with EXO-200. *Phys. Rev. Lett.*, 109:032505, Jul 2012. 9
- [14] M. K. Moe. Detection of neutrinoless double-beta decay. *Phys. Rev. C*, 44(3), 1991. 9, 12
- [15] N. Ackerman et. al. Observation of Two-Neutrino Double-Beta Decay in  $^{136}\text{Xe}$  with the EXO-200 Detector. *Physical Review Letters*, 107, 2011. 9, 11
- [16] M. Auger et. al. The EXO-200 detector, part I: detector design and construction. *Journal of Instrumentation*, 7(05), 2012. 11, 12
- [17] A. Gando et. al. Measurement of the double- $\beta$  decay half-life of  $^{136}\text{Xe}$  with the KamLAND-Zen experiment. *Phys. Rev. C*, 85:045504, 2012. 11
- [18] M. Danilov, R. DeVoe, A. Dolgolenko, G. Giannini, G. Gratta, P. Picchi, A. Piepke, and F. Detection of very small neutrino masses in double-beta decay using laser tagging. *Physics Letters B*, 480(12), 2000. 12, 13
- [19] B. Mong. *Barium tagging in solid xenon for the EXO experiment*. PhD thesis, Colorado State University, 2011. 13, 143
- [20] Kendy Hall. *In-situ laser tagging of barium ions in liquid xenon for the EXO experiment*. PhD thesis, Colorado State University, 2012. 13, 31, 43, 61, 74
- [21] S. Cook. *Detection of small numbers of barium ions implanted in solid xenon for the EXO experiment*. PhD thesis, Colorado State University, 2012. 13, 143
- [22] E. Rollin. *Barium Ion Extraction and Identification from Laser Induced Fluorescence in Gas for the Enriched Xenon Observatory*. PhD thesis, Carleton University, 2011. 13

- [23] J. Curry. Compilation of wavelengths, energy levels, and transition probabilities for Ba I and Ba II. *Journal of Physical and Chemical Reference Data*, 33(3):725–746, 2004. 15
- [24] W. Nagourney, J. Sandberg, and H. Dehmelt. Shelved optical electron amplifier: Observation of quantum jumps. *Physical Review Letters*, 56(26):2797–2799, 1986. 16
- [25] N. Yu, W. Nagourney, and H. Dehmelt. Radiative lifetime measurement of the Ba<sup>+</sup> metastable D<sub>3/2</sub> state. *Physical Review Letters*, 78(26):4898–4901, 1997. 16
- [26] M. Hermanni and G. Werth. Collisional de-excitation of the metastable *d*-states of Ba<sup>+</sup> by He, Ne, N<sub>2</sub>, and N<sub>2</sub>. *Zeitschrift fr Physik D Atoms, Molecules and Clusters*, 11(4), 1989. 17, 135
- [27] J. T. Verdeyen. *Laser Electronics*. Prentice Hall, 3rd edition, 1995. 20, 22, 23
- [28] O. Svelto. *Principles of Lasers*. Plenum Press, 1998. 21
- [29] E. Aprile, R. Mukherjee, and M. Suzuki. Measurements of the lifetime of conduction electrons in liquid xenon. *Nuclear Instruments and Methods in Physics Research A*, 300:343–350, 1991. 24
- [30] G. Bakale, U. Sowada, and W. Schmidt. Effect of an electric field on electron attachment to SF<sub>6</sub>, N<sub>2</sub>O, and O<sub>2</sub> in liquid argon and xenon. *Journal of Physical Chemistry*, 80(23):2556–2559, 1976. 24, 88
- [31] A. Bettini et al. A study of the factors affecting the electron lifetime in ultra-pure liquid argon. *Nuclear Instruments and Methods in Physics Research A*, 305:177–186, 1991. 25, 51
- [32] E. A. Mason and E. W. McDaniel. *Transport properties of ions in gases*. Wiley, 1988. 26
- [33] M. F. McGuirk et al. Theoretical study of Ba<sup>n+</sup>-RG complexes and transport of Ba<sup>n+</sup> through RG. *The Journal of Chemical Physics*, 130(194305), 2009. 26, 28, 95, 104, 109

- [34] S. C. Jeng, W. M. Fairbank Jr, and M. Miyajima. Measurements of the mobility of alkaline earth ions in liquid xenon. *Journal of Physics D: Applied Physics*, 42(3):035302, 2009. 26, 31, 95
- [35] P. N. B. Neves, C.A.N. Conde, and L.M.N. Tavora. The  $X^+ + 2X \rightarrow X_2^+ + X$  reaction rate constant for Ar, Kr and Xe, at 300 K. *Nuclear Instruments and Methods in Physics Research A*, 619:75–77, 2010. 27, 28
- [36] S. Petrie and R. C. Dunbar. Main group metal ion chemistry in planetary atmospheres. In R. I. Kaiser et al., editor, *Astrochemistry, From Laboratory Studies to Astronomical Observations*. American Institute of Physics, 2006. 28
- [37] S. C. Jeng. *New Fluorescence technique to search for neutrino masses by identification of  $0\nu\beta\beta$  decay  $^{136}\text{Ba}^+$  ion daughters in liquid xenon*. PhD thesis, Colorado State University, 2004. 31, 69
- [38] C. C. Lim. Far-infrared high density polyethylene windows for low-temperature and moderate pressure applications. *Review of Scientific Instruments*, 57(1419):1419–1421, 1986. 33
- [39] E. Buckley et al. A study of ionization electrons drifting over large distances in liquid argon. *Nuclear Instruments and Methods in Physics Research A*, 275:364–372, 1989. 51, 63
- [40] W. Shockley. Currents to conductors induced by a moving point charge. *Journal of Applied Physics*, 9(635), 1938. 53
- [41] S. M. Penn, J. P. M. Beijers, and R. A. Dressler. Laser-induced fluorescence measurements of drift-velocity distributions for  $\text{Ba}^+$  in Ar: Moment analysis and a direct measure of skewness. *The Journal of Chemical Physics*, 93(5118), 1990. 95, 104, 109
- [42] J.J. Olivero and R.L. Longbothum. Empirical fits to the voigt line width: A brief review. *Journal of Quantitative Spectroscopy and Radiative Transfer*, 17(2), 1977. 122

- [43] S. Thompson, D. E. Cox, and J. B. Hastings. Rietveld refinement of Debye-Scherrer synchrotron X-ray data from  $\text{Al}_2\text{O}_3$ . *J. Appl. Cryst.*, 20:79–83, 1987. 123
- [44] M. Zokai, M. Harris, I. Shannon, D. Szebesta, D. McHugh, and E. L. Lewis. Pressure broadening of the  $\text{Ba}^+$  resonance doublet by helium and argon. *Journal of Physics B: Atomic and Molecular Physics*, 20(17), 1987. 126
- [45] R. H. Chatham, A. Gallagher, and E. L. Lewis. Broadening of the sodium D lines by rare gases. *Journal of Physics B: Atomic and Molecular Physics*, 13(1), 1980. 126
- [46] N. Allard and J. Kielkopf. The effect of neutral nonresonant collisions on atomic spectral lines. *Rev. Mod. Phys.*, 54, 1982. 126
- [47] N. Lwin and D. G. McCartan. Collision broadening of the potassium resonance lines by noble gases. *Journal of Physics B: Atomic and Molecular Physics*, 11(22), 1978. 126
- [48] N. J. Bowman and E. L. Lewis. Collision broadening and shifts in the spectra of neutral and singly ionised calcium. *Journal of Physics B: Atomic and Molecular Physics*, 11(10), 1978. 126
- [49] Ch. Ottinger, R. Scheps, G. W. York, and A. Gallagher. Broadening of the Rb resonance lines by the noble gases. *Phys. Rev. A*, 11, 1975. 126
- [50] E. Bernabeu and J. M. Alvarez. Shift and broadening of hyperfine components of the first doublet of cesium perturbed by foreign gases. *Phys. Rev. A*, 22, 1980. 126
- [51] R. D. LaBelle, C. S. Hansen, M. M. Mankowski, and W. M. Fairbank. Isotopically selective atom counting using photon burst detection. *Physical Review A*, 54(5), 1996. 138
- [52] S. Cook. *Detection of small number of barium ions implanted in solid xenon for the EXO experiment*. PhD thesis, Colorado State University, 2012. 143